
THE UNIVERSITY *of* EDINBURGH

# The kaon semileptonic form factor with near physical domain wall quarks


*Karthee Sivalingam*

A thesis submitted in fulfillment of the requirements
for the degree of Doctor of Philosophy
to the
University of Edinburgh
2013

# Abstract

The CKM matrix element $|V_{us}|$ can be extracted from the experimental measurement of semileptonic $K \to \pi$ decays and theoretical input for the corresponding vector form factor in QCD. The thesis performs a major improvement of the RBC/UKQCD programme to calculate $K_{l3}$ form factor in $N_f = 2+1$ Lattice QCD using domain wall fermions. We use data from several lattice spacings and different quark masses with lightest pion mass of about 170 MeV. Systematic error corresponding to interpolation in the momentum transfer is avoided using partially twisted boundary conditions. Using simulated quark masses near the physical point, reduce the systematic error due to the mass extrapolation.

This work explores different kinematic arrangements of pion and Kaon momenta for twisted boundary conditions. This thesis proposes a new ansatz for mass extrapolation. Analysing three sets of simulation data allows for a detailed study of systematic effects leading to the prediction $f_+^{K\pi}(0) = 0.9671(17)(^{+18}_{-46})$, where the first error is statistical and the second error systematic. The result allows us to extract the CKM matrix element $|V_{us}| = 0.2237(^{+13}_{-\ 8})$ and confirm unitarity of the first row CKM matrix in the Standard Model.

Also in this thesis, we discuss porting of Clover Lattice fermion action to Blue Gene-Q architecture. Clover action achieves maximum efficiency of 29.1% for single precision with good weak scaling. Strong scaling shows local volume dependency. In a study of different iterative solvers for Domain Wall Fermion action (DWF), we find that Modified Conjugate Residual(MCR) and Multishift MCR as the most efficient solver compared to CG and GCR. A new probing technique for estimating the diagonal of the inverse Dirac operator in Lattice QCD is introduced and this method is found to be closer to the exact solution than stochastic methods.

# Declaration

I do hereby declare that this thesis was composed by myself and that the work described within is my own, except where explicitly stated otherwise. This work has not been submitted for any other award or professional qualification.

The $K_{l3}$ form factor calculation discussed in Chap. 2 and Chap. 3 was performed by me in collaboration with Peter Boyle, Jonathan M. Flynn, Nicolas Garron, Andreas Juttner, Christopher Sachrajda and James Zanotti as part of the RBC-UKQCD collaboration.

I determined the parameters of our runs for $K_{l3}$ such as twist angles and performed measurements of all observables on all ensembles. These parameters were checked by Andreas Juttner. The study of the dependence of the form factor on twist angles and different kinematic choices was done by me and this led to the introduction of new kinematic that is used in the final calculation. A major update in this thesis is the way the mass extrapolation was performed and this thesis introduced a new analytic fit ansatz for mass extrapolation, that was also used in the final calculation. Data analysis was performed independently by me and this was then verified by Andreas Juttner. My complete code for data analysis is developed in $C_{++}$ by me and uses publicly available libraries GNU Scientific Library (GSL) and gnuplot-cpp.

The study of different iterative solvers for DWF and porting of Clover fermion action to Blue Gene-Q architecture (as discussed in Chap. 4) was done by me. The Clover term code was written by me using BAGEL compiler, developed by Peter Boyle. This thesis presents first attempt at studying different iterative solvers, especially Multi shift MCR for DWF and may be the most successfully optimised, publicly available Clover fermion action for Blue Gene-Q architecture.

The probing technique (as introduced in Chap. 5) for Lattice QCD was developed by me along with Eric Endress and Carlos Pena. The code for the

probing algorithm was developed by me and the integration to Lattice QCD simulations was performed by me in association with Eric Endress.

Some of the results in presented in this thesis also appear in

- **Kaon semileptonic decays near the physical point** [Boyle 12b] Published in PoS LATTICE2012 (2012) 112 [arXiv:1212.3188]
- **The kaon semileptonic form factor with near physical domain wall quarks** [Boyle 13a] Published in JHEP 1308 (2013) 132 [arXiv:1305.7217]
- **Kaon semileptonic decay from the SU(3)-symmetric point down to physical quark masses** [Juettner 13] PoS, Lattice 2013 not yet published
- **Clover fermion action for Blue Gene-Q and Iterative solvers for DWF** [Boyle 13b] PoS, Lattice 2013 not yet published

*Karthee Sivalingam*
September 2013

# Acknowledgments

During the last 3 years, Peter Boyle and James Zanotti have supervised, guided, motivated and inspired me at every stage. I am always thankful and grateful to their contribution to my thesis and life.

I would like to thank my colleagues at RBC-UKQCD collaboration, particularly Jonathan M. Flynn, Nicolas Garron, Andreas Juttner and Christopher Sachrajda for working with me in $K_{l3}$ calculations. I am thankful to Eric Endress and Carlos Pena at IFT Madrid, for working with me in the Probing project.

I would like to thank the members of Edinburgh PPT group, especially Tony Kennedy and Roger Horsley for aiding my thesis. I am grateful to Jane Patterson at graduate school for all her support(countless letters and reminders).

I acknowledge support by the European Union under the Grant Agreement number 238353(ITN STRONGnet); I also gratefully acknowledge computing time granted through the STFC funded DiRAC (Distributed Research utilising Advanced Computing) facility (grants ST/K005790/1, ST/K005804/1, ST/K000411/1, ST/H008845/1) and through the Gauss Centre for Supercomputing (GCS) (via John von Neumann Institute for Computing (NIC)) on the GCS share of the supercomputers JUGENE/JUQUEEN at Julich Supercomputing Centre (JSC).

I cannot thank my parents Sivalingam, Saraswathy; my brother Devaprasath and my wife, Brindha for all their love and affection, as they think its just what they are, and thanking them is plain stupid. I adore my daughter, Abhinaya for showing how much I can love some one, that this thesis had to wait to get completed.

# Contents

# List of Figures

# List of Tables

# List of Algorithms

# Chapter 1

# The Standard Model

## 1.1 Introduction

Until 2012, all particles seen in nature were either spin-$\frac{1}{2}$ or spin-1 particles and recently a spin-0 particle, the Higgs boson candidate was discovered to exist by recent experiments at LHC. The fermions (spin-$\frac{1}{2}$) and gauge bosons (integer spin) can be classified as:

$$\text{Fermions} \quad : \quad \begin{pmatrix} e \\ \nu_e \end{pmatrix} \begin{pmatrix} \mu \\ \nu_\mu \end{pmatrix} \begin{pmatrix} \tau \\ \nu_\tau \end{pmatrix} \quad \begin{pmatrix} u \\ d \end{pmatrix} \begin{pmatrix} s \\ c \end{pmatrix} \begin{pmatrix} t \\ b \end{pmatrix} \tag{1.1}$$

$$\text{Bosons} \quad : \quad \text{h}\ \gamma, \text{W}^{\pm}, \text{Z}^0, \text{g}_{\text{i=1...8}} \tag{1.2}$$

The Standard Model that describes the fundamental particles and their interactions, is based on the gauge symmetry group $SU(3)_c \times SU(2)_L \times U(1)_Y$. There are eight gluons mediating the $SU(3)_c$ strong interactions and four gauge bosons $(\gamma, W^{\pm}, Z^0)$ mediating the $SU(2)_L \times U(1)_Y$ electro-weak interactions. Quantum Electro dynamics(QED) is perturbative since $\alpha_e \approx \frac{1}{137}$. The Higgs mechanism makes $W^{\pm}, Z^0$ massive, resulting in a weak "weak force". The "Strong force" is strong at low energy and makes it difficult for accurate theoretical prediction in the non-perturbative sector.

## 1.2 Quantum Chromo dynamics

Quantum Chromo dynamics(QCD) is the theory of Strong interactions. The running of the strong coupling $\alpha_s(\mu)$ (where $\mu$ is the energy scale) is such that

the interactions are characterised by Infrared Confinement, $\alpha_s(\mu) \approx 1$ at hadronic scales and Asymptotic freedom, $\alpha_s(\mu) \to 0$ as $\mu \to \infty$. At leading order, the QCD coupling $\alpha_s$ is given by

$$\alpha_s = \frac{g_s^2}{4\pi}. \tag{1.3}$$

Beyond leading order, radiative corrections renormalise this coupling and the renormalised coupling runs as

$$\alpha_s(\mu^2) = \frac{1}{\beta_0 \log(\mu^2/\Lambda^2)}. \tag{1.4}$$

where $\beta_0$ depends on the renormalisation scheme used and $\Lambda$ is known as the dynamically generated dimensionful parameter of QCD. The Lagrangian for a set of quark flavors "q" with quark masses $m_q$ is as follows

$$L_{QCD} = -\frac{1}{4} F^{(a)}_{\mu\nu} F^{(a)\mu\nu} + i \sum_q \bar{\psi}^i_q \gamma_\mu (D_\mu)_{ij} \psi^j_q - \sum_q m_q \bar{\psi}^i_q \psi_{qi} \tag{1.5}$$

where $F^{(a)}_{\mu\nu} = \partial_\mu A^a_\nu - \partial_\nu A^a_\mu - g_s f_{abc} A^b_\mu A^c_\nu$ and $(D_\mu)_{ij} = \delta_{ij}\partial_\mu + i g_s \sum_a \frac{\lambda^a_{ij}}{2} A^a_\mu$.

QCD is the theory of strong nuclear force and has the quark masses as parameters. In the absence of string breaking, via. $q\bar{q}$ pair production, the strong force would give rise to a non-vanishing attractive force at asymptotically large separation. This is empirically seen as quarks are never found free. Theoretical prediction becomes difficult, as the coupling constant becomes large at small energies. Thus we have to rely on experimental measurements of hadrons and numerical simulations to verify our theoretical understanding of confined quarks and gluon.

In QCD, the continuous chiral symmetry is spontaneously broken by the quark condensate and we get massless Goldstone fields as a result. The light quark masses explicitly break the chiral symmetry, resulting in light Goldstone mesons. Ignoring the quarks with heavier mass, QCD with three quarks (u,d,s) has approximate SU(3) symmetry and the eight Goldstone bosons corresponds to generators of SU(3) symmetry. The massive fermions occur as a combination of right and left handed chiralities and only the left handed components interact with the weak bosons. The parameters of this electro-weak sector are not all precisely determined and probing these interaction provides us a good test for physics beyond Standard Model.

If we consider only two families of quarks (u,d) and (c,s), then W boson doesn't couple with the mass eigenstates $|ud\rangle$ or $|cs\rangle$ but with rotated states as follows:

$$\cos\alpha_c\,|ud\rangle + \sin\alpha_c\,|us\rangle \qquad ; \qquad -\sin\alpha_c\,|ud\rangle + \cos\alpha_c\,|us\rangle \tag{1.6}$$

where $\alpha_c$ is the Cabibbo angle [Cabibbo 63]. If we include all three families of quarks, then we get a 3x3 matrix that describes coupling of W boson to the quark states $|ud\rangle$, $|cs\rangle$ and $|tb\rangle$. This unitary matrix is called the Cabibbo-Kobayashi-Maskawa (CKM) matrix [Kobayashi 73].

## 1.3 CKM Matrix

CKM matrix describes the mixing between the electro-weak eigenstates $(d', s', b')$ with the mass eigenstates $(d, s, b)$ as shown below.

$$\begin{pmatrix} d' \\ s' \\ b' \end{pmatrix} = \begin{pmatrix} V_{ud} & V_{us} & V_{ub} \\ V_{cd} & V_{cs} & V_{cb} \\ V_{td} & V_{ts} & V_{tb} \end{pmatrix} \begin{pmatrix} d \\ s \\ b \end{pmatrix} \tag{1.7}$$

If the quark coupling of b and (d,s) quarks are neglected, the CKM matrix can be approximated to

$$V_{\mathrm{CKM}} = \begin{pmatrix} \cos\alpha_c & \sin\alpha_c & 0 \\ -\sin\alpha_c & \cos\alpha_c & 0 \\ 0 & 0 & 1 \end{pmatrix} \tag{1.8}$$

where $\alpha_c$ is the Cabibbo angle. The CKM matrix is also famously written in terms of Wolfenstein parametrisation

$$V_{\mathrm{CKM}} = \begin{pmatrix} 1-\frac{\lambda^2}{2} & \lambda & A\lambda^3(\rho+i\eta) \\ -\lambda & 1-\frac{\lambda^2}{2} & A\lambda^2 \\ A\lambda^3(1-\rho-i\eta) & -A\lambda^2 & 1 \end{pmatrix} \tag{1.9}$$

This describe a unitary matrix up to $O(\lambda^4)$ terms. Here $\lambda \equiv V_{us}$ and $A = \frac{V_{cb}}{V_{us}^2}$ are the key quantities. The CKM matrix elements are fundamental parameters

of Standard Model. It can be seen in the Yukawa sector of Standard Model Lagrangian that describes the weak interaction of quarks and hadrons.

$$\mathcal{L}_{yukawa} = \frac{g}{2\sqrt{2}}(J_h^\mu + J_l^\mu)W_\mu^+ + h.c. \tag{1.10}$$

where $J_h^\mu$ and $J_l^\mu$ are the hadronic and leptonic (Vector-Axial) currents that undergoes weak interaction.

$$J_h^\mu = (\bar{u}, \bar{c}, \bar{t})\gamma^\mu(1-\gamma^5)V_{CKM}\begin{pmatrix} d \\ s \\ b \end{pmatrix} \tag{1.11}$$

$$J_l^\mu = (\bar{\nu_e}, \bar{\nu_\mu}, \bar{\nu_\tau})\gamma^\mu(1-\gamma^5)\begin{pmatrix} e \\ \mu \\ \tau \end{pmatrix}$$

In Standard Model, the fermion mass terms arise from the Yukawa couplings to the Higgs field

$$\left(1+\frac{H}{v}\right)^{-1}\mathcal{L}_{Yukawa} = -(\bar{e}, \bar{\mu}, \bar{\tau})\begin{pmatrix} m_e & 0 & 0 \\ 0 & m_\mu & 0 \\ 0 & 0 & m_\tau \end{pmatrix}\begin{pmatrix} e \\ \mu \\ \tau \end{pmatrix} - \tag{1.12}$$

$$(\bar{u}, \bar{c}, \bar{t})\begin{pmatrix} m_u & 0 & 0 \\ 0 & m_c & 0 \\ 0 & 0 & m_t \end{pmatrix}\begin{pmatrix} u \\ c \\ t \end{pmatrix} -$$

$$(\bar{d}, \bar{s}, \bar{b})\begin{pmatrix} m_d & 0 & 0 \\ 0 & m_s & 0 \\ 0 & 0 & m_b \end{pmatrix}\begin{pmatrix} d \\ s \\ b \end{pmatrix};$$

where $H$ is the Higgs field. If we maximally diagonalise the most general gauge invariant Yukawa coupling terms by field redefinition, we find that the mass matrix $(d, s, b)$ and the electro-weak gauge couplings of the quark flavors $(d', s', b')$ are rotated relative to each other by the CKM Matrix.

Determining the value of matrix elements and testing the unitarity of the matrix is one of the main objective for constraining the Standard Model, as any deviations from unitarity would be a indication of new physics. We find

experimentally that the diagonal elements are large. Many experiments and Lattice QCD simulations have helped in determining the matrix elements. For example, using semi-leptonic decays, where flavors of mesons are changed, we can determine CKM matrix elements. Table 1.1 shows example transitions and the corresponding CKM matrix element that can be determined. The unitarity

| Transition | CKM element |
|---|---|
| $K \to \pi e \overline{\nu}$ | $V_{us}$ |
| $B \to \pi e \overline{\nu}$ | $V_{ub}$ |
| $D \to K e \overline{\nu}$ | $V_{cs}$ |

Table 1.1: CKM matrix and semi-leptonic decays

condition of the CKM matrix ensures that elements of the first row of the matrix should obey the following rule.

$$|V_{ud}|^2 + |V_{us}|^2 + |V_{ub}|^2 = 1 \tag{1.13}$$

Measuring this rule is one of the key results of this thesis. $|V_{ub}|^2$ is so small ($\approx 10^{-5}$) that it is usually approximated to zero. The value of $|V_{ud}|$ is known precisely from "superallowed" nuclear decay[Hardy 09].

$$|V_{ud}| = 0.97425(22) \tag{1.14}$$

$|V_{us}|$ can be found from Kaon, Hyperon [Cabibbo 04] and Tau decays [Maltman 09].

$$\begin{aligned} |V_{us}| &= 0.2250(27) \text{ Hyperon Decays} \\ |V_{us}| &= 0.2208(34) \text{ Tau Decays} \end{aligned} \tag{1.15}$$

Even though the above measurements from experiments are good, there are still many open issues and the precision of $|V_{us}|$ compared to $|V_{ud}|$ and $|V_{ub}|$ is very important in testing the Standard Model for deviations and possible new physics. A key topic in this thesis is to measure $V_{us}$ from semileptonic decays.

## 1.4 Semileptonic decays

Semileptonic decays involve changes to quark flavor or mixing of quarks and from these processes we can determine CKM matrix elements. $K \to \pi l \nu$ ($K_{l3}$) semileptonic decay involves coupling of $u$ and $s$ quarks and leads to the determination of $|V_{us}|$ [Colangelo 11]. In a $K_{l3}$ decay, the decay rate can be

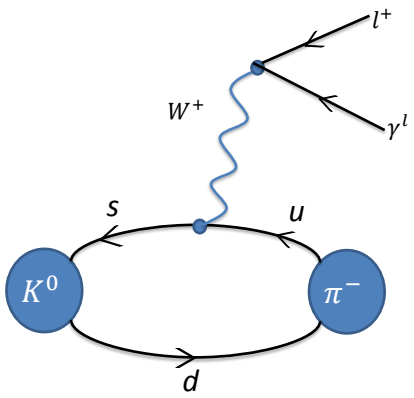


Figure 1.1: Plot showing semi-leptonic decay of $K \to \pi l \nu$

written as [Leutwyler 84]

$$\Gamma = \frac{G_F^2}{192\pi^3} M_k^5 C^2 I |V_{us}|^2 |f_+(0)|^2 S_{ew}(1+\delta_{em}) \tag{1.16}$$

where $G_F$ is the Fermi constant, $I$ is phase space integral, $S_{ew}(1+\delta_{em})$ is the radiative correction, $C^2 = 1(1/2)$ is the Clebsch-Gordon coefficient and $M_k$ is the kaon mass. The value of $I$ is estimated to approximately 0.154 for $K^0_{e3}$ and 0.102 for $K^0_{\mu 3}$ [Alexopoulos 04], value of $S_{ew}$ determined precisely as 1.022 [Sirlin 82]. The electromagnetic piece $(1+\delta_{em})$ is small correction and doesn't contribute much to the error in $\Gamma$. Thus the product $|V_{us}|^2|f_+(0)|^2$ can be precisely estimated from experiments of semileptonic $K \to \pi$ decay rate [Antonelli 10]. A precise theoretical determination of $f_+(0)$ is required for estimating the value of $V_{us}$.

$f_+(0)$ is defined from the strangeness changing weak current ($V_\mu = \bar{s}\gamma_\mu u$) as

$$\langle \pi(p') \big| V_\mu \big| K(p) \rangle = (p_\mu + p'_\mu) f_+(q^2) + (p_\mu - p'_\mu) f_-(q^2) \tag{1.17}$$

where $q^2 = (p - p')^2$. In the SU(3) flavor limit ($m_u = m_d = m_s$), $f_+(0) = 1$, due to charge conservation. We can expect small SU(3) breaking effects in $f_+(0)$. $f_+(0)$ can be expanded in terms of the meson masses as

$$f_+(0) = 1 + f_2 + f_4 + \dots \tag{1.18}$$

As a result of Ademollo-Gatto theorem [Ademollo 64], $f_2$ can be calculated directly from masses $m_k$, $m_\pi$ and pion decay constant $f_\pi$ [Gasser 85]. If we can write the expansion as

$$\Delta f = f_+(0) - (1 + f_2) \tag{1.19}$$

then the only quantity that needs to be determined is $\Delta f$. Until recently, standard result from Leutwyler and Roos (LR) is $\Delta f = 0.016(8)$ [Leutwyler 84, Bijnens 03]. Lattice methods offer an alternate method to calculate the value of $f_+(0)$ non perturbatively [Hashimoto 99, Becirevic 05b, Boyle 07, Boyle 10, Gamiz 12]. Using Lattice methods, $f_+^{K\pi}(0)$ has been determined to a precision of $\approx 0.5\%$ [Lubicz 09, Boyle 08b, Boyle 10, Kaneko 11, Bazavov 12, Gamiz 12]. A key part of this thesis is to determine $f_+^{K\pi}(0)$ from ($K_{l3}$) semileptonic decay as discussed in Ch. 2 and Ch. 3.

## 1.5 Lattice QCD

For precise determination of $K_{l3}$ form factor, we are interested in determining hadronic matrix element $\langle \pi(p') \big| V_\mu \big| K(p) \rangle$ in (1.17), that mediates the $K_{l3}$ semileptonic decays. While the weak interacting theories are understood by perturbation theory, perturbative methods for QCD at low energy becomes difficult due to the strength of the coupling constant.

Non perturbative methods like Lattice QCD are the only way to solve QCD in this regime. Lattice QCD provides us a tool to verify our understanding of QCD by formulating the theory in a discrete lattice. Though space-time symmetries are lost, the lattice respects local gauge symmetries. High frequencies are lost due to discretisation, with momentum cutoff proportional to the inverse lattice spacing $1/a$. We choose a suitable lattice volume (L) and size (a) and evaluate Feynman path integral by generating ensemble of fields and then measuring

physical quantities from them.

In evaluating the physical observables $\mathcal{O}$, expectation value of operator should be calculated.

$$\langle \mathcal{O} \rangle = 1/Z \int \mathcal{D}\phi \, \mathcal{O}(\phi) \, \exp(-S(\phi)) \tag{1.20}$$

where $S(\phi)$ is the action and Z is the partition function. In Lattice QCD, we have one integration per degree of freedom and the numerical evaluation becomes expensive for even small volumes. We use Monte-Carlo methods to importance sample the integration. The expectation value is evaluated by generating many gauge field configurations $(\phi_1, \phi_2, \phi_3, ...)$ with the probability $1/Z \exp(-S)$. The operator $\mathcal{O}$ is evaluated on each of the configurations and the average value is determined.

$$\mathcal{O}_{avg} = \frac{1}{N} \sum_{t=1}^{N} \mathcal{O}(\phi_t) \tag{1.21}$$

As the number of gauge field configurations tends to infinity,

$$\langle \mathcal{O} \rangle = \lim_{N \to \infty} \mathcal{O}_{avg} \tag{1.22}$$

we obtain the expectation value of the observable.

In Lattice QCD the aim is to transcribe the gauge action and Dirac operator for fermions on a discrete space-time lattice so that ideally all important symmetries of QCD like gauge invariance, chiral symmetry are present.

### 1.5.1 Lattice gauge action

In constructing the gauge fields on a discrete lattice, Wilson formulated the gauge group (SU(3)) elements to live on the links that connect the sites and constructed a plaquette ($W_{\mu\nu}$).

$$W_{\mu\nu}^{1\times1} = \mathrm{Re\ Tr}\left(\mathrm{U}_\mu(\mathrm{x})\mathrm{U}_\nu(\mathrm{x}+\hat{\mu})\mathrm{U}_\mu^\dagger(\mathrm{x}+\hat{\nu})\mathrm{U}_\nu^\dagger(\mathrm{x})\right) \tag{1.23}$$

The trace of the product of path ordered link variables preserves gauge invariance and leads to term proportional to $F_{\mu\nu}F^{\mu\nu}$ in its Taylor expansion in "$a$". The

Wilson gauge action is

$$S_{\mathrm{G}}(U) = \frac{6}{g^2} \sum_x \sum_{\mu<\nu} \mathrm{Re\,Tr}\, \frac{1}{3}(1 - W_{\mu\nu}^{1\times 1}) \tag{1.24}$$

We can improves this gauge action by taking linear combination of loops that will remove the "$a^n$" terms in the Taylor expansion. The improved gauge action $S_G$ is of the form

$$S_{\mathrm{G}}[U] = -\frac{\beta}{3}\left[(1 - 8\,c_1) \sum_{x;\mu<\nu} P[U]_{x,\mu\nu} + c_1 \sum_{x;\mu\neq\nu} R[U]_{x,\mu\nu}\right] \tag{1.25}$$

where $P[U]_{x,\mu\nu}$ and $R[U]_{x,\mu\nu}$ the real part of the trace of the path ordered product of link variables around the $1 \times 1$ plaquette and $1 \times 2$ rectangle, respectively and $\beta \equiv 6/g^2$. The commonly used the Iwasaki action sets $c_1 = -0.331$ [Iwasaki 85, Iwasaki 84]. In coarser lattices, the number of low modes developed by Iwasaki gauge action increases and the residual chiral symmetry breaking increases. These low modes are suppressed by adding a weighting term, giving the Dislocation Suppressing Determinant Ratio (DSDR) action [Kelly 11].

### 1.5.2 Lattice fermions

The naive discretisation of the Dirac fermion action replaces the derivative with a finite difference and uses gauge links to maintain gauge invariance.

$$\bar{\psi} \not{D} \psi = \frac{1}{2a}\bar{\psi}(x) \sum_\mu \gamma_\mu (U_\mu(x)\psi(x+\hat{\mu}) - U_\mu^\dagger(x-\hat{\mu})\,\psi(x-\hat{\mu})) \tag{1.26}$$

The simplest fermion action is as follows

$$\begin{aligned} S_L &= m_q \sum_x \bar{\psi}(x)\psi(x) \\ &\quad + \frac{1}{2a} \sum_x \sum_\mu \bar{\psi}(x)\gamma_\mu (U_\mu(x)\psi(x+\hat{\mu}) - U_\mu^\dagger(x-\hat{\mu})\psi(x-\hat{\mu})) \\ &\equiv \sum_x \bar{\psi}(x) M_{xy}[U] \psi(y) \end{aligned} \tag{1.27}$$

where $M$ is the interaction matrix

$$M_{i,j}[U] \;=\; m_q\delta_{ij} \;+\; \frac{1}{2a}\sum_{\mu}\;\left[\gamma_\mu U_{i,\mu}\delta_{i,j-\mu} \;-\; \gamma_\mu U^{\dagger}_{i-\mu,\mu}\delta_{i,j+\mu}\right] \tag{1.28}$$

The above lattice action exhibits chiral symmetry as $\{\gamma_5, M\}$=0 for $m_q = 0$ but has a problem of doubling. The Doubling problem can be seen from the Fourier representation

$$S_L(p) \;=\; m_q \;+\; \frac{i}{a}\sum_{\mu}\gamma_\mu\;\sin p_\mu a \tag{1.29}$$

which gives rise to $2^d$ flavors instead of one.

### Wilson Fermion

Wilson's solution to doublers was to add the Wilson term

$$S_W = S_L + \frac{r}{2a}\sum_{x}\sum_{\mu}\bar{\psi}(x)(U_\mu(x)\psi(x+\hat{\mu}) - 2\psi(x) + U^{\dagger}_{\mu}(x-\hat{\mu})\psi(x-\hat{\mu})) \tag{1.30}$$

so that we have only one low energy solution at $p_\mu$=0 and other solutions at $p_\mu = \pi/a$ become massive and decouple in continuum limit.

$$S_W(p) \;=\; m_q \;+\; \frac{i}{a}\sum_{\mu}\gamma_\mu\;\sin p_\mu a + \;\frac{1}{a}\sum_{\mu} 1 - \cos p_\mu a \tag{1.31}$$

Adding such irrelevant terms not only increases the complexity and computational cost, but also explicitly breaks the chiral symmetry.

### Clover Fermion

$O(a)$ improved clover action was proposed by Sheikholeslami and Wohlert [Sheikholeslami 85] which builds on the Wilson action with the fix for doublers by adding higher dimensional term to remove or reduce $O(a)$ errors

$$S_{\text{clover}} \;=\; S_W - \frac{C_{SW}}{4}\sum_{\mu<\nu}\;\bar{\psi}(x)\sigma_{\mu\nu}F_{\mu\nu}\psi(x)\;. \tag{1.32}$$

Here the value of $C_{SW}$ can be determined by perturbative or non-perturbative methods and determines the improvement. The cost of this method is comparable

to that of Wilson fermions. For both Wilson and Clover fermion actions, $m_q$ is additively renormalised and leaves us to determine numerically the value of $m_q$ where $m_\pi \to 0$. As a part of this thesis, we discuss porting and optimisation of Clover fermion action to Blue Gene-Q architecture in Ch. 4.

### Domain Wall Fermion

Many different methods were developed to resolve the doubling problem and still preserve chiral symmetry and significant among them is the Domain Wall Fermion(DWF) action. Kaplan [Kaplan 92] and Shamir [Shamir 93] extended the Wilson fermion into fifth dimension ($L_s$) with left handed and right handed fermions residing on the opposite walls of the fifth dimension. The DWF action is defined as

$$S_{\rm DWF} \ = \bar{\psi} D^{\rm DWF}(x)\psi(x) \ . \tag{1.33}$$

with the domain wall fermion operator $D^{\rm DWF}$, for a fermion of mass $m_f$, defined as

$$D^{\rm DWF}_{x,s;x',s'}(M_5, m_f) = \delta_{s,s'} D^{\parallel}_{x,x'}(M_5) + \delta_{x,x'} D^{\perp}_{s,s'}(m_f) \tag{1.34}$$

$$\begin{aligned} D^{\parallel}_{x,x'}(M_5) \ &= \ \frac{1}{2}\sum_{\mu=1}^{4}\Big[(1-\gamma_\mu)U_{x,\mu}\delta_{x+\hat{\mu},x'} + (1+\gamma_\mu)U^{\dagger}_{x',\mu}\delta_{x-\hat{\mu},x'}\Big] \\ &+ \ (M_5 - 4)\delta_{x,x'} \end{aligned} \tag{1.35}$$

$$\begin{aligned} D^{\perp}_{s,s'}(m_f) \ &= \ \frac{1}{2}\Big[(1-\gamma_5)\delta_{s+1,s'} + (1+\gamma_5)\delta_{s-1,s'} - 2\delta_{s,s'}\Big] \\ &- \ \frac{m_f}{2}\Big[(1-\gamma_5)\delta_{s,L_s-1}\delta_{0,s'} + (1+\gamma_5)\delta_{s,0}\delta_{L_s-1,s'}\Big]. \end{aligned} \tag{1.36}$$

The gauge fields are same on each slice with the gauge links set to unity except for the boundaries or walls. The mixing between two chiral components reduces exponentially as $(L_s) \to \infty$. So at $(L_s) = \infty$ and finite $a$, we have exact chiral symmetry. The $O(a)$ discretisation error reduces exponentially as the size of $(L_s)$ increases. For finite $L_s$, chiral symmetry is slightly broken and this is measured as the residual mass $m_{res}$. For DWF, error for all practical purposes are $O(a^2)$ and $O(a^4)$, with odd powers of $a$ eliminated by exponentially suppressed chiral symmetry breaking.

### 1.5.3 Dynamical fermions

Dynamical fermions make Lattice QCD expensive. Fermions are Grassmann variables and cannot be simulated on a computer directly. Field theory is implemented using Feynman path integral approach and the generating functional can be written on a Lattice as follows

$$Z = \int \mathcal{D}A_\mu \mathcal{D}(\psi, \bar{\psi}) \exp(-S) \tag{1.37}$$

where where $S = \int d_4x(\frac{1}{4}F_{\mu\nu}F^{\mu\nu} - \bar{\psi}\mathcal{M}\psi)$, $\mathcal{M}$ is the fermion matrix. The fermions $\psi$ and $\bar{\psi}$ are represented using Grassmann variables and can be easily integrated out. The action can be represented as

$$S = S_{gauge} + S_{quarks} = \int d_4x \frac{1}{4}F_{\mu\nu}F^{\mu\nu} - \sum_i \log(\det(\mathcal{M}_i)) \tag{1.38}$$

Now the integral is only over background gauge configurations and action depends on the fermion determinant. Thus for generation of gauge fields using Monte Carlo methods, determinant of $\mathcal{M}$ should be evaluated for each gauge configuration. With $L^3 \times T \times 12$ rows and columns, the computation of $\det(\mathcal{M})$ is very expensive and we shall use stochastic methods to compute. If $\det \mathcal{M}$ is set to a constant value, we have the quenched approximation.

The physical quantities can be calculated by evaluating the expectation values of operators ($\mathcal{O}$)

$$\langle \mathcal{O} \rangle = \frac{1}{Z} \int \mathcal{D}A_\mu \mathcal{O} \exp(-S) \tag{1.39}$$

where Z is a normalisation constant defined in (1.37). The physical observables are calculated by using suitable operators and then studying the large $t$ behaviour. As the fermion fields are integrated out, all integrals should be expressed in terms of gauge fields. For a observable $\mathcal{O}(\phi, \bar{\psi}, \psi)$, integration over fermion fields is done by adding source terms ($\bar{\psi}\sigma + \bar{\sigma}\psi$).

$$\hat{\mathcal{O}}(\phi, \bar{\psi}, \psi) = \mathcal{O}(\phi, \frac{\partial}{\partial\sigma_x}, \frac{\partial}{\partial\sigma_y}) \exp(\sigma_x M(\phi)^{-1}\sigma_y) \mid_{\sigma_x=\sigma_y=0} \tag{1.40}$$

Fermion determinant is extensive and expensive and can be expressed in terms of Gaussian integrals of gauge fields called "pseudofermions". To ensure that the

matrix is positive definite, fermion determinant is expressed for even number of flavors.

$$\det(\mathcal{M}(\phi))^2 = \det(\mathcal{M}(\phi)\mathcal{M}^\dagger(\phi)) \propto \int d\bar{\chi} d\chi \exp[-\bar{\chi}(\mathcal{M}^\dagger\mathcal{M})^{-1}\chi] \tag{1.41}$$

From the above relations, it is clear that solution to the system $\mathcal{M}\mathcal{M}^\dagger\psi = \chi$ should be evaluated. In Lattice QCD this is normally done using iterative solvers like Conjugate Gradient (CG). As a part of this thesis, we investigate different iterative solvers for DWF in Ch. 4.

## 1.6 Hybrid Monte-Carlo

Hybrid Monte-Carlo (HMC) method is usually used to generate the gauge configurations. The method introduces a momentum $p$ corresponding to degree of freedom $\phi$, so that the Hamiltonian $\mathcal{H}$ is

$$\mathcal{H} = p^2 + S(\phi) \tag{1.42}$$

At each step of the evolution, $S(\phi)$ is updated using Molecular dynamics evolution, $p$ is selected randomly from a momentum heat-bath and then accepted or rejected based on Metropolis algorithm.

Using HMC, the fermion determinant in (1.41) is evaluated on each of the configurations using pseudofermions. Usually even number of pseudofermion fields are used to aid the evaluation of fermion determinant. For odd number of pseudofermion fields, we take $\det((\mathcal{M}\mathcal{M}^\dagger)^{1/2})$.

Pseudofermion field at each step can be selected from a random Gaussian noise and rational approximation is used to approximate the pseudofermions and MD evolution. This algorithm is referred to as RHMC [Clark 04] [Clark 05]. Rational approximation is done using partial fraction expansion. For eg.

$$\frac{1}{\sqrt{x}} \approx 0.3904603901 + \frac{0.0511093775}{x+0.0012779193} + \frac{0.1408286237}{x+0.0286165446} + \frac{0.5964845033}{x+0.4105999719}. \tag{1.43}$$

As the denominator in the rational expansion are shifts of the fermion determinant, we can use multi-shift solvers to reduce cost of solving the multiple linear system of equations in parallel. As a part of this thesis, we investigate an improved

multi-shift MCR solver in Ch. 4.

## 1.7 Measurement of Observables

As shown in the previous section, CKM Matrix elements and masses are calculated from correlation functions. The two-point correlation function for a meson propagator with quarks $h$ and $l$ can be written as

$$C_i(t,\vec{p}_i) = \sum_{\vec{x}} e^{i\vec{p}_i\cdot\vec{x}} \langle 0|Tr\{\bar{h}(x)\gamma^5 l(x)\bar{l}(0)\gamma^5 h(0)\}|0\rangle, \tag{1.44}$$

Using Wick's theorem, the above trace can be written as a product of quark propagators $(H, L)$

$$C_i(t,\vec{p}_i) = \sum_{\vec{x}} e^{i\vec{p}_i\cdot\vec{x}} \langle Tr\{H^\dagger(x,0)\, L(x,0)\}\rangle, \tag{1.45}$$
$$H(x,0) = \langle 0|h(x)\bar{h}(0)|0\rangle,$$
$$L(x,0) = \langle 0|l(x)\bar{l}(0)|0\rangle$$

In all the above relations, the trace is over spin and colour indices and is not denoted for simplicity. From (1.39), quark propagators are measured in a Lattice as follows

$$\begin{aligned}\langle 0|\psi(x)\bar{\psi}(y)|0\rangle &= \frac{1}{Z}\int \mathcal{D}A_\mu \psi(x)\bar{\psi}(y)\exp(-S) \\ &= \frac{1}{Z}\int \mathcal{D}A_\mu \mathcal{M}^{-1}(x,y)\exp(-S)\end{aligned} \tag{1.46}$$

Similarly the three-point function can also be constructed from quark propagators and measure in a lattice simulation.

Quark propagator matrix are large and it will be very expensive to determine all the elements. So only a subset is calculated. In general a point source, with unit spin-colour vectors at a single space-time location, is used. This source will require 12 inversions for each spin and colour. This source suffers from local Gauge fluctuations. The subset generated from point sources contains only elements of the propagator from one source to all other source locations (one to all propagator).

One source operator that is of particular interest is the Z2PSWall [Boyle 08a] that is used in this work. For such stochastic sources [Foster 99, McNeile 06], a set of sources ($N_{hits}$) contains elements randomly selected from a Distribution $\mathcal{D}$, symmetric about zero. They are usually used to compute the all the elements of the propagator. Using $\mathcal{D} = \mathbb{Z} \times \mathbb{Z}$ ($\mathbb{Z} = \{+1, -1\}$) noise source, all to all propagators can be calculated. These propagators are very noisy and are not preferred unless required. For pseudoscalar mesons, this source reduces the two pt-correlation function to a scalar product of two solution vectors as follows

$$\mathcal{M}(x, y) = \frac{1}{N} \sum_{n} \langle \Phi(x) \cdot \bar{\Phi}(y) \rangle \tag{1.47}$$

Thus this can be evaluated from a single inversion per $N_{hit}$. For large enough gauge configurations, only a few $N_{hit}$ need be used as increasing the $N_{hit}$ doesn't improve. The sources may be affected by gauge correlation and so the are placed at different time location so that any correlation does not affect the statistical noise. The measured correlation functions from different sources are usually averaged. Only the ground state is of interest and the source and sink operators are separated large enough to reduce any contamination from excited states.

In this thesis, we discuss a new measurement technique to determine the complete quark propagator matrix in Chap. 5.

## Chapter 2

# The $K_{l3}$ Form-factor

## 2.1 The $K_{l3}$ form factor

The $K_{l3}$ form factor $f_+^{K\pi}(0)$ at zero momentum transfer is of considerable importance in determining the CKM matrix element $V_{us}$. From the relation in (1.17), we can define the scalar form factor as

$$f_0^{K\pi}(q^2) = f_+^{K\pi}(q^2) + \frac{q^2}{m_K^2 - m_\pi^2} f_-^{K\pi}(q^2)\,, \tag{2.1}$$

from the above relation we have $f_0^{K\pi}(0) = f_+^{K\pi}(0)$. Calculation of $f_+^{K\pi}(0)$ begins with the measurement of pion and kaon correlation functions. The 2-point correlation function is defined as

$$C_i(t,\vec{p}_i) = \sum_{\vec{x}} e^{i\vec{p}_i\cdot\vec{x}} \langle\, O_i(t,\vec{x})\, O_i^\dagger(0,\vec{0})\,\rangle = \frac{|Z_i|^2}{2E_i}\left(e^{-E_i t} + e^{-E_i(T-t)}\right) \tag{2.2}$$

We define the 3-point function between initial and final states $P_i$ and $P_f$ of the weak vector current $V_\mu$

$$\begin{aligned} C_{P_iP_f}(t_i,t,t_f,\vec{p}_i,\vec{p}_f) &= \sum_{\vec{x}_f,\vec{x}} e^{i\vec{p}_f\cdot(\vec{x}_f-\vec{x})} e^{i\vec{p}_i\cdot\vec{x}} \langle\, O_f(t_f,\vec{x}_f)\, V_4(t,\vec{x})\, O_i^\dagger(t_i,\vec{0})\,\rangle \\ &= \frac{Z_i\, Z_f}{4E_iE_f} \langle\, P_f(\vec{p}_f)\,|\,V_4(0)\,|\,P_i(\vec{p}_i)\,\rangle \\ &\times \left\{\theta(t_f-t)\, e^{-E_i(t-t_i)-E_f(t_f-t)} \;-\; \theta(t-t_f)\, e^{-E_i(T+t_i-t)-E_f(t-t_f)}\right\} \end{aligned} \tag{2.3}$$

In the above relations, the states $i, f$ can be kaon($K$) or pion($\pi$) and the corresponding operators for mesons are $O_K = \bar{s}\gamma_5 q$ and $O_\pi = \bar{q}\gamma_5 q$. The constants

have the following definitions $Z_f = \langle\, 0 \,|\, O_f(0,\vec{0})|\, P_f \,\rangle$; $Z_i = \langle\, P_i \,|\, O_i^{\dagger}(0,\vec{0}) \,|\, 0 \,\rangle$. In practice, the values of $t_i$ and $t_f$ are fixed and we assume large time behaviour. We can normalise the local vector current in (2.4) by multiplying it with normalisation constant $Z_V$.

$$Z_V = \frac{\tilde{C}_\pi(t_f,\vec{0})}{C_{\pi\pi}^{(B,0)}(t_i,t,t_f,\vec{0},\vec{0}\,)}\,. \tag{2.4}$$

where B refers to the bare vector current. The main aim is to calculate $f_0^{K\pi}(0)$. From (1.17), we know that this can be calculated from the weak matrix element $\langle\, P_f(\vec{p}_f) \,|\, V_4(0) \,|\, P_i(\vec{p}_i) \,\rangle$. This matrix element can be computed by constructing ratios of the correlation functions (2.2) and (2.4), such that the exponential and constant terms can be cancelled out. We can define three ratios as follows

$$\begin{aligned}
R_{1,\,P_iP_f}(\vec{p}_i,\vec{p}_f) &= 4\sqrt{E_iE_f}\,\sqrt{\frac{C_{P_iP_f}(t,\vec{p}_i,\vec{p}_f)\,C_{P_fP_i}(t,\vec{p}_f,\vec{p}_i)}{C_{P_i}(t_f,\vec{p}_i)\,C_{P_f}(t_f,\vec{p}_f)}},\\
R_{2,\,P_iP_f}(\vec{p}_i,\vec{p}_f) &= 2\sqrt{E_iE_f}\,\sqrt{\frac{C_{P_iP_f}(t,\vec{p}_i,\vec{p}_f)\,C_{P_fP_i}(t,\vec{p}_f,\vec{p}_i)}{C_{P_iP_i}(t,\vec{p}_i,\vec{p}_i)\,C_{P_fP_f}(t,\vec{p}_f,\vec{p}_f)}},\\
R_{3,\,P_iP_f}(\vec{p}_i,\vec{p}_f) &= 4\sqrt{E_iE_f}\,\frac{C_{P_iP_f}(t,\vec{p}_i,\vec{p}_f)}{C_{P_f}(t_f,\vec{p}_f)}\,\sqrt{\frac{C_{P_i}(t_f-t,\vec{p}_i)\,C_{P_f}(t,\vec{p}_f)\,C_{P_f}(t_f,\vec{p}_f)}{C_{P_f}(t_f-t,\vec{p}_f)\,C_{P_i}(t,\vec{p}_i)\,C_{P_i}(t_f,\vec{p}_i)}}\,.
\end{aligned} \tag{2.5}$$

For large t, all the above ratios are equal to the weak matrix element.

$$R_{1,2,3} = \langle\, P_f(\vec{p}_f) \,|\, V_4(0) \,|\, P_i(\vec{p}_i) \,\rangle \tag{2.6}$$

$f_0^{K\pi}(q^2_{max})$ can be computed precisely from the relation

$$R_{2;K\pi}(\vec{0},\vec{0}) = f_0^{K\pi}(q^2_{\rm max})(m_K + m_\pi)\,. \tag{2.7}$$

where $q^2_{max} = (m_K - m_\pi)^2$. Also $f_0^{K\pi}(0)$ can be evaluated by computing $f_0^{K\pi}(q^2)$ at different $q^2$ and then interpolating it to $q^2 = 0$ using a suitable ansatz [Boyle 08b]. For interpolation, the value of $f_+(q^2)$ is calculated at different values of $q^2$ from the relations below.

$$\begin{aligned}
F(p_K,p_\pi) &= \tfrac{f_+(q^2)}{f_0(q^2_{max})}(1 + \tfrac{E_k(p_K)-E_\pi(p_\pi)}{E_k(p_K)+E_\pi(p_\pi)}\xi(q^2)),\\
\xi(q^2) &= \tfrac{f_-(q^2)}{f_+(q^2)}\\
F(p_K,p_\pi) &= \tfrac{m_K+m_\pi}{E_K(\vec{p}_K)+E_\pi(\vec{p}_\pi)}\,\tfrac{C_{K\pi}(t,\vec{p}_K,\vec{p}_\pi)\,C_K(t,\vec{0})\,C_\pi(t_f-t,\vec{0})}{C_{K\pi}(t,\vec{0},\vec{0})\,C_K(t,\vec{p}_K)\,C_\pi(t_f-t,\vec{p}_\pi)}.
\end{aligned} \tag{2.8}$$

By determining $F(p_K, p_\pi)$ and $\xi(q^2)$, we can compute $f_+(q^2)$ and $f_-(q^2)$ at different $q^2$.

The above approach suffers from error due to interpolation. Also different ansatz may result in different result for the scalar form factor and this will add to the systematic uncertainties[Tsutsui 06] [Dawson 06]. In a lattice of volume $V = L^3 \times T$ with periodic boundary condition, the momentum are quantised as $p_i = \frac{2\pi}{L} \times i$, where $i$ is an integer. And the lowest non-zero momentum that can be simulated is $\frac{2\pi}{L}$. This makes it difficult to evaluate scalar form factor directly at $q^2 = 0$.

Twisted boundary condition is a non-periodic technique which allows momentum smaller than $\frac{2\pi}{L}$ to be evaluated in a Lattice [Bedaque 05] [Boyle 04]. For a quark field, the twisted boundary condition is given by

$$q(x_i + L) = \exp\left(i\,\theta_i/L\,\right) q(x_i) \tag{2.9}$$

where $\theta_i$ is the twist. Redefinition of quark fields result in quarks interacting with a external field with coupling proportional to the twist, $\theta_i/L$. This allows the momentum to be shifted by $\theta_i/L$. Though this can be applied to both sea and valence quarks, it is usually applied only to valence quarks [Sachrajda 05].

Twisting boundary conditions are usually implemented in the lattice by modifying the gauge links so that $U_i(x) \rightarrow U_i(x)\,\exp(i\theta_i/L)$. For example, we can consider the term

$$\bar{\psi}(x)\,U_\mu(x)\,\psi(x+\mu) \tag{2.10}$$

that appears in the Wilson fermion action (1.30). After phase change $\psi(x) \rightarrow \psi(x)\,e^{i\phi(x)}$, this term can be written as

$$\bar{\psi}(x)\,e^{-i\phi(x)}\,U_\mu(x)\,e^{i\phi(x+\mu)}\,\psi(x+\mu) = \bar{\psi}(x)\,e^{i(\phi(x+\mu)-\phi(x))}\,U_\mu(x)\,\psi(x+\mu) \tag{2.11}$$

With $\phi(x) = x\theta_x + y\theta_y + z\theta_z$,

$$\bar{\psi}(x)\,e^{i(\phi(x+\mu)-\phi(x))}\,U_\mu(x)\,\psi(x+\mu) = \bar{\psi}(x)\,e^{i\theta_\mu}\,U_\mu(x)\,\psi(x+\mu) \tag{2.12}$$

This implies that we can multiply $U_\mu(x)$ by $e^{i\theta_\mu}$ to implement twisted boundary condition.

For $K \rightarrow \pi$ decay, valence quarks with a twisted boundary condition (with

twist $\theta$), the dispersion relation of the meson is given by [de Divitiis 04, Flynn 06]

$$E = \sqrt{m^2 + \left(\vec{p}_{\rm FT} + \frac{\vec{\theta}}{L}\right)^2}, \tag{2.13}$$

With this, the momentum transfer can be rewritten as [Boyle 07]

$$q^2 = (p_i - p_f)^2 = [E_i(\vec{p}_i) - E_f(\vec{p}_f)]^2 - [(\vec{p}_{{\rm FT},i} + \frac{\vec{\theta}_i}{L}) - (\vec{p}_{{\rm FT},f} + \frac{\vec{\theta}_f}{L})]^2 \,. \tag{2.14}$$

By adjusting the twists on the mesons $(K, \pi)$, we can evaluate form factor exactly at $q^2 = 0$. An easier approach will be to keep either kaon or pion at rest and adjust the twist on the other meson to get $q^2 = 0$. For ratios in (2.5) the pion or kaon twist required to get $q^2 = 0$ is calculated as follows.

$$\begin{aligned} &R_{\alpha,K\pi}(\vec{p}_K, \vec{0}) \quad \text{with} \quad |\vec{\theta}_K| = L\sqrt{(\tfrac{m_K^2+m_\pi^2}{2m_\pi})^2 - m_K^2} \quad \text{and} \quad \vec{\theta}_\pi = \vec{0} \\ &R_{\alpha,K\pi}(\vec{0}, \vec{p}_\pi) \quad \text{with} \quad |\vec{\theta}_\pi| = L\sqrt{(\tfrac{m_K^2+m_\pi^2}{2m_K})^2 - m_\pi^2} \quad \text{and} \quad \vec{\theta}_K = \vec{0}\,, \end{aligned} \tag{2.15}$$

where $\alpha = 1, 2, 3$. Now form factor, $f^0_{K\pi}(0)$ is evaluated directly at $q^2 = 0$ using the relation below.

$$f^0_{K\pi}(0) = \frac{R_{\alpha,K\pi}(\vec{p}_K, \vec{0})(m_K - E_\pi) - R_{\alpha,K\pi}(\vec{0}, \vec{p}_\pi)(E_K - m_\pi)}{(E_K + m_\pi)(m_K - E_\pi) - (m_K + E_\pi)(E_K - m_\pi)} \qquad (\alpha = 1, 2, 3)\,. \tag{2.16}$$

This relationship is obtained by considering the $V_4$ or time component of the weak vector current in (1.17). Using all the other components of the weak vector current, we can obtain a system of equations which we can solve to obtain the form factor. The equations are listed below.

$$\begin{aligned} R_{\alpha,K\pi}(\vec{\theta}_K, \vec{0}, V_4) &= f^+_{K\pi}(0)\,(E_K + m_\pi) + f^-_{K\pi}(0)\,(E_K - m_\pi) \\ R_{\alpha,K\pi}(\vec{0}, \vec{\theta}_\pi, V_4) &= f^+_{K\pi}(0)\,(m_K + E_\pi) + f^-_{K\pi}(0)\,(m_K - E_\pi) \\ R_{\alpha,K\pi}(\vec{\theta}_K, \vec{0}, V_i) &= f^+_{K\pi}(0)\,\theta_{K,i} + f^-_{K\pi}(0)\,\theta_{K,i} \\ R_{\alpha,K\pi}(\vec{0}, \vec{\theta}_\pi, V_i) &= f^+_{K\pi}(0)\,\theta_{\pi,i} - f^-_{K\pi}(0)\,\theta_{\pi,i}\ . \end{aligned} \tag{2.17}$$

Separately solving each of these equations can result in much larger error and this can be overcome by simultaneously solving all the equations corresponding to all

the components of the vector current $V_\mu$ and then performing $\chi^2$ minimisation. In evaluating $f^+_{K\pi}(0)$, it is important to estimate the systematic errors. As noted above, lattice with finite spacing results in discretisation errors and finite volume effects. Even though, twisted boundary condition can completely eliminate error due to $q^2$ interpolation, the simulated quarks are at unphysical masses and would require mass extrapolation [Boyle 10].

## 2.2 $K_{l3}$ in Lattice QCD

The form-factor $f_+(q^2 = 0)$ from $K_{l3}$ semi-leptonic decays is of considerable interest and has been calculated independently by collaborations using different lattice spacings and lattice actions. The $K_{l3}$ form factor has been successfully calculated by many collaboration, with $N_f = 2$ [Tsutsui 06, Dawson 06, Lubicz 09, Lubicz 10] and $N_f = 2+1$ [Kaneko 11, Bazavov 12] dynamical quarks and the details of their calculations can be found in [Colangelo 11].

The RBC-UKQCD collaboration has previously computed the form-factor using $N_f = 2 + 1$ flavors of domain wall quarks [Boyle 08b]. Their study used $N_f = 2 + 1$ dynamical flavors, generated from Iwasaki gauge action at $\beta = 2.13$ ($a^{-1} = 1.73$GeV) [Allton 08] and domain wall fermion action with strange quark mass close to the physical mass. The calculations were performed with four values of rather heavy light quark masses ($am_{ud} = 0.005$, 0.01, 0.02, 0.03) and two different volumes, $16^3$ and $24^3$ (24Coarse). The result from the analysis was,

$$f_+(0)^{K\pi} = \quad 0.9599(34)_{stat}(^{+31}_{-43})_{chiral}(14)_a\,, \tag{2.18}$$

The errors quoted are statistical, due to Chiral extrapolation and Lattice cut-off effects respectively. In this study, the $16^3$ data was ignored due to its poor quality and the study was performed using single lattice spacing. The pion and kaon masses used in the simulations were much larger than the physical values ($m_\pi > 333\,\text{MeV}$). This gave rise to rather large chiral and "a" errors as shown above. This chapter describes the work performed in reducing these errors by adding new calculations with simulations using considerably lighter pion masses down to 170 MeV and at two additional lattice spacings.

## 2.3 Ensembles

This chapter discusses the new analysis done in this thesis by adding new ensembles 32Fine [Aoki 11], 32Coarse [R.Arthur 12] (cf. table 2.1) to the RBC-UKQCD data-set and also by recomputing the form-factor on 24Coarse ensembles using twisted boundary conditions. We also introduce a new method for the mass extrapolation of data.

| Label | Size | $S_G$ | $\beta$ | $a^{-1}$ | $m_\pi$( MeV) |
|---|---|---|---|---|---|
| 24Coarse | $24^3 \times 64 \times 16$ | Iwasaki | 2.13 | 1.75(4) | 333, 422, 562, 678 |
| 32Fine | $32^3 \times 64 \times 16$ | Iwasaki | 2.25 | 2.31(4) | 294, 349, 399 |
| 32Coarse | $32^3 \times 64 \times 32$ | Iwasaki+DSDR | 1.75 | 1.37(1) | 171, 247 |

Table 2.1: A summary of the three ensembles used in this analysis. Here '$S_G$' denotes the Gauge action, '$m_\pi$' the pion mass and $a^{-1}$ the lattice spacing. The 32Fine and 32Coarse data are new in this calculation.

This is a major update on the precision-study of the $K_{l3}$ form factor, $f_+(0)$ [Boyle 08b, Boyle 10]. Table 2.1 lists all the ensembles used and their properties. The ensembles are generated using RHMC algorithm and are sufficiently thermalised. The calculations are performed with the fifth dimension of length $L_s = 16$ or 32. The strange quark mass is chosen so that it is closer to the physical valence quark mass. For the ensemble with $am_{ud} = 0.005$, measurements are performed using two different valence strange quark masses ($am_s$).

The aim is to measure $f_0(q^2)$ on each of the ensemble and then perform mass extrapolation to obtain the form-factor at physical meson mass. Table 2.3 summarises the input quark masses ($am_{ud}, am_s$) , number of gauge configurations ($N_{meas}$), type of noise source and number of noise source positions ($N_{src}$) used for measurement for each ensemble. For each gauge configuration, the quark propagator is measured stochastically using "Z2PSWall" source with $N_{hits}$=1. In further discussion, the ensembles will be referred to by the set name listed in Table 2.3. For example, ensemble with $am_{ud} = 0.0042$ will be referred to as $B_4$.

The above measurements using DWF is expensive and is evident from table 2.2. This $K_{l3}$ calculation takes approximately 6000 years on a single core and is made possible only by the HPC resources listed in table 2.2.

| HPC | Location | Architecture | core-hours |
|---|---|---|---|
| JUGENE | Forschungszentrum Juelich | Blue Gene-P | 13.7 million |
| JUQUEEN | Forschungszentrum Juelich | Blue Gene-Q | 2.4 million |
| DiRAC | Univerity of Edinburgh | Blue Gene-Q | ≈35 million |
| DiRAC | Swansea Univerity | Blue Gene-P | ≈2 million |

Table 2.2: A summary of HPC resources used for this $K_{l3}$ calculation. Here core-hours is an approximate estimate of total time used in hours × number of cores used. Blue Gene-P and Blue Gene-Q have peak performance of 3.4 and 12.8 GFlops per core respectively.

| Label | set | $am_{ud}$ | $am_s^{sea}$ | $am_s^{val}$ | $N_{meas}$ | $N_{srcs}$ | $m_\pi L$ | $src$ |
|---|---|---|---|---|---|---|---|---|
| 24Coarse | $A_3$ | 0.03 | 0.04 | 0.04 | 105 | 2 | 9.13 | Z2PSWall |
| | $A_2$ | 0.02 | 0.04 | 0.04 | 85 | 2 | 7.7 | Z2PSWall |
| | $A_1$ | 0.01 | 0.04 | 0.04 | 153 | 2 | 5.8 | Z2PSWall |
| | $A_5^4$ | 0.005 | 0.04 | 0.04 | 143 | 8 | 4.6 | Z2PSWall |
| | $A_5^3$ | 0.005 | 0.04 | 0.03 | 143 | 8 | 4.6 | Z2PSWall |
| 32Fine | $C_8$ | 0.008 | 0.03 | 0.025 | 120 | 8 | 5.5 | Z2PSWall |
| | $C_6$ | 0.006 | 0.03 | 0.025 | 153 | 8 | 4.8 | Z2PSWall |
| | $C_4$ | 0.004 | 0.03 | 0.025 | 135 | 8 | 4.1 | Z2PSWall |
| 32Coarse | $B_4$ | 0.0042 | 0.045 | 0.045 | 162 | 16 | 5.7 | Z2PSWall |
| | $B_1$ | 0.001 | 0.045 | 0.045 | 196 | 16 | 3.9 | Z2PSWall |

Table 2.3: Simulation parameters: bare light quark mass ($am_{ud}$), strange quark mass ($am_s$), number of gauge configurations ($N_{meas}$), type of noise source and number of noise source positions ($N_{src}$) used.

## 2.4 Measurement techniques

Setting up the calculation for the new ensembles involve the following steps. Initially, for determining twists, the meson masses determined in [R.Arthur 12] were used.

1. Determine the meson masses at zero momentum for each ensemble.
2. Evaluate the twist required for pion or kaon to obtain $q^2 = 0$ (2.15).
3. Use twisted boundary conditions to measure 3-pt correlation functions.
4. Evaluate the ratios from the correlation functions as shown in (2.5) [Becirevic 05b] [Becirevic 05a]
5. From the ratios, obtain $f_+(q^2)$ and $f_-(q^2)$ as shown in (2.17).
6. Evaluate $f_0(q^2)$ from $f_+(q^2)$ and $f_-(q^2)$ as shown in (2.1)

In all the above analysis, statistical error for any measured quantity is determined by generating a bootstrap ensemble [Efron 79] of size 500. Data is usually binned before analysis and our analysis shows no real dependency on the bin size. In the final analysis, bin size is chosen to be same as the number of srcs ($N_{src}$) for each data set (as quoted in table 2.3).

## 2.5 Meson masses

The meson masses are calculated from the two-point correlation functions (2.2) using cosh fit. To avoid contamination from excited states, fit ranges for the cosh fit are determined to doing a constant fit for the effective mass using the following ansatz.

$$M_{eff} = \cosh^{-1}\left\{\frac{C_{t-1} + C_{t+1}}{2C_t}\right\} \tag{2.19}$$

From the $M_{eff}$ fits, the fit range for cosh fit is determined by looking for excited state contributions. Figures 2.1 - 2.10 shows the plot of $M_{eff}$ and the fit window used for data sets $A_3, A_2, A_1, A_5^3, A_5^4, C_8, C_6, C_4, B_4$ and $\mathrm{B}_1$. First two rows of Table 2.4 and 2.5 lists the exact fit window used for calculation of $M_{eff}$.

The meson masses determined are in good agreement with the values quoted in [R.Arthur 12] except for data set $C_4$. For $C_4$, [R.Arthur 12] mentions difficulty in

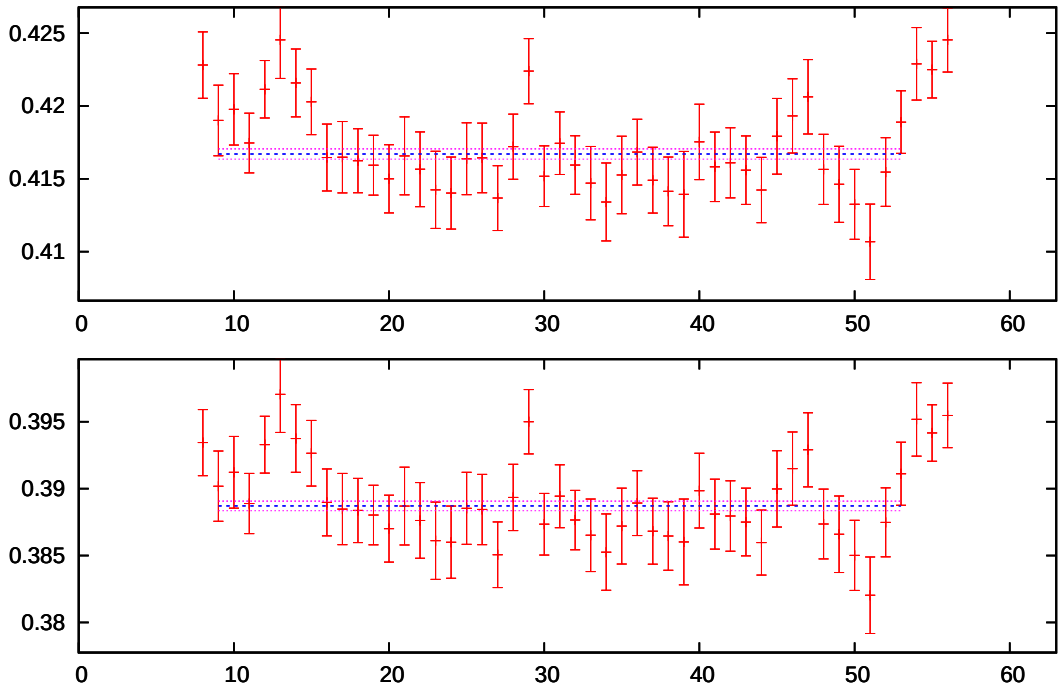


Figure 2.1: Plot of $am_K$ kaon(top) and $am_\pi$ pion(bottom) mass vs $t/a$ for $A_3$

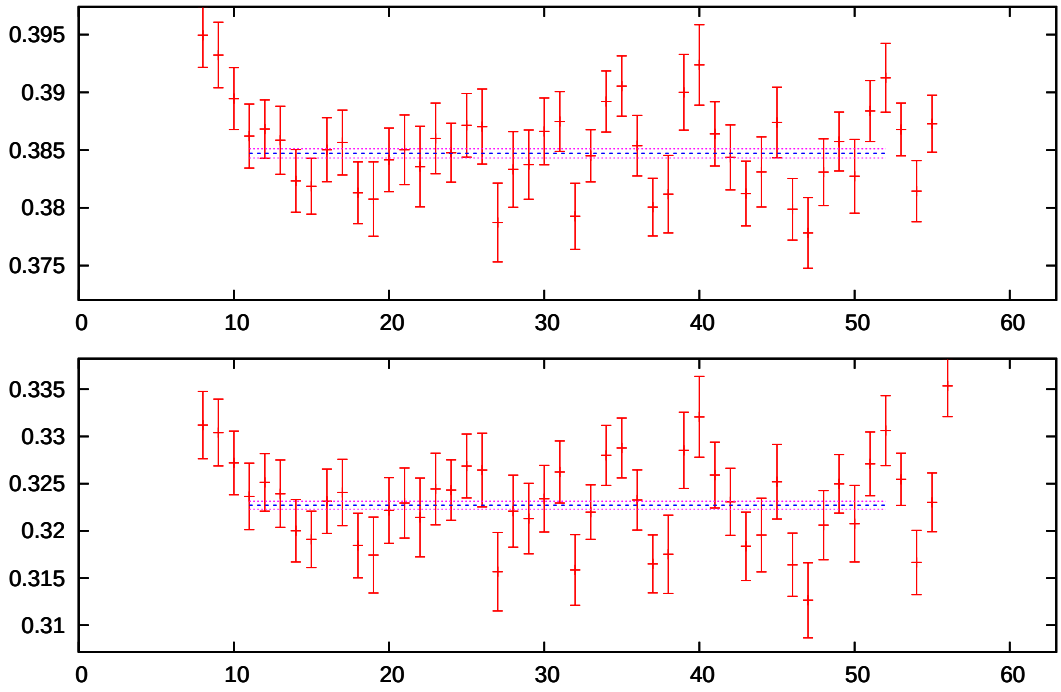


Figure 2.2: Plot of $am_K$ kaon(top) and $am_\pi$ pion(bottom) mass vs $t/a$ for $A_2$

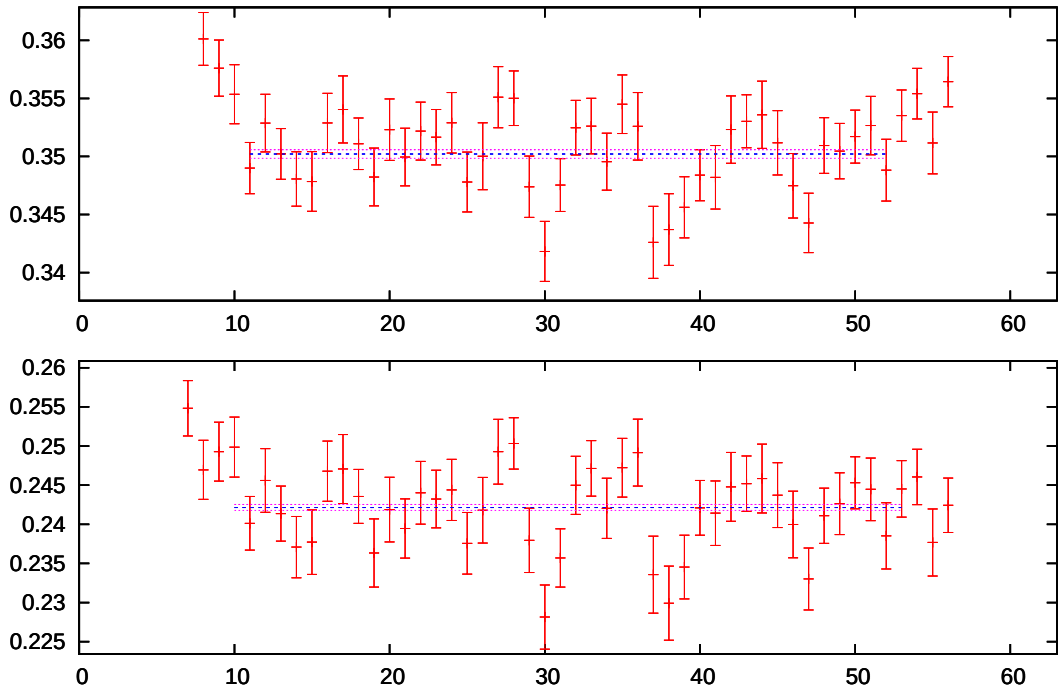


Figure 2.3: Plot of $am_K$ kaon(top) and $am_\pi$ pion(bottom) mass vs $t/a$ for $A_1$

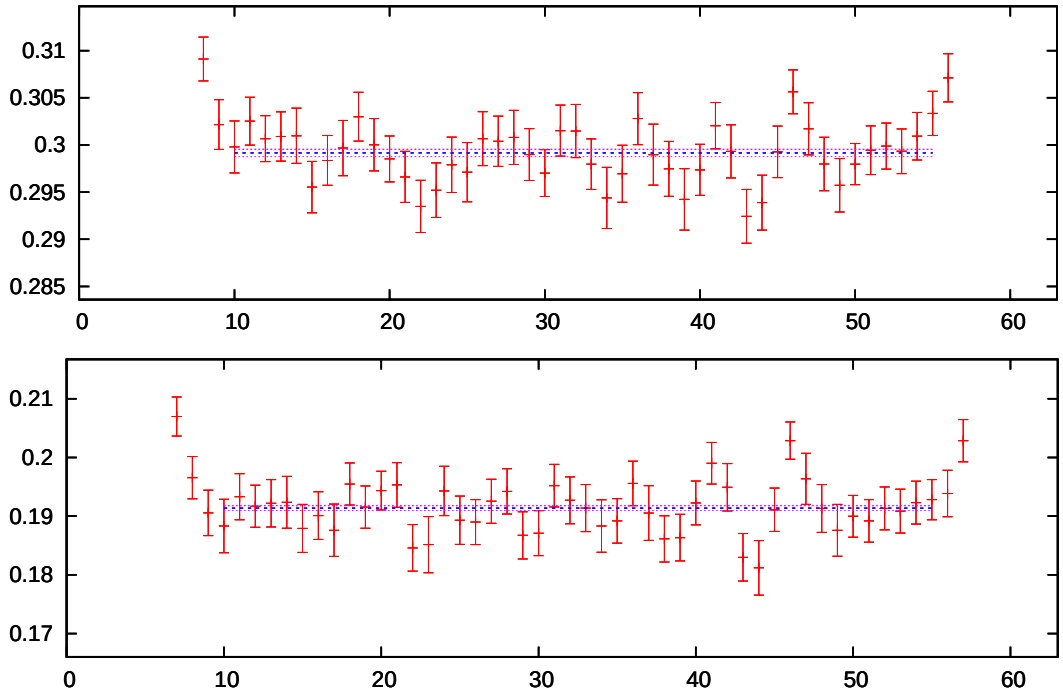


Figure 2.4: Plot of $am_K$ kaon(top) and $am_\pi$ pion(bottom) mass vs $t/a$ for $A_5^3$

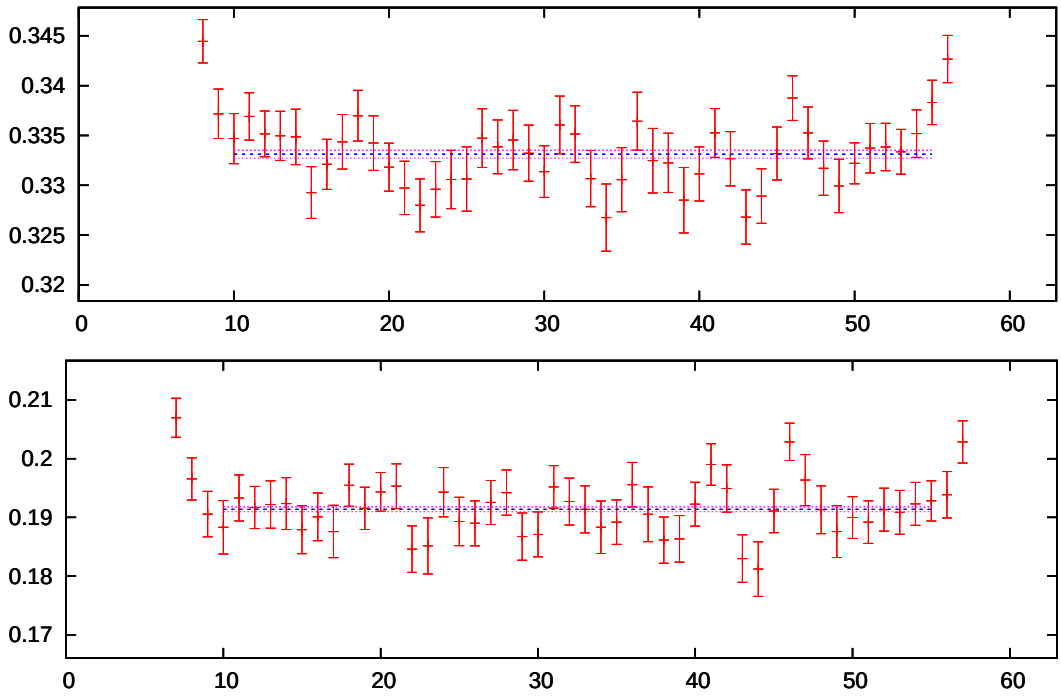


Figure 2.5: Plot of $am_K$ kaon(top) and $am_\pi$ pion(bottom) mass vs $t/a$ for $A_5^4$

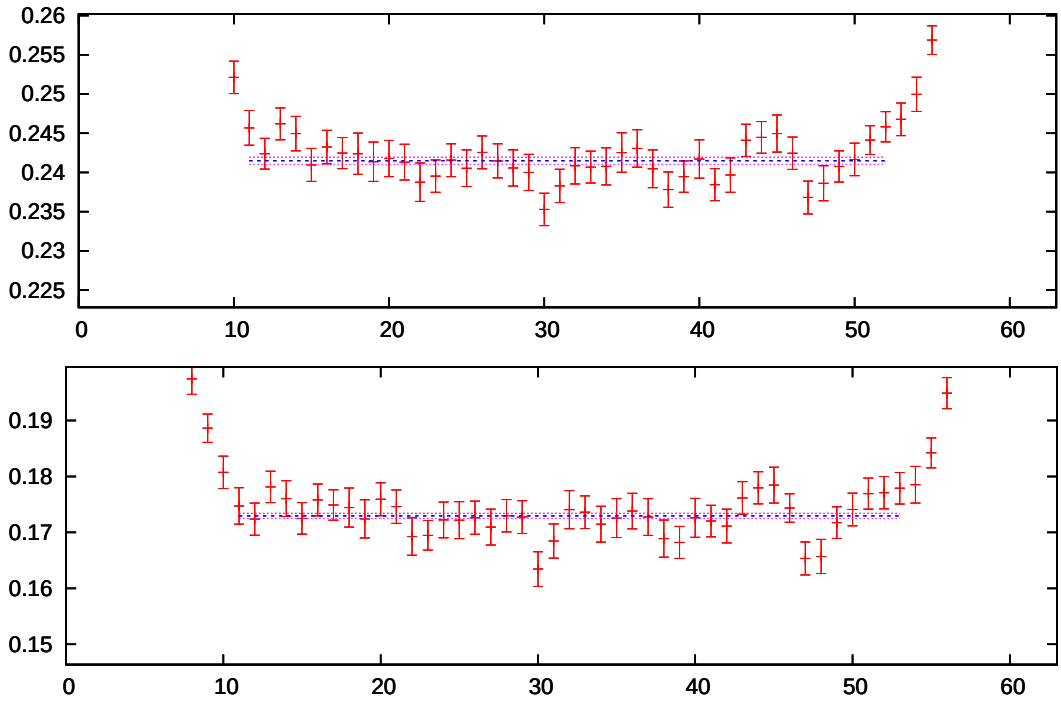


Figure 2.6: Plot of $am_K$ Kaon(top) and $am_\pi$ pion(bottom) mass vs $t/a$ for $C_8$

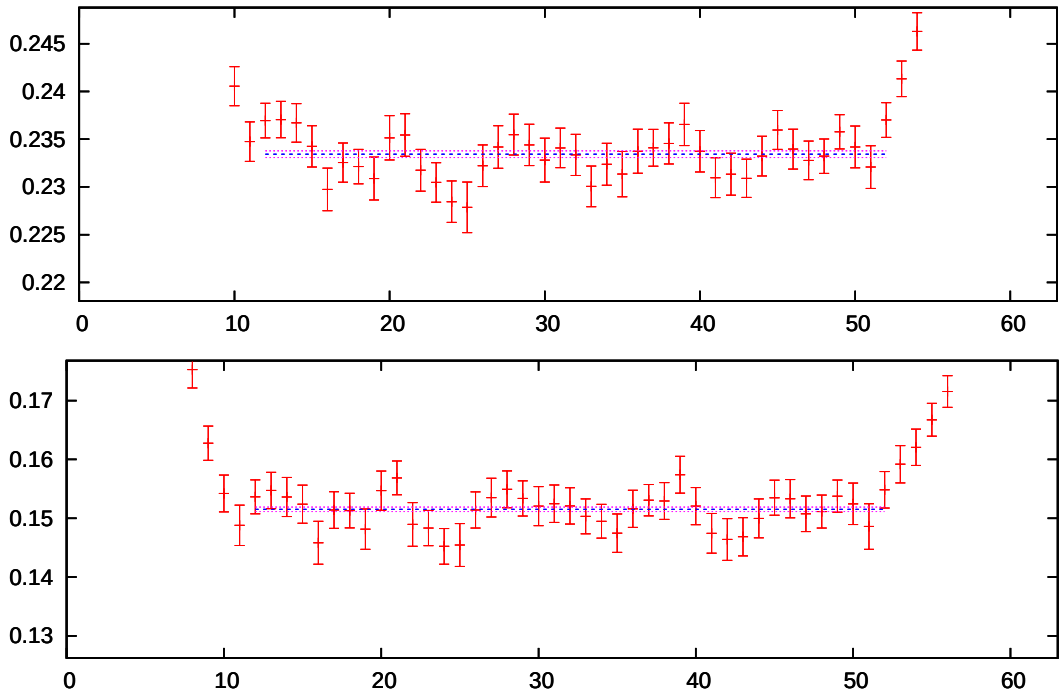


Figure 2.7: Plot of $am_K$ kaon(top) and $am_\pi$ pion(bottom) mass vs $t/a$ for $C_6$

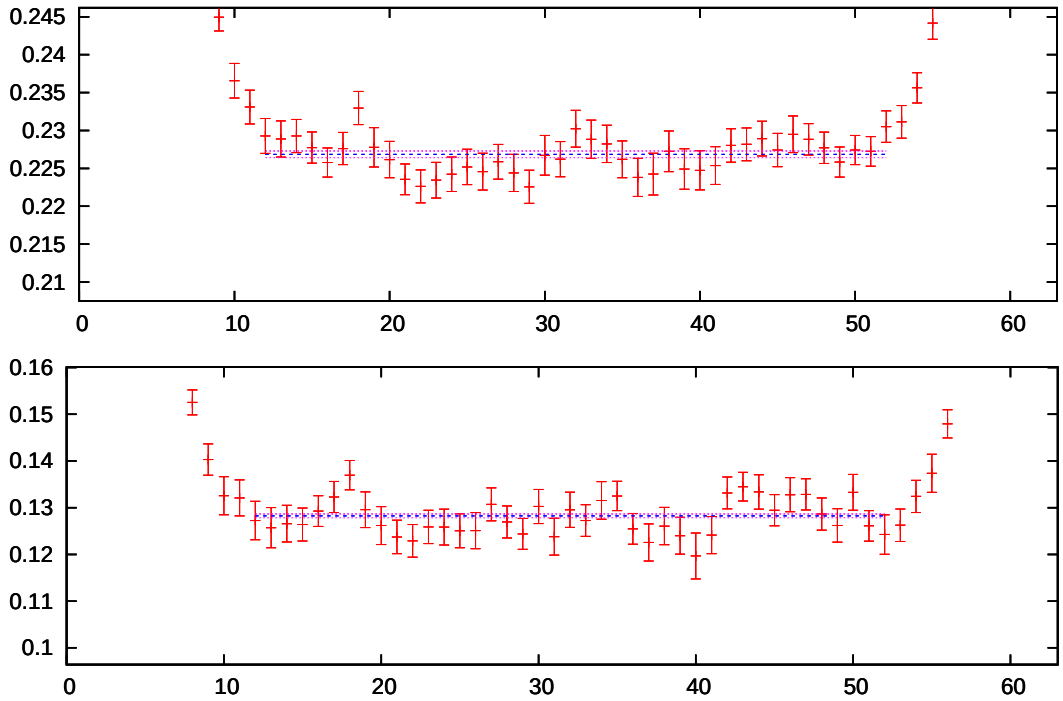


Figure 2.8: Plot of $am_K$ kaon(top) and $am_\pi$ pion(bottom) mass vs $t/a$ for $C_4$

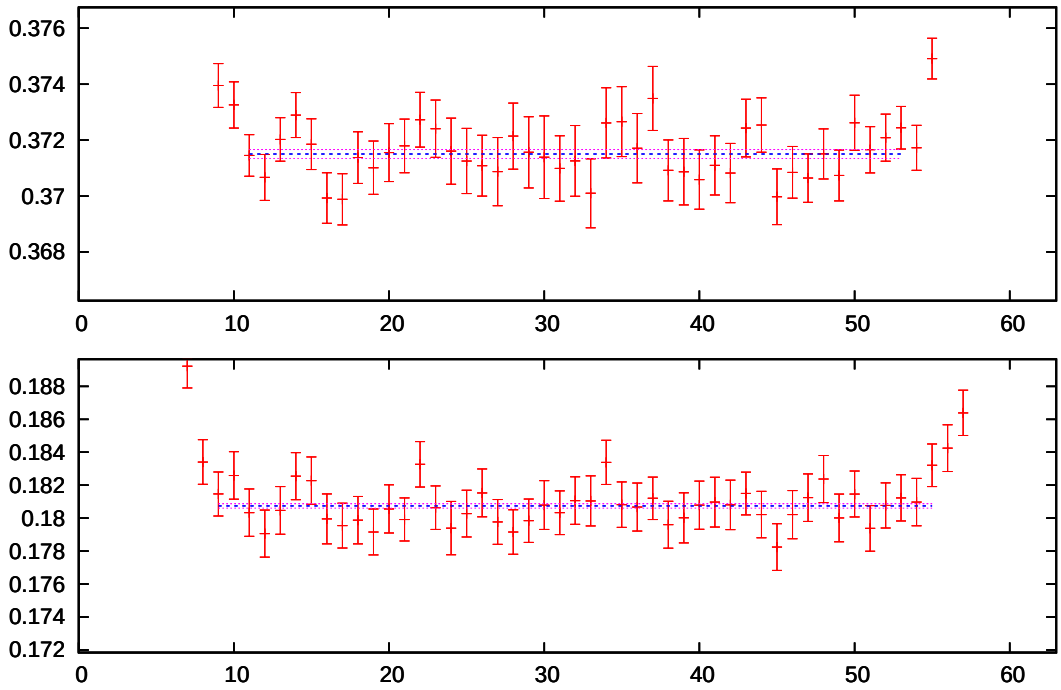


Figure 2.9: Plot of $am_K$ kaon(top) and $am_\pi$ pion(bottom) mass vs $t/a$ for $B_4$

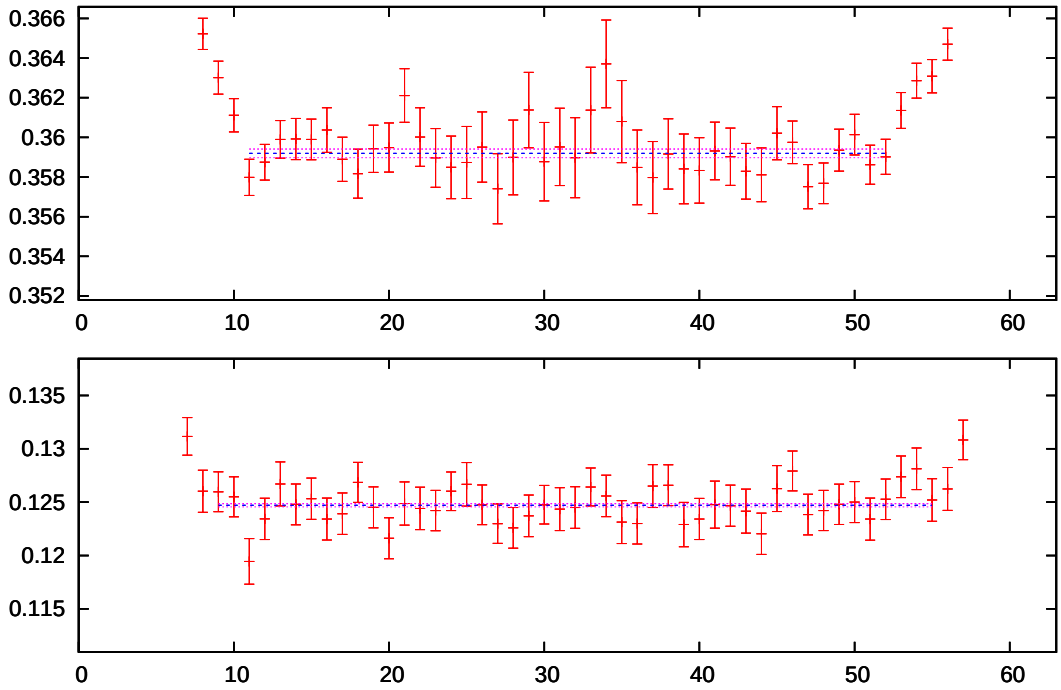


Figure 2.10: Plot of $am_K$ kaon(top) and $am_\pi$ pion(bottom) mass vs $t/a$ for $B_1$

| set | $A_3$ | $A_2$ | $A_1$ | $A_5^4$ | $A_5^3$ | $C_8$ | $C_6$ | $C_4$ |
|---|---|---|---|---|---|---|---|---|
| $am_\pi$ | 12-52 | 11-53 | 10-54 | 10-54 | 10-54 | 8-56 | 12-52 | 12-52 |
| $am_K$ | 12-52 | 11-53 | 11-53 | 10-54 | 10-54 | 9-55 | 12-52 | 12-52 |
| $R_\pi^x$ | 4-22 | 4-19 | 6-20 | 8-20 | 8-20 | 6-13 | 9-14 | na. |
| $R_\pi^y$ | 8-20 | 6-21 | 3-21 | na. | na. | 6-15 | 11-17 | 7-14 |
| $R_\pi^z$ | 6-17 | 6-18 | 4-21 | na. | na. | na. | na. | 10-13 |
| $R_\pi^t$ | 5-22 | 4-22 | 4-22 | 8-18 | 9-17 | 5-19 | 5-19 | 5-19 |
| $R_K^x$ | 4-22 | 4-20 | 4-22 | 4-18 | 4-18 | na. | na. | 7-19 |
| $R_K^y$ | 8-20 | 6-21 | 4-22 | na. | na. | 9-20 | 5-17 | 5-18 |
| $R_K^z$ | 6-17 | 6-18 | 4-22 | na. | na. | 8-19 | 5-13 | na. |
| $R_K^t$ | 5-22 | 4-22 | 4-22 | 14-23 | 14-23 | 5-19 | 5-19 | 8-19 |
| $R_{K\pi}^x$ | 6-20 | 6-20 | 6-20 | 6-20 | 6-20 | 6-16 | 8-15 | 5-20 |
| $R_{K\pi}^y$ | 6-20 | 6-20 | 6-20 | na. | na. | 6-17 | 10-16 | 8-14 |
| $R_{K\pi}^z$ | 6-20 | 6-20 | 6-20 | na. | na. | 8-19 | 11-17 | 13-19 |
| $R_{K\pi}^t$ | 6-20 | 6-20 | 6-20 | 6-20 | 6-20 | 5-19 | 5-19 | 11-21 |
| $R_2$ | 6-20 | 6-20 | 4-22 | 6-20 | 6-20 | 6-18 | 5-18 | 6-17 |
| $Z_V$ | 7-19 | 4-20 | 4-20 | 4-21 | 4-20 | 5-19 | 5-19 | 5-19 |

Table 2.4: Fit window used for 24Coarse and 32Fine ensembles. na. indicates that a fit window cannot be identified as the parameter could not be fitted to a constant value. $R$ refers to ratio in (2.5) and its subscript refers to the meson that is twisted; superscript refers to the twist direction. $R_2$ and $Z_V$ are defined in (2.7) and (2.4) respectively.

| Kinematics | PT, KT | | PKT | |
|---|---|---|---|---|
| set | $B_4$ | $B_1$ | $B_4$ | $B_1$ |
| $am_\pi$ | 9-55 | 9-55 | 10-54 | 12-52 |
| $am_K$ | 11-53 | 10-54 | 11-53 | 12-52 |
| $R_\pi^x$ | 8-15 | 6-17 | 8-17 | na. |
| $R_\pi^y$ | na. | 7-16 | na. | na. |
| $R_\pi^z$ | 7-17 | na. | na. | 7-14 |
| $R_\pi^t$ | 7-20 | 7-19 | 7-19 | 11-17 |
| $R_K^x$ | 5-20 | na. | na. | 13-17 |
| $R_K^y$ | 5-20 | na. | 7-21 | 9-19 |
| $R_K^z$ | na. | na. | 4-18 | na. |
| $R_K^t$ | 5-20 | na. | 6-15 | 8-18 |
| $R_{K\pi}^x$ | 9-15 | na. | 5-16 | 10-18 |
| $R_{K\pi}^y$ | 5-20 | na. | 4-21 | 13-18 |
| $R_{K\pi}^z$ | 7-15 | na. | 8-18 | 7-18 |
| $R_{K\pi}^t$ | 7-20 | na. | 10-20 | 9-20 |
| $R_2$ | 10-16 | 7-16 | 8-16 | 6-17 |
| $Z_V$ | 6-17 | 5-19 | 10-18 | 5-19 |

Table 2.5: Fit window used for 32Coarse ensembles as in table 2.4 for Kinematics PT, KT and PKT (refer table 2.7).

| *set* | $am_\pi$ | $am_K$ | $q^2_{\max}$ [GeV$^2$] | $f_0(q^2_{max})$ |
|---|---|---|---|---|
| $A_3$ | 0.38815(36) | 0.41613(35) | 0.0024(1) | 1.0003(1) |
| $A_2$ | 0.32219(45) | 0.38428(45) | 0.0118(4) | 1.0018(1) |
| $A_1$ | 0.24163(37) | 0.35015(40) | 0.0359(12) | 1.0080(3) |
| $A_5^4$ | 0.19090(46) | 0.29849(48) | 0.0610(22) | 1.0181(12) |
| $A_5^3$ | 0.19090(46) | 0.33234(53) | 0.0353(13) | 1.0120(8) |
| $C_8$ | 0.17256(39) | 0.24124(40) | 0.0251(8) | 1.0066(4) |
| $C_6$ | 0.15109(36) | 0.23283(34) | 0.0357(12) | 1.0089(6) |
| $C_4$ | 0.12745(46) | 0.22619(47) | 0.0520(17) | 1.0193(11) |
| $B_4$ | 0.18059(13) | 0.37143(19) | 0.0682(9) | 1.0305(7) |
| $B_1$ | 0.12461(15) | 0.35942(28) | 0.1033(13) | 1.0607(10) |

Table 2.6: $am_\pi$, $am_K$ (2.19) and $q^2_{max} = (m_K - m_\pi)^2$, $f_0(q^2_{max})$ (2.7) for each data set.

fitting masses associated with difference between different interpolating operators. Such discrepancies are not seen in the new measurements which uses Z2PSWall noise sources and this measured value is used for further analysis. In all further discussion and analysis, the meson mass determined by this study will be used unless specified otherwise.

Table 2.6 lists the meson mass obtained and $q^2_{max}$ for each of the data set. Here, $q^2_{\max}$ is found to increase gradually from 0.0024(1) to 0.1033(13) as $m_\pi$ is reduced from 678 MeV to 170 MeV. This in turn will demand a increase in twists in order to achieve $q^2$=0.

## 2.6 Twisted boundary conditions

For 24Coarse ensembles, Fourier modes were used to obtain form-factor at different $q^2$ and then interpolated to $q^2 = 0$. In this work, partial twisted boundary condition is used to evaluate form-factor at $q^2 = 0$. In addition to measuring 32Fine and 32Coarse ensembles, 24Coarse ensembles are re-measured using twisted boundary conditions to completely eliminate error due to $q^2$ interpolation. As noted in table 2.6, $q^2_{max}$ increases approximately by 43 times as $m_\pi$ reduces by a factor of 4 (678→170). From (2.15), this directly implies that the twists applied to absorb $q^2$ should increase. Naively one would apply twists in only one direction ($x$ or $y$ or $z$) as shown in (2.15). Tests showed that the signal becomes noisy as the twist angle is increased. We found that applying twists in

two or all directions reduces twist angle in single direction and empirically the noise is reduced.

The simultaneous equations in (2.17) give us different choices in solving them, based on the application of twists and twist angles. To simplify the discussion, these different choices are grouped as "Kinematic" as listed below.

1. **Kinematic-PT** : Solve equations for the choice where "only Pion" is twisted

$$K(m_K, \vec{0}) \rightarrow \pi(m_\pi, \vec{\theta_\pi}); \quad q^2 = [m_K - E_\pi]^2 - [\frac{\vec{\theta_\pi}}{L}]^2 = 0 \tag{2.20}$$

2. **Kinematic-KT** : Solve equations for the choice where "only Kaon" is twisted

$$K(m_K, \vec{\theta_K}) \rightarrow \pi(m_\pi, \vec{0_\pi}); \quad q^2 = [E_K - m_\pi]^2 - [\frac{\vec{\theta_K}}{L}]^2 = 0 \tag{2.21}$$

3. **Kinematic-PKT** : Solve equations for the choice where "Pion and Kaon" are twisted

$$K(m_K, \vec{\theta_K}) \rightarrow \pi(m_\pi, \vec{\theta_\pi}); \quad q^2 = [E_K - E_\pi]^2 - [\frac{\vec{\theta_K} - \vec{\theta_\pi}}{L}]^2 = 0 \tag{2.22}$$

4. **Kinematic-BT** : Solve together equations for the choice where "only Pion" and "only Kaon" are twisted

$$\mathrm{BT} = \mathrm{PT} + \mathrm{KT}; \quad \mathrm{q}^2 = 0 \tag{2.23}$$

5. **Kinematic-ALLT**: Solve all equations for different choices where "only Pion", "only Kaon" and "Pion and Kaon" are twisted

$$\mathrm{ALLT} = \mathrm{PT} + \mathrm{KT} + \mathrm{PKT}; \quad \mathrm{q}^2 = 0 \tag{2.24}$$

Equation (2.15) can be used to compute twists only when pion or kaon is twisted. Additionally we can evaluate $f_0(q^2)$ at a nonzero $q^2$ when the above twists are used together. This can be used along with the $f_0(q^2_{max})$ to better constrain the fit for $q^2$ interpolation. $f_0(0)$ can be evaluated independently using any one of

| set | PT : $\theta_\pi$ | KT : $\theta_\mathrm{K}$ | PKT : $\theta_\pi, \theta_\mathrm{K}$ |
|---|---|---|---|
| $A_3$ | (0.375, 0.375, 0.375) | (0.402, 0.402, 0.402) | na. |
| $A_2$ | (0.790, 0.790, 0.790) | (0.943, 0.943, 0.943) | na. |
| $A_1$ | (1.270, 1.270, 1.270) | (1.842, 1.842, 1.842 | na. |
| $A_5^4$ | (2.682, 0.000, 0.000) | (4.681, 0.000, 0.000) | na. |
| $A_5^3$ | (2.129, 0.000, 0.000) | (3.337, 0.000, 0.000) | na. |
| $C_8$ | (0.943, 1.622, 0.000) | (0.000, 1.570, 2.094) | na. |
| $C_6$ | (0.943, 1.934, 0.000) | (0.000, 1.570, 2.915) | na. |
| $C_4$ | (1.739, 1.739, 0.000) | (0.000, 3.086, 3.086) | na. |
| $B_4$ | (3.209, 0.000, 3.209) | (0.000, 6.587, 6.587) | $(3.689, 0.000, 0.000)$, $(0.000, 2.356, 3.927)$ |
| $B_1$ | (2.513, 4.382, 0.000) | (0.000, 0.000, 0.000) | $(0.000, 0.000, 4.173)$, $(4.712, 3.142, 0.000)$ |

Table 2.7: Choice of twist angles used for Kinematic-PT, KT and PKT for each of the ensembles. na. refers that the particular Kinematic is not used to measure $f_0(q^2 \approx 0)$.

the Kinematic and we can expect the values to be in good agreement.

Table 2.7 lists the twist angles applied to each of the data sets for Kinematic-PT, KT and PKT. For $B_1$, only Kinematic-PT can be used, as measurements performed with Kinematic-KT are noisy. Assuming twists are applied in only one direction, $B_1$ requires twist of $\theta_\pi = 5.049$ (PT) or $\theta_K = 14.51$ (KT) to get $q^2 = 0$. The resulting ratio $R_1$ for kinematic-PT and KT are shown in Fig. 2.11.

These ratios corresponding to KT are noisy with error >50%. These ratios cannot be used in solving simultaneous equations for $f_+(0)$. This noise is due to bigger twist applied to kaon that is three times that for pion. The applied twists can be reduced by twisting in all spatial directions but test showed that the channel is still noisy. It is important to note that in all the above cases, the aim is to get zero momentum transfer, and we can use any of the kinematic to get $q^2 = (p_i - p_f)^2 = 0$.

### 2.6.1 Kinematic-PKT

It is possible to determine the form factor at $q^2 = 0$ without the correlators where the kaon carries the twist (Kinematic-KT). For the case where only the pion is twisted (Kinematic-PT), using the the system of linear equations in (2.17) will determine the form factor. The problem with using only the results from PT is that we have two equations (2.17) with two unknowns and so they aren't very

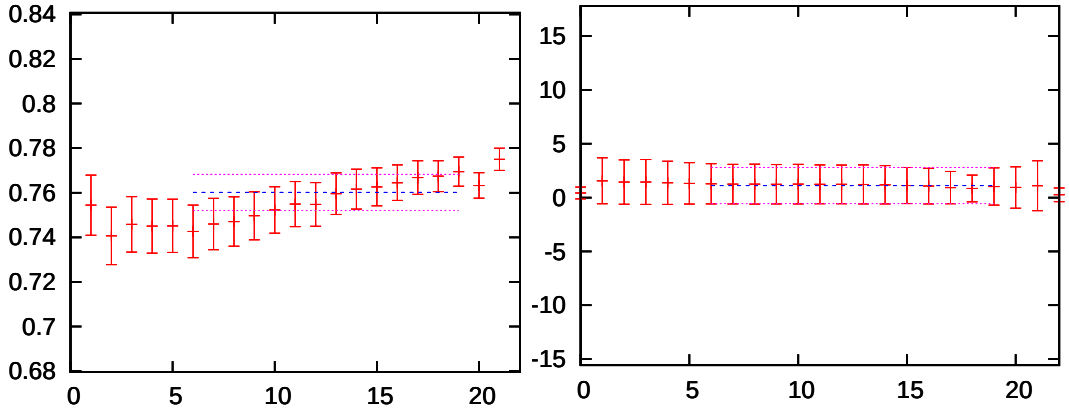


Figure 2.11: Plot of $R_1$ (2.5) vs $t/a$ : left : when twist $\theta_{pi} = 5.049$ (PT) is applied, right: when twist $\theta_K = 14.51$ (KT) is applied, to obtain $q^2 = 0$. In the above plots, Y axis has different range and the difference shows the noise in Kinematic-KT

well constrained. By twisting pion and kaon (Kinematic-PKT), we will have more equations that will better constrain $f+(0)$.

For the data set $B_1$, to reduce the kaon twist angles and still obtain $q^2 = (p_i - p_f)^2 = 0$, the approach to twist only kaon cannot be used as shown in the previous section 2.6. If the pion and kaon are twisted(Kinematic-PKT) to obtain $q^2 = 0$, the twists for kaon and pion are considerably reduced. For example when the following twists (0.0,0.0,4.173) and (4.714,3.142,0.0) are used for pion and kaon respectively, the ratios have good statistical signal compared to ratios shown in Fig. 2.11. Fig. 2.12 shows $R_1$ ratio for Kinematic-PKT using the above mentioned twist angles.

So in order to check if we get a better constraint on the relationship, measurements are performed on $B_1$ configurations with Kinematic-PKT and Kinematic PT. This is found to be a better approach as the form-factor value determined from Kinematic-PKT is found to be in good agreement with that for Kinematic-PT.

## 2.7 Ratios

The ratios $(R_1, R_2, R_3)$ in (2.5), are evaluated using the correlation functions and meson masses. They should be evaluated and then fitted to a constant

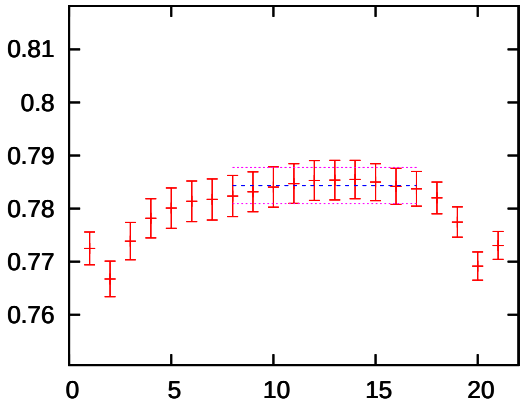


Figure 2.12: Plot of $R_1$ (2.5) vs $t/a$ when kaon and pion are twisted (PKT) to obtain $q^2 = 0$

value by choosing a suitable fit widow. R3 ratio is found to be noisy and is ignored in all our analysis. Using multiple ratios does not necessarily improve the error because they are highly correlated. However they can be compared for correctness. For each kinematic, $R_1$ and $R_2$ ratio are evaluated from both temporal and spatial components of vector current and then we can solve for $f_+(q^2)$ and $f_-(q^2)$ simultaneously (2.17).

Figures 2.13, 2.14 and 2.15 shows ratios $R_1$(left) and $R_2$(right) for data sets $B_4$ (PT), $C_8$ (KT) and $B_1$ (PKT) respectively. These ratios have good signal and are fitted to a constant value by selecting a suitable fit window to avoid any excited state contributions. Table 2.4 and 2.5 lists the fit window used for the ratios in spatial and temporal direction. Similarly for data sets $A_5^3$ and $A_5^4$, Fig. 2.16 and Fig. 2.17 shows R1 ratios for PT and KT kinematic.

$R_1$ ratio contains local vector current and is not balanced between numerator and denominator whereas R2 is balanced. This is therefore not self normalising and renormalisation of the local vector current must be included. Thus we expect,

$$R_2 = R_1 \times Z_V \tag{2.25}$$

Fig. 2.18 shows plot of $Z_V$ determined for $C_6$ and $A_3$ data set and fitted to a constant value. Fig. 2.19 shows plot of $R_2$ ratio computed for set $C_6$ and $A_2$ fitted to a constant value. $f_0(q^2_{max})$ is evaluated precisely from this ratio as defined in (2.7).

As shown in the plots, we have very good plateau that can be fitted to a

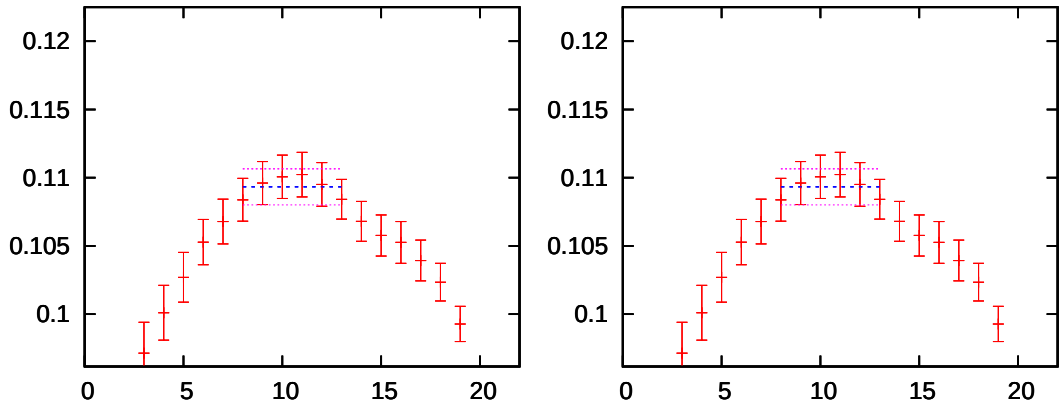


(a) ratios from $V_x$, twist in x direction only

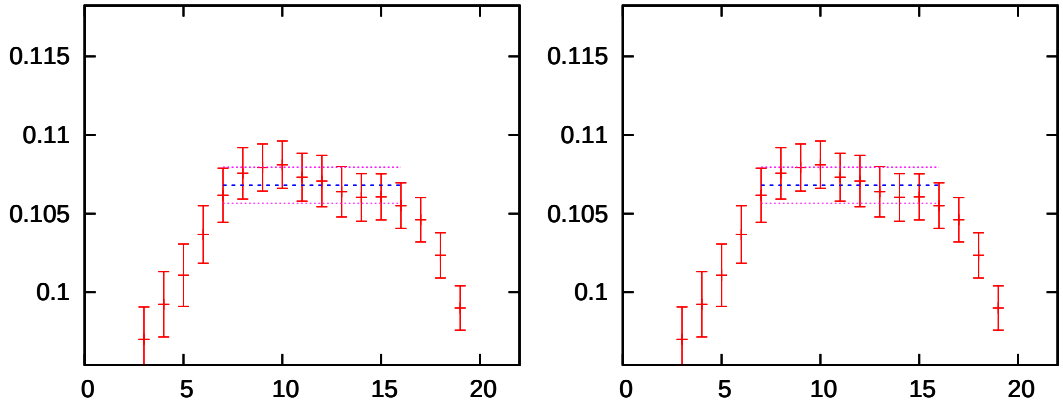


(b) ratios from $V_z$, twist in z direction only

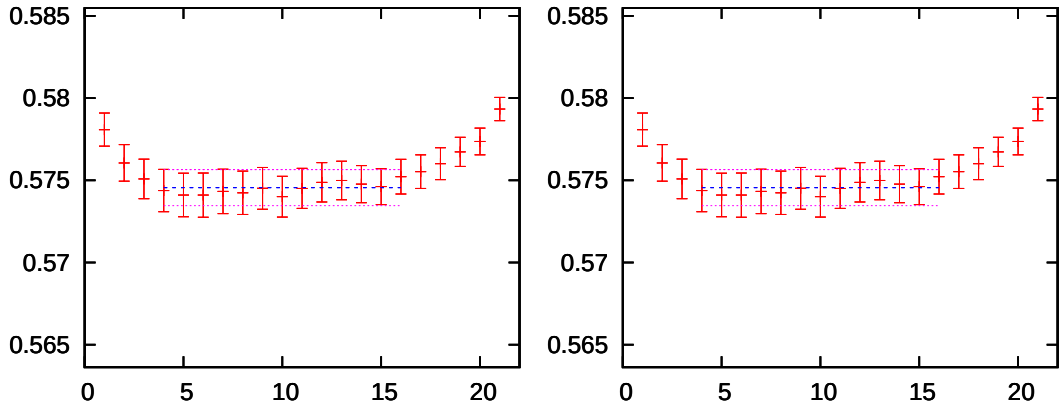


(c) ratios from $V_t$, twist in t direction only

Figure 2.13: Plot of ratios (2.5), $R_1$(left) and $R_2$(right) vs $t/a$ for $B_4$ ensemble when pion is twisted (Kinematic-PT)

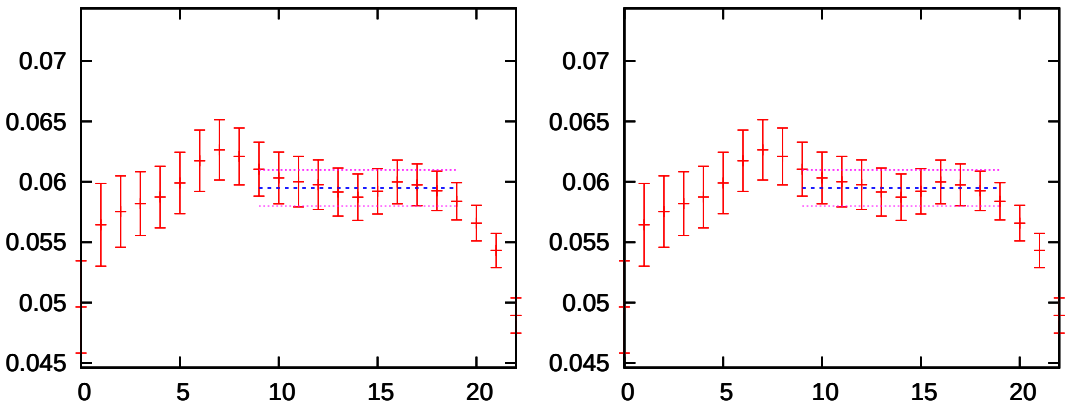


(a) ratios from $V_y$, twist in y direction only

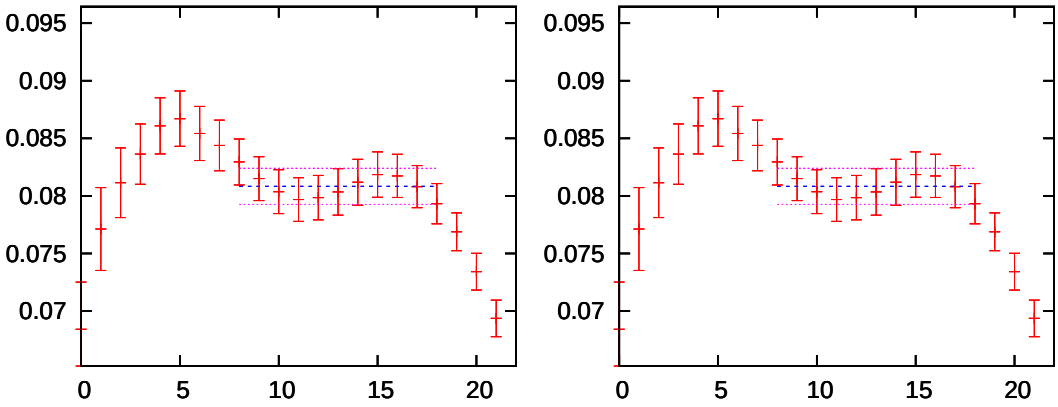


(b) ratios from $V_z$, twist in z direction only

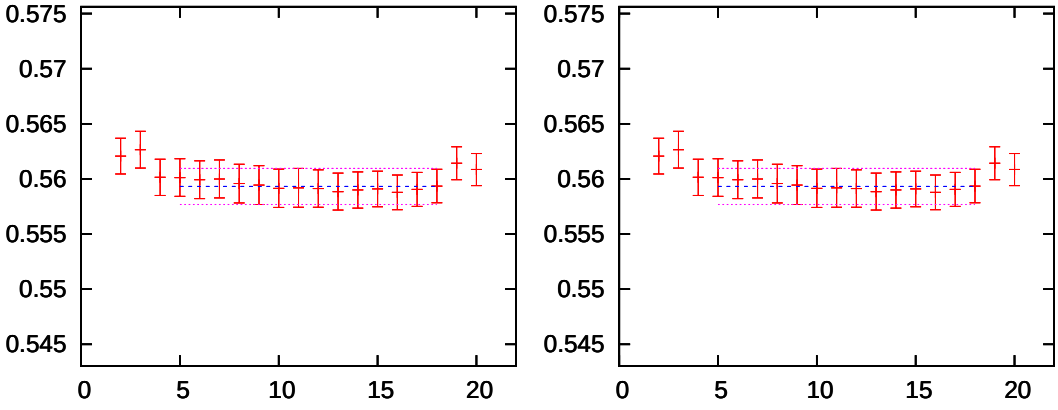


(c) ratios from $V_t$, twist in t direction only

Figure 2.14: Plot of ratios (2.5), $R_1$(left) and $R_2$(right) vs $t/a$ for $C_8$ ensemble when only kaon is twisted (Kinematic-KT)

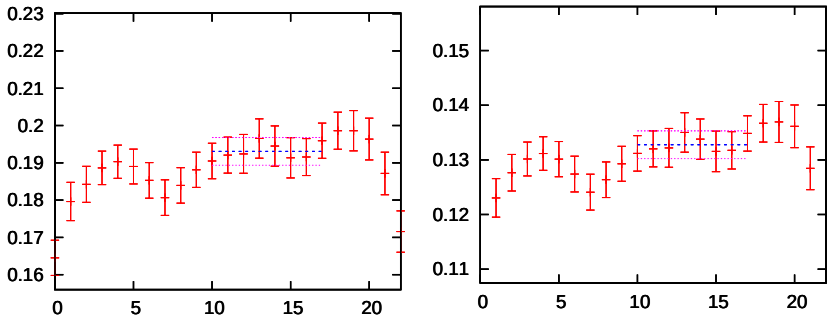


(a) ratios from $V_x$, twist in x direction only

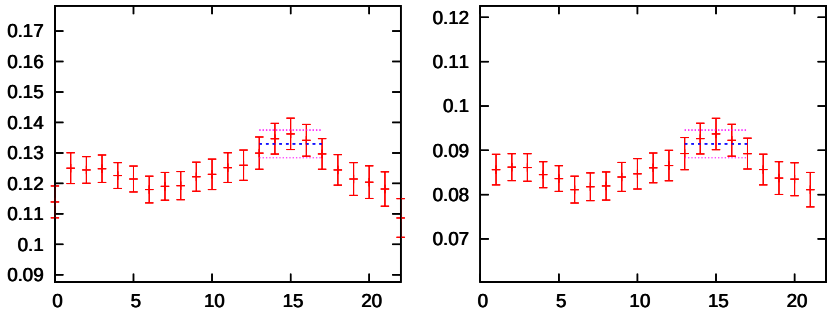


(b) ratios from $V_y$, twist in y direction only

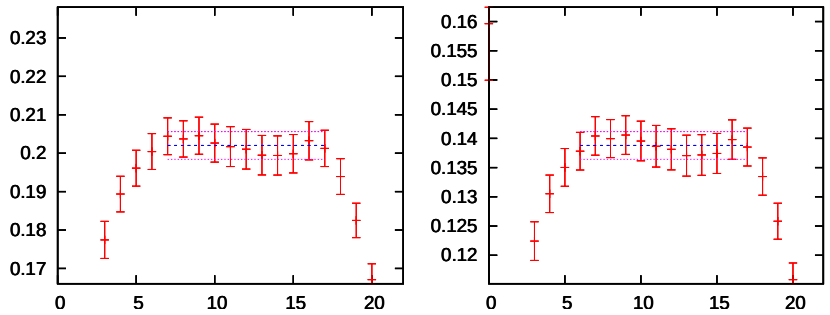


(c) ratios from $V_z$, twist in z direction only

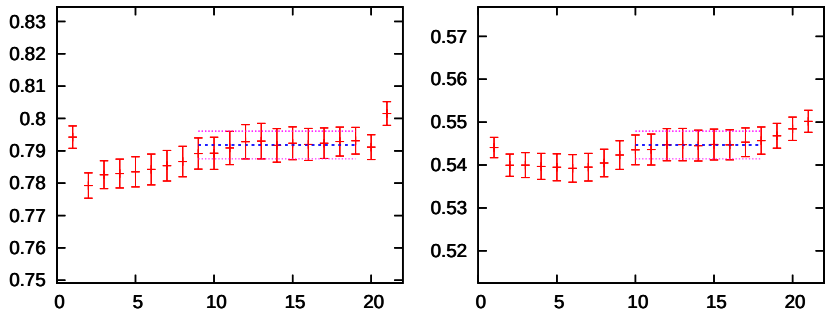


(d) ratios from $V_t$, twist in (x,y,z) directions

Figure 2.15: Plot of ratios (2.5), $R_1$(left) and $R_2$(right) vs $t/a$ for $B_1$ ensemble when both pion and kaon are twisted

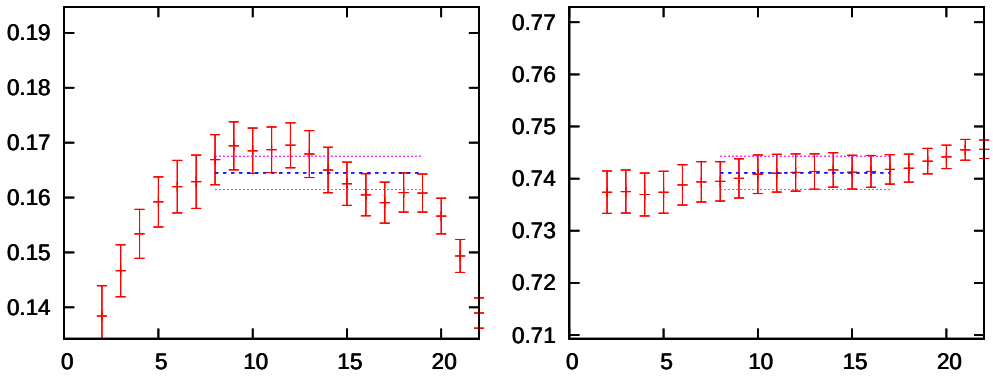


Figure 2.16: Plot of ratio (2.5), $R_1$ vs $t/a$ from $V_x$ (left) and $V_t$ (right) for $A_5^4$ ensemble when only pion is twisted (Kinematic-PT)

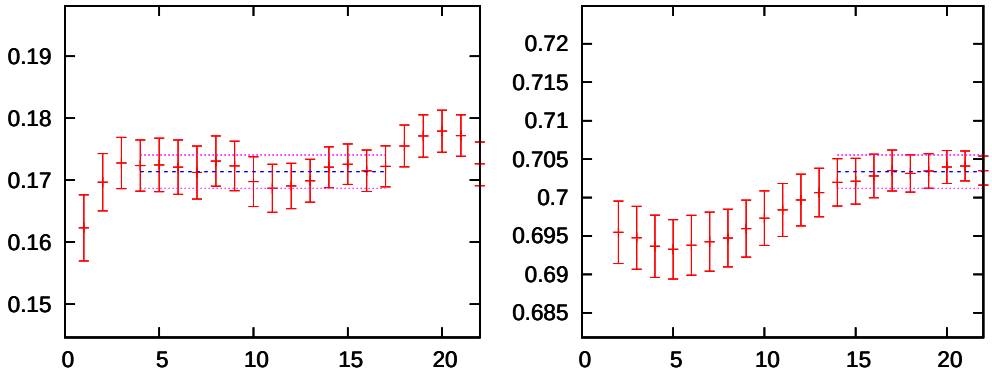


Figure 2.17: Plot of $R_1$ (2.5) vs $t/a$ from $V_x$ (left) and $V_t$ (right) for $A_5^3$ ensemble when only kaon is twisted (Kinematic-KT)

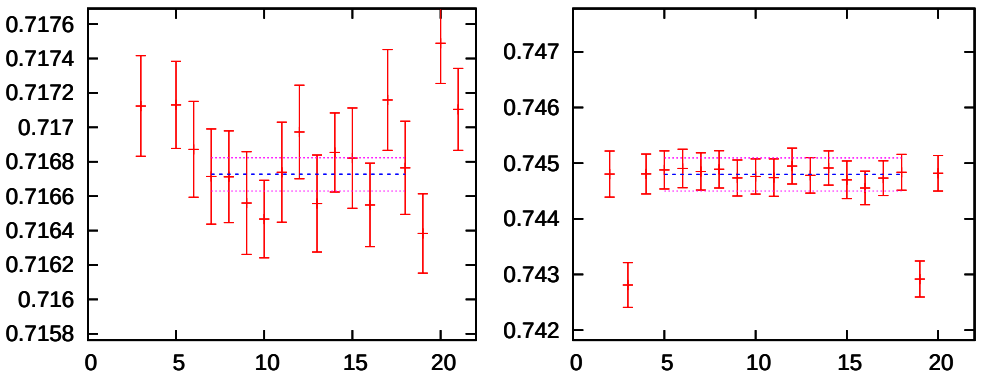


Figure 2.18: Plot of $Z_V$ (2.4) vs $t/a$ for $A_3$(left) and $B_6$(right)

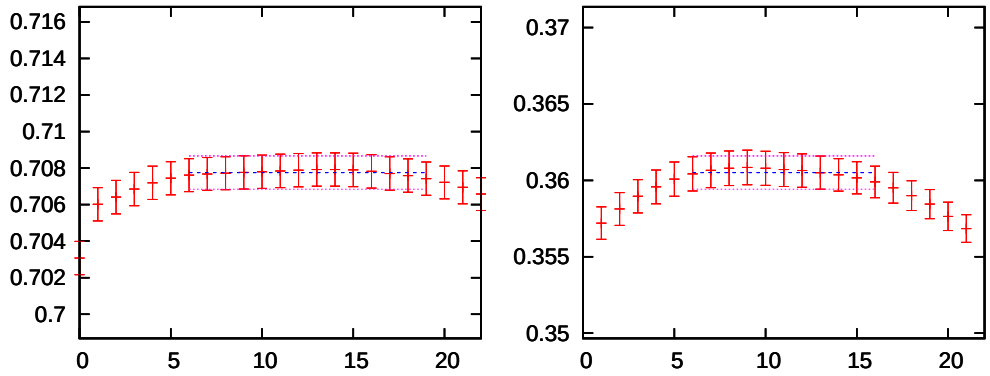


Figure 2.19: Plot of $R_2$ (2.7) vs $t/a$ for $A_2$(left) and $B_4$(right)

constant value. Some ratios have shorter plateau and the fit range is chosen conservatively as shown in figures 2.13b and 2.14b. We note that where significant ripples that say break time reversal occur, the fit range philosophy has been that these are statistical effects that we are better to average over. This avoids selecting a short sequence of correlated data points that could underestimate the error.

## 2.8 Solving Kinematic

From the ratios, the form-factor $f_0^{K\pi}(q^2)$ is determined at different $q^2$ by forming simultaneous equations (2.17) for each of the kinematics and then solving them simultaneously. For example in case of Kinematic-PT, if pion is twisted only in one direction, then we have two simultaneous equations for the spatial and time component. If we consider $R_1$ and $R_2$ ratios, then we have four equations to solve. These four equations are solved to obtain form-factor for the Kinematic-PT and similarly for Kinematic-KT. Table 2.8 lists the form factors for each set for Kinematic PT and KT. Fig. 2.20 shows the the dependence of these form factor on $m_\pi$.

As seen in Fig. 2.20, the form-factor of data sets with $m_\pi < 400$ seem to be inconsistent. The form-factor determined from Kinematic PT and KT differ by more than one sigma. In particular, for data sets $B_4$ and $C_4$, there is a 2% discrepancy which is ten times that of statistical error. This is the primary reason for exploring other kinematic choices to reduce this discrepancy.

| set | Kin. | $(aq)^2$ | $f_+(q^2)$ | $f_-(q^2)$ | $f_0(q^2)$ | $\chi^2/dof$ |
|---|---|---|---|---|---|---|
| $A_3$ | PT | -1.86e-06(195) | 0.99994(117) | -0.0493(348) | 0.99994(117) | 1.74 |
| $A_3$ | KT | -1.95-06(210) | 0.99830(125) | -0.0051(349) | 0.99830(126) | 1.50 |
| $A_2$ | PT | 4.97e-06(111) | 0.99565(154) | -0.0561(187) | 0.99565(154) | 0.16 |
| $A_2$ | KT | 3.66e-06(132) | 0.99557(173) | -0.0578(185) | 0.99557(173) | 0.04 |
| $A_1$ | PT | 1.40e-05(329 | 0.98533(176) | -0.0590(176) | 0.98532(176) | 0.90 |
| $A_1$ | KT | -9.07e-06(453) | 0.98893(190) | -0.1064(96) | 0.98894(192) | 1.20 |
| $A_5^4$ | PT | -0.00015(7) | 0.97384(494) | -0.0792(159) | 0.97400(495) | na. |
| $A_5^4$ | KT | -0.00024(11) | 0.98964(935) | -0.1439(221) | 0.99011(945) | na. |
| $A_5^3$ | PT | -0.00013(4) | 0.98228(370) | -0.0510(161) | 0.98240(372) | na. |
| $A_5^3$ | KT | -0.00019(7) | 0.99769(538) | -0.1167(183) | 0.99810(546) | na. |
| $C_8$ | PT | 3.96e-05(189) | 0.98853(333) | -0.0533(204) | 0.98845(331) | 0.14 |
| $C_8$ | KT | 5.45e-05(261) | 0.99158(358) | -0.0770(177) | 0.99143(356) | 0.18 |
| $C_6$ | PT | 3.27e-05(289) | 0.98506(346) | -0.0541(152) | 0.98506(345) | 0.01 |
| $C_6$ | KT | 4.92e-05(432) | 0.97850(364) | -0.0529(147) | 0.97842(363) | 0.26 |
| $C_4$ | PT | 8.14e-05(433) | 0.98387(407) | -0.0576(156) | 0.98374(405) | 1.01 |
| $C_4$ | KT | 8.12e-05(774) | 0.96385(551) | -0.0424(163) | 0.96375(549) | 0.01 |
| $B_4$ | PT | 0.00013(5) | 0.97774(248) | -0.0938(72) | 0.97762(247) | 1.03 |
| $B_4$ | KT | 0.00061(8) | 0.95863(791) | -0.0669(131) | 0.95824(789) | 0.05 |
| $B_1$ | PT | 0.00014(9) | 0.96959(597) | -0.0975(110) | 0.96947(596) | 0.52 |
| $B_1$ | KT | na. | na. | na. | na. | na. |

Table 2.8: Table showing values of $q^2$ and the results for the form factors for each set for Kinematic(Kin.) PT and KT.

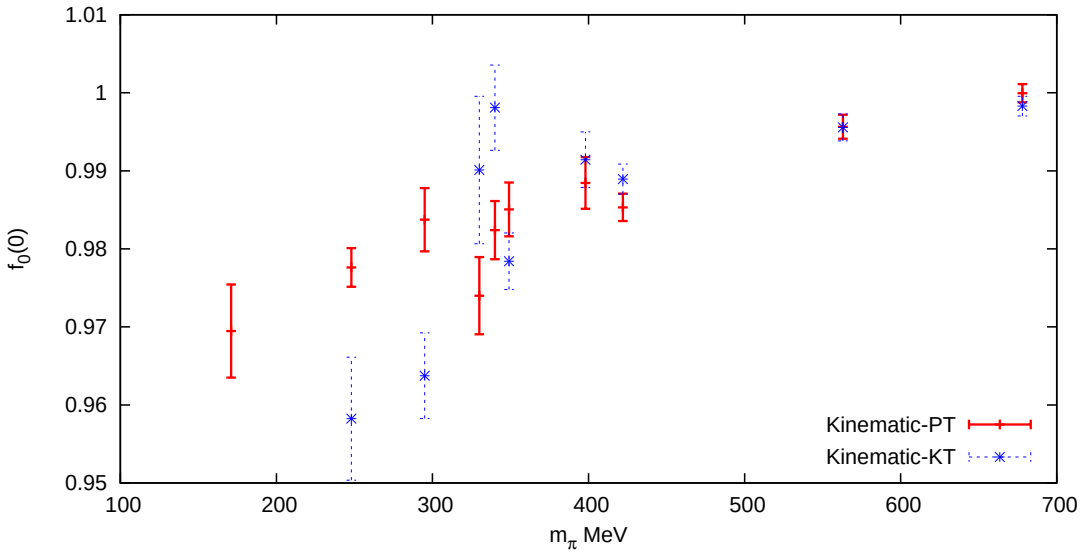


Figure 2.20: Plot of form factors vs simulated pion mass ; comparing value obtained from Kinematic PT and KT as listed in table 2.8

| set | Kin. | $f_+(q^2)$ | $f_-(q^2)$ | $f_0(q^2)$ | $\chi^2/dof$ |
|---|---|---|---|---|---|
| $A_3$ | BT | 0.99917(4) | -0.0274(5) | 0.99917(4) | 1.21 |
| $A_2$ | BT | 0.99563(24) | -0.0572(14) | 0.99562(24) | 0.09 |
| $A_1$ | BT | 0.98675(82) | -0.0883(26) | 0.98674(82) | 3.54 |
| $A_5^4$ | BT | 0.97553(423) | -0.1021(93) | 0.97578(424) | 2.56 |
| $A_5^3$ | BT | 0.98583(271) | -0.0767(72) | 0.98605(272) | 3.20 |
| $C_8$ | BT | 0.99013(149) | -0.0683(103) | 0.99002(150) | 0.28 |
| $C_6$ | BT | 0.98496(200) | -0.0667(95) | 0.98488(199) | 0.75 |
| $C_4$ | BT | 0.98255(303) | -0.0713(107) | 0.98238(302) | 1.85 |
| $B_4$ | BT | 0.97781(239) | -0.0940(71) | 0.97773(238) | 0.77 |
| $B_4$ | PKT | 0.97523(343) | -0.0954(82) | 0.97526(342) | 0.39 |
| $B_4$ | ALLT | 0.97713(197) | -0.0975(54) | 0.97716(197) | 0.95 |
| $B_1$ | BT | na. | na. | na. | na. |
| $B_1$ | PKT | 0.97159(631) | -0.0822(104) | 0.97148(629) | 0.95 |
| $B_1$ | ALLT | 0.97053(404) | -0.0885(83) | 0.97053(404) | 0.88 |

Table 2.9: Table showing results for form factors at $q^2 \approx 0$ for each data set for Kinematic(Kin.) BT, PKT and ALLT.

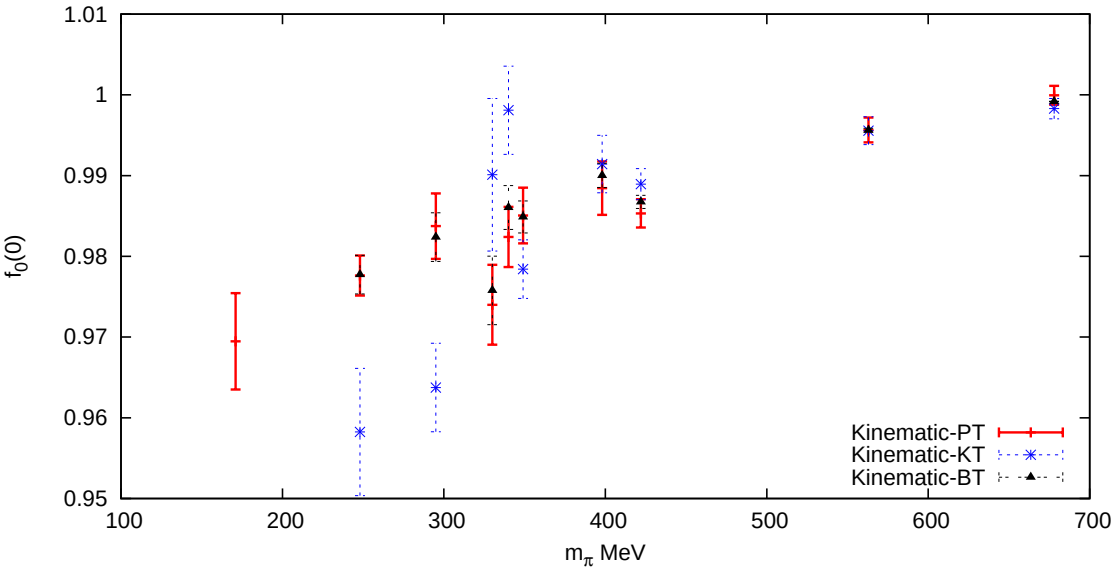


Figure 2.21: Plot of form factors vs simulated pion mass ; comparing value obtained from Kinematic PT, KT and BT as listed in table 2.8 and table 2.9

### 2.8.1 Twisting Kaon Vs Pion

To understand the 2% discrepancy arising from difference in form-factor determined with Kinematic PT and KT, other Kinematic choices should be explored. Kinematic-BT computes $f_0(0)$ by solving globally all the equations in (2.17) corresponding to Kinematic PT and KT. Table 2.9 lists the form-factor value for each data-set determined using Kinematic-BT. For $B_1$, BT cannot be used due to the reason discussed in the previous section 2.6. For each data set, Fig. 2.21 compares the form-factor determined using Kinematic PT,KT and BT. This clearly shows that the form factor values determined from BT are in agreement with that of PT. This gives us good argument to discard Kinematic KT or instead use BT for all data sets.

## 2.9 Form-factor dependence on Twists

In order to find a better choice of kinematic and understand different kinematic used we analysed the situation further: From (2.17), the slope of $f_+(0)$ with

respect to $f_-(0)$ is given by

$$\frac{\partial f_+(0)}{\partial f_-(0)}_{\mu} = -\frac{(\vec{p}_K - \vec{p}_\pi)_\mu}{(\vec{p}_K + \vec{p}_\pi)_\mu} \tag{2.26}$$

and for kinematic options ($\mu = t, x, y, z$) used in (2.17), for the time-component of the vector current, $V_t$,

$$\left.\frac{\partial f_+(0)}{\partial f_-(0)}\right|_{\theta_K=0} = -\frac{m_K - E_\pi}{m_K + E_\pi}\,, \qquad \left.\frac{\partial f_+(0)}{\partial f_-(0)}\right|_{\theta_\pi=0} = -\frac{E_K - m_\pi}{E_K + m_\pi}\,, \tag{2.27}$$

and for the spatial components $V_{x,y,z}$.

$$\left.\frac{\partial f_+(0)}{\partial f_-(0)}\right|_{\theta_K=0} = 1 \qquad \left.\frac{\partial f_+(0)}{\partial f_-(0)}\right|_{\theta_\pi=0} = -1\,, \tag{2.28}$$

For any single kinematic to get a better constraint on $f_+(0)$, the slopes of the time and spatial components should be of different sign (positive or negative). The larger kaon mass will mean that the slope from $V_t$ will always be negative. So a positive slope from $V_{x,y,z}$, will help constrain the relation better. From $V_{x,y,z}$, positive slope is obtained for Kinematic-PT and negative slope for Kinematic-KT. This means slopes of the time and spatial components for Kinematic-KT are negative and the corresponding equations become ill-constrained.

Fig. 2.23, 2.22, 2.24 shows the slope of the equations for kaon only and pion only kinematics (l.h.s. and r.h.s. plots). While all solutions have a negative slope for the case where only the kaon is twisted(KT), there are solutions with opposite slopes in the case where the pion is twisted(PT). Because the solution is given by the intersection of the individual constraints, Kinematic-PT provides the best result. The statistical errors are also smaller in this case. Kinematic-KT is not well constrained as shown by the large intercept where the equations intersect.

Motivated by these observations, we computed all correlation functions once again for a third choice of kinematic-PKT, where both the kaon and the pion are twisted. As shown in the left plot in Fig. 2.24b, this is found to gives us a good alternative for $B_1$ data set where the kaon cannot be twisted to get a signal. Kinematic PKT also leads to a good constraint for $f_+(0)$ for $B_4$.

For $B_4$ with Kinematic-PKT, the result is in agreement with the result obtained by solving all simultaneous equations for the cases where either the pion

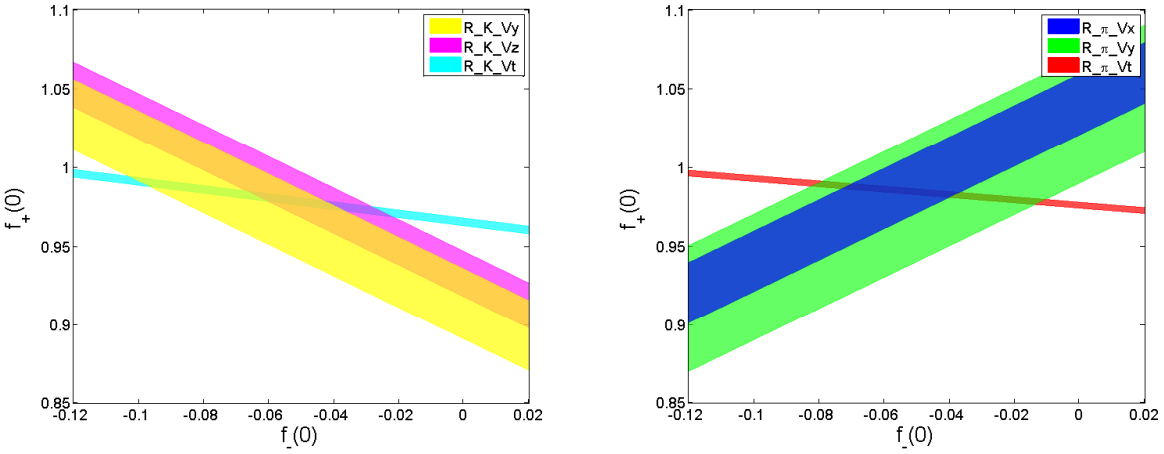


(a) Kinematic KT (left), Kinematic PT (right)

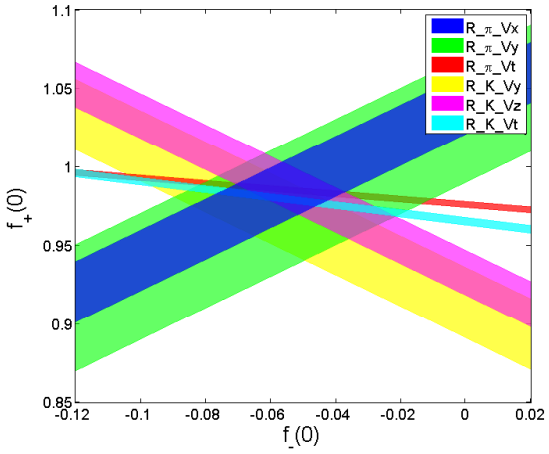


(b) Kinematic BT

Figure 2.22: Plot of $f_+(0)$ vs. $f_-(0)$ for $C_6$ ensemble

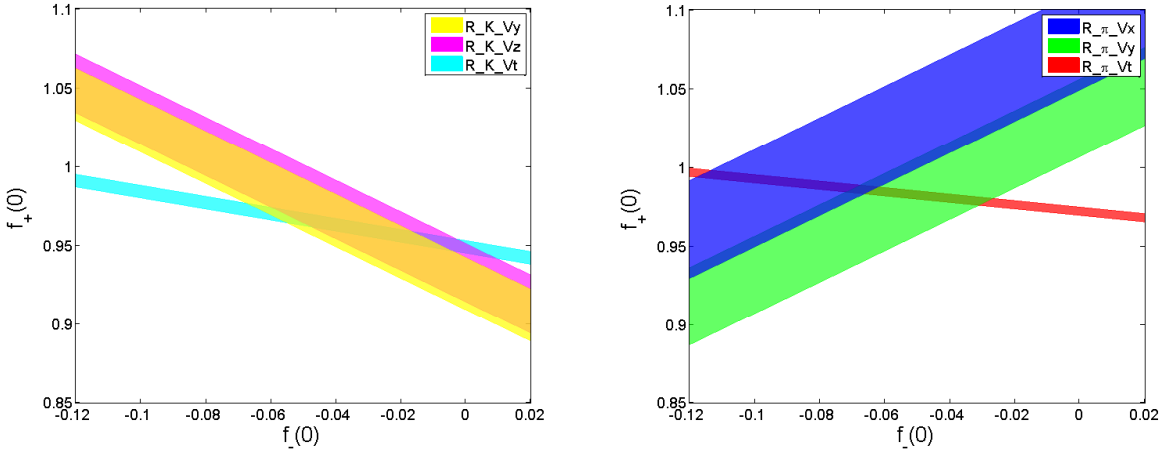


(a) Kinematic KT (left), Kinematic PT (right)

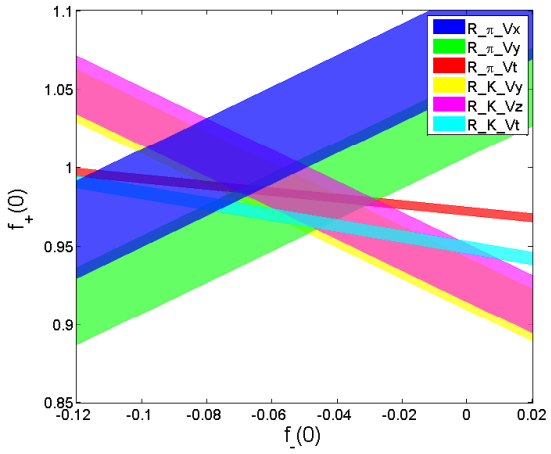


(b) Kinematic BT

Figure 2.23: Plot of $f_+(0)$ vs. $f_-(0)$ for $C_4$ ensemble

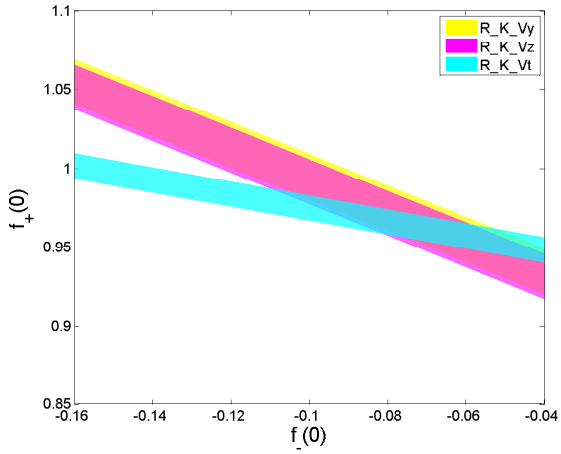


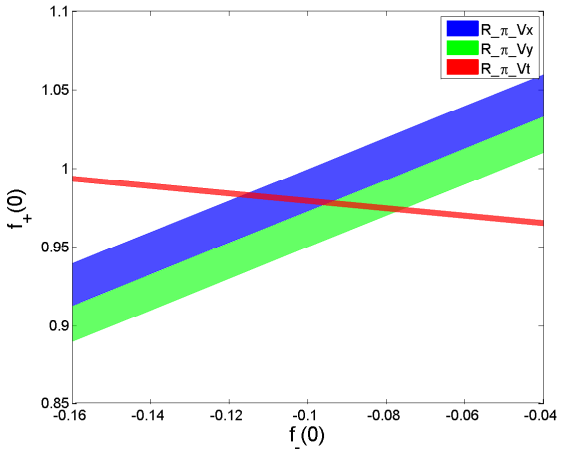


(a) Kinematic KT (left), Kinematic PT (right)

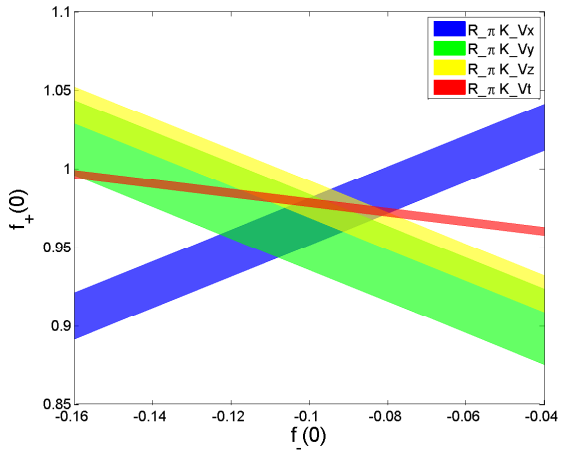


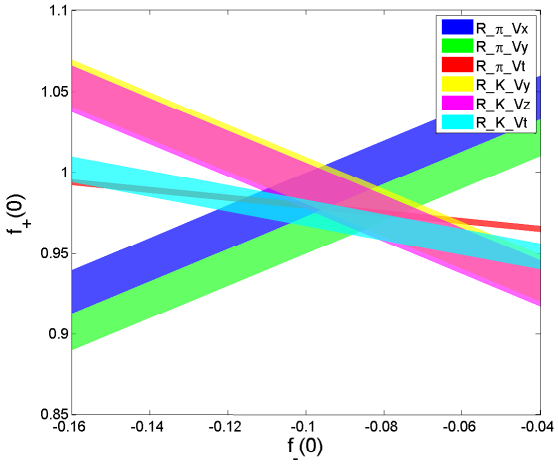


(b) Kinematic PKT (left), Kinematic BT (right)

Figure 2.24: Plot of $f_+(0)$ vs. $f_-(0)$ for $B_4$ ensemble

| *set* | $m_\pi$ $[GeV]$ | $m_K$ $[GeV]$ | $f_0(0)$ |
|---|---|---|---|
| $A_3$ | 0.678(12) | 0.723(13) | 0.99917(4) |
| $A_2$ | 0.563(10) | 0.672(12) | 0.99562(24) |
| $A_1$ | 0.422(8) | 0.612(11) | 0.98674(82) |
| $A_5^4$ | 0.334(7) | 0.581(11) | 0.97578(424) |
| $A_5^3$ | 0.334(7) | 0.522(10) | 0.98605(272) |
| $C_8$ | 0.399(7) | 0.557(10) | 0.99002(150) |
| $C_6$ | 0.349(7) | 0.538(10) | 0.98488(199) |
| $C_4$ | 0.295(6) | 0.522(10) | 0.98238(302) |
| $B_4$ | 0.248(2) | 0.509(4) | 0.97716(197) |
| $B_1$ | 0.170(1) | 0.492(3) | 0.97053(404) |

Table 2.10: $m_\pi$, $m_K$ and $f_0(0)$ for each ensemble.

or the kaon are twisted (Kinematic-BT) as shown in the right plot of Fig. 2.24b (obtained by combining the plots in Fig. 2.24a). Similarly for $C_6$ and $C_4$, result obtained from Kinematic-BT is in agreement with kinematic-PT as shown in Fig. 2.22b and Fig. 2.23b respectively.

The analysed results for $B_1$ and $B_4$ from Kinematic-PKT and ALLT are shown in table 2.9. Fig. 2.25 shows a closer look at the form-factor values for $B_1$ and $B_4$. This shows us that all kinematics are in good agreement except Kinematic-KT and the systematic error arising from the difference in form-factor values from Kinematic PT and KT can be ignored if a better kinematic solution can be used. Thus for all data sets, kinematics are combined if available and so either Kinematic BT or ALLT is always used. The form-factor and meson masses for each of the data set is listed in table 2.10. Here, the form-factor values are determined at unphysical values of meson masses. This data needs to be extrapolated using suitable fit ansatz and this is addressed in the next chapter.

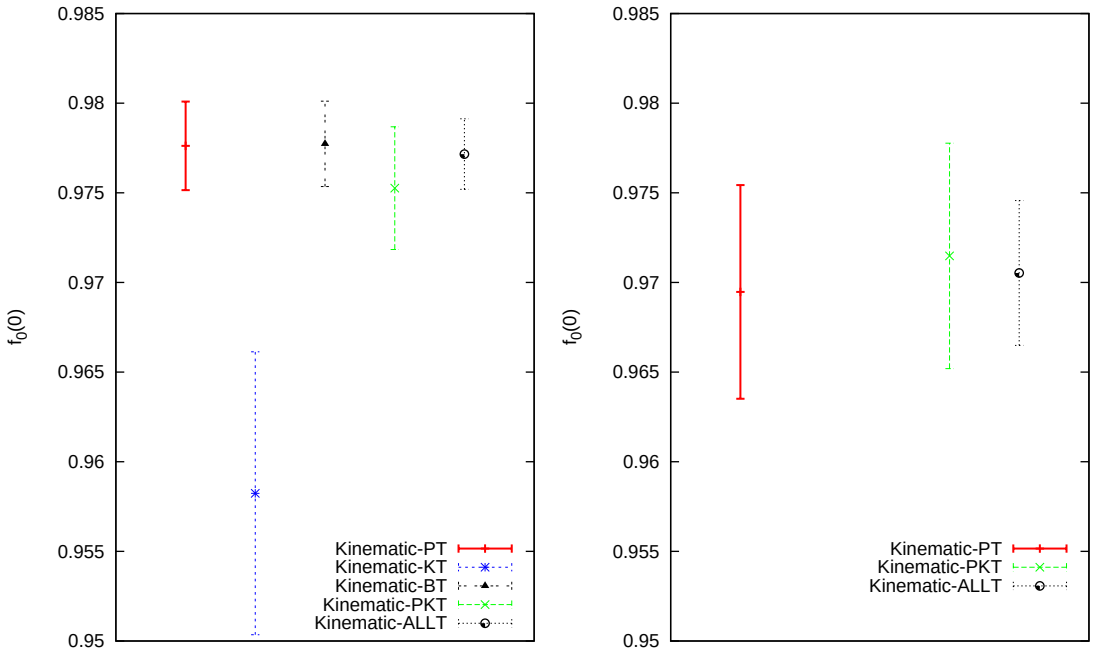


Figure 2.25: Plot of form factor for different kinematics. Left : for data set $B_4$ Right : for data set $B_1$

# Chapter 3

# $K_{l3}$ form factor - Extrapolation

## 3.1 Extrapolation

For computing the value of $V_{us}$, the value of $f_+^{K\pi}(q^2)$ should be calculated at $q^2$=0 and at the charged pion mass $m_{\pi^-} = 139.57\,\text{MeV}$ and the neutral koan mass $m_{K^0} = 497.614\,\text{MeV}$ [Beringer 12]. In the previous chapter, $f_+^{K\pi}(q^2)$ was determined for different values of unphysical quark (kaon and pion) masses. This means mass extrapolating unphysical values $f_+(0)$ to the physical one using a suitable ansatz. This chapter describes the steps followed in finding a suitable ansatz and then estimating the systematic errors associated with $f_+^{K\pi}(0)$ and $V_{us}$. In this chapter, we will denote the physical form-factor by $f_+^{K\pi}(0)$ and unphysical one by $f_+(0)$.

Previous work [Boyle 08b] used the following ansatz with four fit parameters $A_0, A_1, M_0, M_1$ to simultaneously fit $f_0(q^2)$ dependence on $q^2$ and quark masses. We will refer to it as "simul-fit". This is successfully used to extrapolate 24Coarse ensembles. The result of this previous work (2.18) was reproduced for completeness and verification purposes.

$$f_0^{K\pi}(q^2, m_\pi^2, m_K^2) = \frac{1 + f_2 + (m_K^2 - m_\pi^2)^2(A_0 + A_1(m_K^2 + m_\pi^2))}{1 - q^2/(M_0 + M_1(m_K^2 + m_\pi^2))^2} \tag{3.1}$$

where the term $f_2$ in the above expression is defined as

$$\begin{aligned} f_2 &= \frac{3}{2}H_{\pi K} + \frac{3}{2}H_{\eta K} \\ H_{PQ} &= -\frac{1}{64\pi^2 f_d^2}\left[M_P^2 + M_Q^2 + \frac{2M_P^2 M_Q^2}{M_P^2 - M_Q^2}\ln\frac{M_Q^2}{M_P^2}\right] \end{aligned} \tag{3.2}$$

The numerator of the simul-fit (3.1) is motivated from the Ademello-Gatto theorem [Ademollo 64], whereas the denominator is a standard pole fit for quark mass dependence. In the above ansatz $f_2$ can be calculated accurately from lattice results of $m_K^2, m_\pi^2, m_\eta^2$ and decay constant $f_d$. $f_d$ refers to pion constant $f_\pi$ at the SU(3) chiral limit and the difference of $f_d$ from $f_\pi$ remains theoretically uncertain. $f_d$ is chosen to be 130 MeV [etal 06] for further discussions unless specified otherwise. In the following sections, we will separately study the $q^2$ and quark mass dependence of the simul-fit.

For clarity, definition of some frequently used terms are summarised below. "Cutoff" in this section for $m_\pi$ and $q^2$ will refer to selection of data for which $m_\pi$ and $q^2$ are less than the quoted cutoff value. Where a cutoff is not quoted, all data is included in obtaining a fit. "Physical limit" refers to point at which $m_\pi = 139.57\,\text{MeV}$ and $m_K = 497.614\,\text{MeV}$ and the "SU(3) symmetric limit" refers to the point where $m_\pi = m_K$ and $f_0(0) = 1$. As shown in table 2.10 data sets $A_5^4, B_4, B_1$ are closer to physical limit and data sets $A_3, A_2, C_8$ are closer to SU(3) symmetric limit.

An important update in this thesis is the way the dependence of form factor on quark masses is analysed. In previous studies by RBC-UKQCD, this dependence is understood by plotting $f_0(0)$ as a function of $m_\pi^2$ which required additional terms that parametrise the dependence on the strange quark masses.

In this thesis, $f_0(0)$ was studied as a function of $(m_K^2 - m_\pi^2)^2/m_K^2$. This term appears as a leading term in the Taylor expansion of $f_2$ around the SU(3) symmetric point [Leutwyler 84, Becirevic 06]. We can write the expression in (3.2) as follows

$$H_{PQ} \propto M_P^2 + M_Q^2 + \frac{2M_P^2 M_Q^2}{M_P^2 - M_Q^2} \ln(\frac{M_Q^2}{M_P^2}) \tag{3.3}$$

Expanding the terms in $H_{PQ}$ around the SU(3) symmetric point($M_K^2 = M_\pi^2$),

$$\begin{aligned} \ln(\frac{M_Q^2}{M_P^2}) &= -\frac{M_P^2 - M_Q^2}{M_Q^2} + \frac{(M_P^2 - M_Q^2)^2}{2(M_Q^2)^2} \\ &- \frac{(M_P^2 - M_Q^2)^3}{3(M_Q^2)^3} + \frac{(M_P^2 - M_Q^2)^4}{4(M_Q^2)^4} + \dots \\ \frac{2M_P^2 M_Q^2}{M_P^2 - M_Q^2} &= \frac{2(M_Q^2)^2}{M_P^2 - M_Q^2} + 2M_Q^2 + \dots \end{aligned} \tag{3.4}$$

Multiplying the expanded terms,

$$\begin{aligned}\frac{2M_P^2M_Q^2}{M_P^2-M_Q^2}\ln(\frac{M_Q^2}{M_P^2}) &= -M_P^2-M_Q^2+\frac{(M_P^2-M_Q^2)^2}{3(M_Q^2)^2} \\ &- \frac{(M_P^2-M_Q^2)^3}{6(M_Q^2)^2}+\frac{(M_P^2-M_Q^2)^4}{10(M_Q^2)^3}+\ldots \end{aligned} \tag{3.5}$$

Thus we can write the Taylor expansion of $H_{PQ}$ as follows

$$H_{PQ} \propto \frac{(M_P^2-M_Q^2)^2}{3M_Q^2}-\frac{(M_P^2-M_Q^2)^3}{6(M_Q^2)^2}+\frac{(M_P^2-M_Q^2)^4}{10(M_Q^2)^3}+\ldots \tag{3.6}$$

We shall see that this parametrisation in fact describes the strange quark mass dependence surprisingly well without additional terms. The first use of this parametrisation in extrapolating $K_{l3}$ was made in this thesis work.

In the chiral expansion of $f_+(0) = 1 + f_2 + f_4 + \ldots$, the Ademollo-Gatto theorem [Ademollo 64] states that $f_+(0)$ receives corrections from 1, that are second order in $(m_K^2 - m_\pi^2)$. Because of this, Leutwyler and Roos [Leutwyler 84] observed that $f_2$ does not receive contributions from beyond leading order terms in the chiral effective Lagrangian, and may be expressed only in terms of $m_K$, $m_\pi$ and $f_\pi$. The theoretical uncertainty in the low energy constant at the SU(3) symmetric chiral limit ($m_u = m_d = m_s = 0$) appearing in $f_2$, makes this expression somewhat uncertain since this differs in principle from the $f_\pi$ measured for non-zero mass physical quarks[Allton 08].

In extrapolation of lattice data at unphysical quark masses, analytic functions have proved to be a good alternative to chiral effective theory[Aoki 11, Arthur 13]. Although the chiral effective theory is formally the correct expansion of $K_{l3}$ form factor around zero quark mass, both the physical point and even more so the lattice data points are at non-zero quark masses.

Both the radius of convergence of the chiral effective theory and the region in which using a few terms of the series is accurate, are unknown without lattice input. Analytic expansion will be formally correct provided we stay away from the non analytic behaviour at zero quark masses. Of course, in principle an analytic fit may require more terms for accurate extrapolation to the physical point in the presence of chiral curvature. The use of analytic forms has been successful in quantifying the systematic error in the use of chiral effective fits by comparing it

to the NLO ansatz [Aoki 11].

In $K_{l3}$, the symmetry of $f_+(0) = 1$ for $m_K = m_\pi \neq 0$ is encoded in the SU(3) effective theory. Instead of using a naive analytic expansion, the SU(3) effective theory therefore forms the basis of our analytic expansion. This symmetry holds good for arbitrarily large $m_K = m_\pi$. By taking $(m_K^2 - m_\pi^2)^2/m_K^2$ as an analytic expansion parameter, we form a analytic expansion that respects this symmetry at both the physical point and lattice data points. Surprisingly, we shall see that this single expansion parameter in fact describes the complete pion and kaon mass dependence of all our lattice data points with a first or second order polynomial. The fit ansatz motivated by this analytic expansion will be explained in detail in section 3.3.

### 3.1.1 $q^2$ dependence

In the above ansatz (3.1) (simul-fit), we can completely ignore the denominator if momentum interpolation is done to compute $f_0(q^2)$ at $q^2$=0. We can either use a fit ansatz to perform $q^2$-interpolation or use partially twisted boundary conditions to determine $f_0(q^2)$ at $q^2$=0. Fig. 3.1 shows $f_0(q^2)$ dependence on $q^2$ for all the ensembles. With $q^2$ ranging from -0.4 to 0.1, all the $f_0(q^2)$ values can be used in simul-fit (3.1) to determine $A_0, A_1, M_0, M_1$. We can then compute $f_0(0)$ by setting $q^2 = 0$, $m_\pi = 139.57$ MeV and $m_K = 497.614$ MeV. Fitting all $q^2$ information, $f_0^{K\pi}(0)$ is found to be $0.9625(14)_{stat}$ with $\chi^2/dof = 2.18$. $\chi^2/dof$ denotes the quality of the fit and a value of less than 1 is considered a good fit.

Using partial twisted boundary conditions, we have evaluated $f_0(q^2)$ at $q^2 \approx$0 as listed in table 2.10. Fig. 3.2 shows the $f_0(q^2)$ of each data set at $q^2$ in the range: -0.00057 to +0.00053($q^2 \approx 0$). We can reduce the $q^2$ dependence in the simul-fit by selecting $f_0(q^2)$ based on $q^2$ cutoff. Similarly, we can repeat the fit with $m_\pi$ cutoff where data sets are included or excluded from the extrapolation based on the mass cutoff.

Table 3.1 tabulates $f_0^{K\pi}(0)$ determined for different cutoff of $q^2$ and $m_\pi$. For the case where we include all data sets to fit, we can infer that the $\chi^2/dof$ reduces 4 times (from 2.49 to 0.49) as $f_0(q^2)$ values at $q^2 > 0.001$ are excluded from the fit, even if statistical error increases by 30%. Also excluding the values at $q^2 > 0.001$ reduces the variance of $f_0(q^2)$ for different $m_\pi$ cutoffs. Fig. 3.3 shows how the simul-fit better fits the individual data points when $q^2$ cutoff is

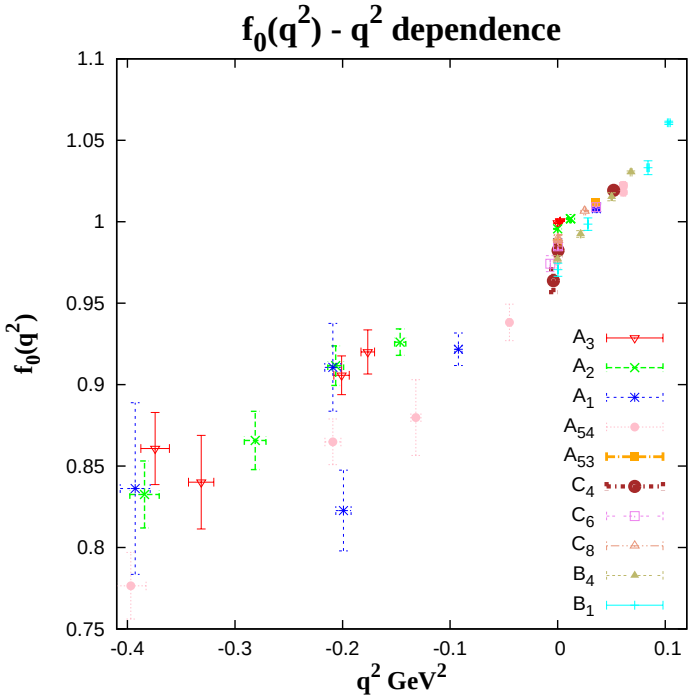


Figure 3.1: Plot of $f_0(q^2)$ dependence on $q^2$ for all data sets.

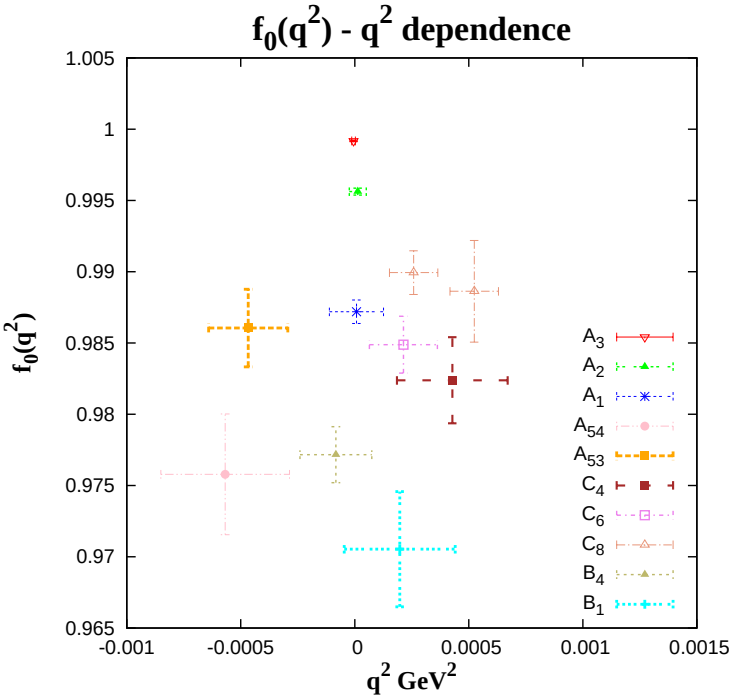


Figure 3.2: Plot of $f_0(q^2)$ dependence on $q^2$ for $q^2 \approx 0$. This plot is a $q^2$ zoom of Fig. 3.1

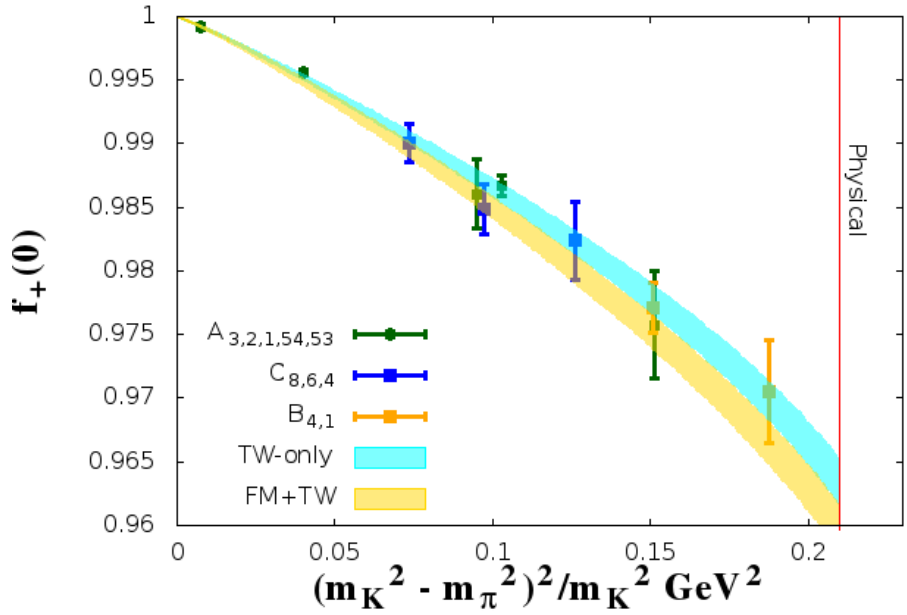


Figure 3.3: Plot showing simul-fit of $f_0^{K\pi}(q^2)$ for different cutoff of $q^2$. For "TW only", $f_0(0)$ determined using twisted boundary conditions (table 2.10) are used. "FM+TW" uses all $f_0(q^2)$ (also values generated using Fourier modes for 24Coarse.)

| $m_\pi$ cutoff | $\lvert q^2\rvert$cutoff GeV | | | |
|---|---|---|---|---|
| | 1 | 0.1 | 0.01 | 0.001 |
| 700 | $0.9625(14)_{2.18}$ | $0.9636(14)_{1.97}$ | $0.9642(18)_{1.25}$ | $0.9635(20)_{0.49}$ |
| 600 | $0.9605(26)_{2.04}$ | $0.9621(16)_{1.98}$ | $0.9632(21)_{1.14}$ | $0.9636(20)_{0.52}$ |
| 500 | $0.9587(20)_{2.21}$ | $0.9608(22)_{2.22}$ | $0.9612(27)_{1.22}$ | $0.9618(30)_{0.45}$ |
| 400 | $0.9592(22)_{2.44}$ | $0.9628(27)_{2.53}$ | $0.9632(33)_{0.27}$ | $0.9639(33)_{0.16}$ |
| 300 | $0.9655(36)_{1.63}$ | $0.9687(38)_{1.26}$ | $0.9651(53)_{0.00}$ | na. |
| sys | $0.9625(14)(^{+30}_{-38})$ | $0.9636(14)(^{+51}_{-18})$ | $0.9642(18)(^{+9}_{-30})$ | $0.9635(20)(^{+4}_{-17})$ |

Table 3.1: $f_0^{K\pi}(0)$ determined for different cutoffs of $q^2$ and $m_\pi$ using simul-fit (3.1) and $f_d = 130$ MeV. Subscript for $f_0^{K\pi}(0)$ values denote $\chi^2$/dof of the simul-fit.

| | Pole | | Quadratic | |
|---|---|---|---|---|
| *set* | $f_+(0)$ | $\chi^2$/dof | $f_+(0)$ | $\chi^2$/dof |
| 24Coarse | | | | |
| $A_3$ | 0.99916(6) | 0.42 | 0.99917(5) | 0.35 |
| $A_2$ | 0.99569(26) | 0.20 | 0.99565(24) | 0.20 |
| $A_1$ | 0.98677(82) | 1.89 | 0.98687(80) | 1.73 |
| $A_5^4$ | 0.97747(282) | 1.44 | 0.97589(344) | 1.34 |
| $A_5^3$ | 0.98638(269) | na. | na. | na. |
| 32Fine | | | | |
| $C_8$ | 0.98954(175) | 0.15 | 0.99124(273) | na. |
| $C_6$ | 0.98377(231) | 1.20 | 0.98459(209) | 1.20 |
| $C_4$ | 0.97950(334) | 4.10 | 0.98065(341) | na. |
| 32Coarse | | | | |
| $B_4$ | 0.97684(185) | 0.06 | 0.97720(192) | 0.01 |
| $B_1$ | 0.97191(348) | 3.20 | 0.97321(399) | 3.08 |

Table 3.2: Results for $f_+(0)$ using pole dominance (3.8) and quadratic (3.7) fits to each data set

used. In this plot "TW only" uses only $f_0(q^2)$ values at $q^2 < 0.001$ to simul-fit, whereas "FM+TW" uses all $f_0(q^2)$ values including the one generated using Fourier modes for 24Coarse ensemble. From Fig. 3.3, we can infer that the $f_0(q^2)$ values at $q^2 \gg 0$ can be ignored to get a accurate fit.

Simul-fit (3.1) can also be performed by first interpolating $f_0(q^2)$ values to $f_0(0)$ using a suitable ansatz and then extrapolating the $f_0(0)$ values to that of physical quark masses. For $q^2$ interpolation, a pole or a quadratic fit can be used as listed below.

$$\text{Quadratic} : f_0(q^2) = a_0 + a_1 q^2 + a_2 q^4 \tag{3.7}$$

$$\text{Pole} : f_0(q^2) = f_0(0)/(1 - q^2/M^2) \tag{3.8}$$

The pole and quadratic fits are repeated for all the ensembles. Table 3.2 summarises the results of pole and quadratic fit for each of the data sets. Appendix A shows the plot of pole, quadratic and simul fit for each individual fit.

With all $q^2$ data included, data sets $B_1$,$C_4$,$A_5^4$ and $A_1$ have $\chi^2$/dof $> 1$. Similar to the simul-fit the $\chi^2$/dof of pole and quadratic fit reduces as $q^2$ cutoff is introduced. Once $f_0(0)$ is determined using ansatz (3.7) or (3.8), we can use the

numerator of (3.1) to extrapolate as we are left with only two free parameters $A_0, A_1$.

$$f_0(q^2, m_\pi^2, m_K^2) = 1 + f_2 + (m_K^2 - m_\pi^2)^2(A_0 + A_1(m_K^2 + m_\pi^2)) \tag{3.9}$$

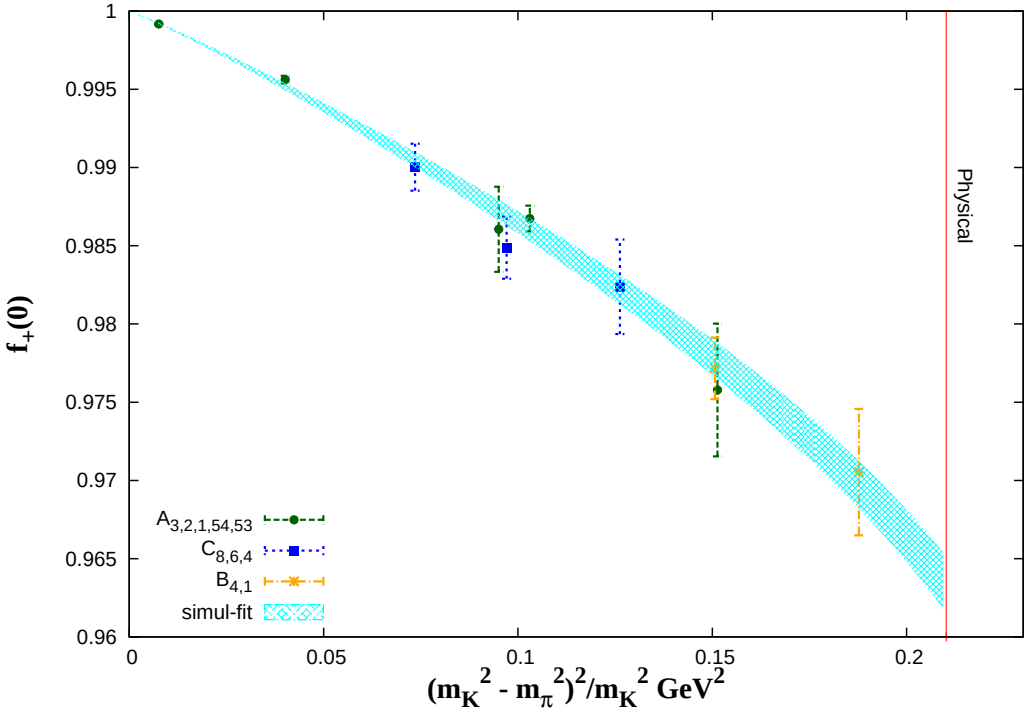


Figure 3.4: Plot showing simul-fit (3.9) of $f_0^{K\pi}(q^2)$ using $f_0(0)$ determined using twisted boundary conditions only (table 2.10)

Tables 3.3 and 3.4 lists $f_0^{K\pi}(0)$ determined for different cutoff of $q^2$ and $m_\pi$ using pole (3.7) and quadratic (3.8) fits respectively for $q^2$ interpolation and then extrapolating using fit (3.9). We can observe similar behaviour as that for simul-fit (3.1). In table 3.4 simul fit for $|q^2| < 0.001$ cannot be performed as we have only one $f_0(0)$ value whereas quadratic fit needs at least two. Also with $q^2$cutoff $< 0.001$, we can observe that $f_0^{K\pi}(0)$ shows reduced variance when $m_\pi$ cutoff is applied.

Fig. 3.4 shows mass extrapolation using fits (3.8) and (3.9). This is similar to the simul-fit (3.1) as shown in Fig.3.3. Using twisted boundary conditions, we have computed $f_0(q^2)$ at $q^2 \approx 0$. Using only the $f_0(q^2)$ values $q^2 \approx 0$, we have improved the $\chi^2$/dof for the simul-fit and reduced the model dependence of $q^2$

| $m_\pi$ cutoff | $\|q^2\|$cutoff GeV | | | |
|---|---|---|---|---|
| | 1 | 0.1 | 0.01 | 0.001 |
| 700 | $0.9641(16)_{0.70}$ | $0.9641(16)_{0.87}$ | $0.9643(16)_{0.56}$ | $0.9646(16)_{0.53}$ |
| 600 | $0.9629(19)_{0.55}$ | $0.9632(19)_{0.87}$ | $0.9633(19)_{0.50}$ | $0.9636(19)_{0.45}$ |
| 500 | $0.9621(23)_{0.59}$ | $0.9623(23)_{0.96}$ | $0.9615(25)_{0.39}$ | $0.9619(24)_{0.36}$ |
| 400 | $0.9638(26)_{0.45}$ | $0.9652(26)_{0.47}$ | $0.9638(29)_{0.13}$ | $0.9641(28)_{0.12}$ |
| 300 | $0.9667(38)_{0.00}$ | $0.9689(39)_{0.11}$ | $0.9651(44)_{0.00}$ | $0.9642(43)_{0.13}$ |
| sys | $0.9641(16)(^{+26}_{-20})$ | $0.9641(16)(^{+48}_{-18})$ | $0.9643(16)(^{+9}_{-28})$ | $0.9646(16)(^{+0}_{-27})$ |

Table 3.3: $f_0^{K\pi}(0)$ determined for different cutoff of $q^2$ and $m_\pi$ using fit ansatz (3.9) and $f_d = 130$ MeV. Subscript for $f_0^{K\pi}(0)$ values denote $\chi^2$/dof of the fit ansatz (3.9).

| $m_\pi$ cutoff | $\|q^2\|$cutoff GeV | | | |
|---|---|---|---|---|
| | 1 | 0.1 | 0.01 | 0.001 |
| 700 | $0.9646(16)_{0.60}$ | $0.9643(16)_{0.47}$ | $0.9647(17)_{0.35}$ | na. |
| 600 | $0.9637(19)_{0.56}$ | $0.9637(19)_{0.49}$ | $0.9643(21)_{0.39}$ | na. |
| 500 | $0.9628(25)_{0.63}$ | $0.9620(25)_{0.37}$ | $0.9628(27)_{0.26}$ | na. |
| 400 | $0.9649(29)_{0.44}$ | $0.9637(30)_{0.27}$ | $0.9642(31)_{0.05}$ | na. |
| 300 | $0.9676(43)_{0.10}$ | $0.9649(44)_{0.00}$ | $0.9651(51)_{0.00}$ | na. |
| sys | $0.9646(16)(^{+30}_{-18})$ | $0.9643(16)(^{+6}_{-23})$ | $0.9647(17)(^{+5}_{-19})$ | na. |

Table 3.4: $f_0^{K\pi}(0)$ determined for different cutoff of $q^2$ and $m_\pi$ using fit ansatz (3.9) and $f_d = 130MeV$. Simul fit for $|q^2| < 0.001$ cannot be performed as we have only one $f_0(0)$ value whereas quadratic fit needs at least two values. Subscript for $f_0^{K\pi}(0)$ values denote $\chi^2$/dof of the fit ansatz (3.9).

interpolation. Using the above argument, we exclude $f_0(q^2)$ at $q^2 > 0$ for further analysis. This also greatly reduces any systematic error from $q^2$ dependence from entering our mass extrapolation.

### 3.1.2 Strange quark dependence

In addition to the $q^2$ dependence of simul-fit, we should also model the strange quark mass dependence as the simulated strange quark mass is not exactly at the physical point. We have chosen the scaling trajectory of our bare parameters to leave $m_K$, $m_\pi$ and $m_\Omega$ free from lattice artefacts when the scale is set using the omega baryon mass. For masses nearby the light and strange physical point, we may taylor expand around the physical point. Here, we consider only the leading corrections linear in the light quark mass and strange quark mass. Continuity in the mass parameters means that the coefficient of $a^2$ corrections will also be small.

We can use $m_\pi^2$ as a non-perturbative measure of the light quark mass, which is linear in leading order, and conclude that the slope $m_K^2$ with $m_\pi^2$ must be the same on each ensemble since this comes from the leading term in the deviation of the simulated light quark mass from the physical point. The leading effect from the strange quark mass will only change the intercept. This approximation amounts to ignoring the higher order cross terms and non-linear terms in our expansion around the physical point. Fig. 3.5 plot the dependence of kaon and pion masses for each ensemble. So $m_K$ and $m_\pi$ of each ensemble is fitted using ansatz (3.10).

$$m_K^2 = X \ + Y \ m_\pi^2 \tag{3.10}$$

Y should be the same across all 3 sets of ensembles, but with different X's. We used constrained fit to solve system of equations for all 3 ensembles at once.

$$\begin{aligned} m_K^2 &= X_1 \ + Y \ m_\pi^2 \\ m_K^2 &= X_2 \ + Y \ m_\pi^2 \\ m_K^2 &= X_3 \ + Y \ m_\pi^2 \end{aligned} \tag{3.11}$$

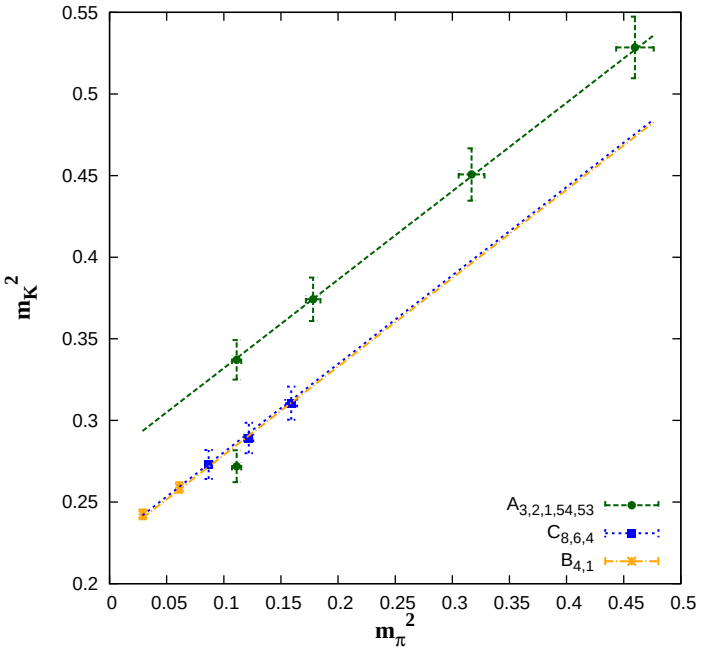


Figure 3.5: Plot showing relation between $m_K^2$ (GeV$^2$) and $m_\pi^2$ (GeV$^2$) for all the ensembles

Fitting for all three ensembles, we obtain

$$\begin{aligned} \text{24Coarse} \;:\; \mathrm{m_K^2} &= 0.2808(106) + 0.5211(3)\,\mathrm{m_\pi^2} \\ \text{32Fine} \;:\; \mathrm{m_K^2} &= 0.2271(31) + 0.5211(3)\,\mathrm{m_\pi^2} \\ \text{32Coarse} \;:\; \mathrm{m_K^2} &= 0.2275(8) + 0.5211(3)\,\mathrm{m_\pi^2} \end{aligned} \tag{3.12}$$

Using the above fit to predict for physical strange quark, kaon mass is written as:

$$\text{Physical limit} \;:\; \mathrm{m_K^2} = 0.2336 + 0.5211(3)\,\mathrm{m_\pi^2} \tag{3.13}$$

For the strange quark mass correction, we should use (3.13) to determine the Kaon mass for physical strange quark on each ensemble. With the corrected strange quark, the difference of $f_0(0)$ evaluated with both corrected Kaon mass and the original Kaon mass at fixed $m_\pi$ gives the correction for $f_0(0)$ as shown in (3.14).

$$f_0(0) = f_0(0) + f_0(0)_{phy} - f_0(0)_{latt} \tag{3.14}$$

Here, $f_0(0)_{latt}$ is determined from the data sets with unphysical strange quark

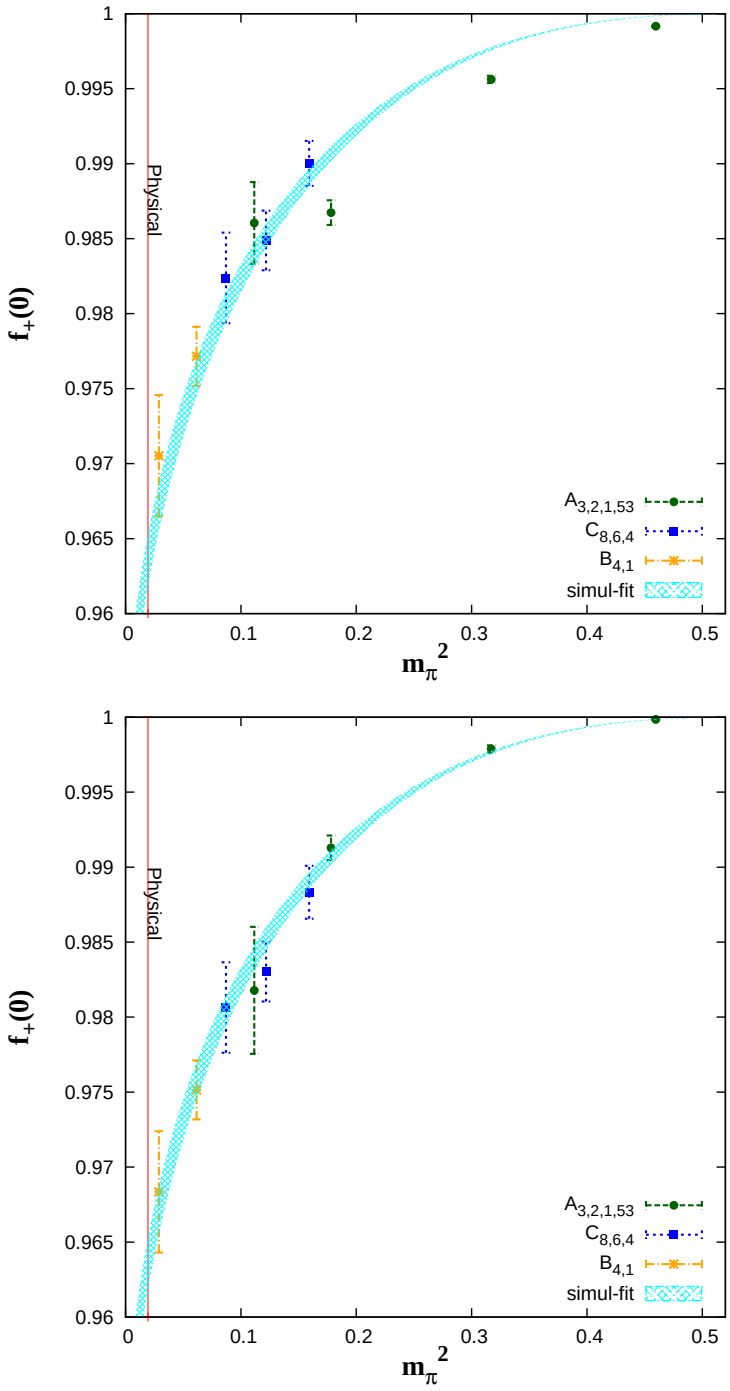


Figure 3.6: Plot of $f_+(0)$ dependence on $m_\pi^2$. Top : raw data points at the simulated (uncorrected) strange quark masses. Bottom : The data points are shifted to physical strange quark mass. In both plots, the curve uses a parametrisation for the Kaon mass with strange quark held fixed at its physical value.

| $m_\pi$ cutoff | $f_0(0)$ | $f_d\,GeV$ | $\chi^2/dof$ |
|---|---|---|---|
| 700 | 0.9606(35) | 0.108(16) | 0.52 |
| 600 | 0.9629(38) | 0.129(100) | 0.39 |
| 500 | 0.9661(36) | 0.630(292) | 0.15 |
| 400 | 0.9663(39) | 0.310(246) | 0.14 |
| 300 | 0.9655(68) | 0.659(381) | 0.03 |

Table 3.5: $f_0^{K\pi}(0)$ and decay constant $f_d$ determined for different cutoff of $m_\pi$ using simul-fit (3.1) with $f_d$ as a free parameter.

masses and $f_0(0)_{phy}$ is determined from using original value of $m_\pi$ and corrected $m_K$ (from (3.13)) in simul-fit ansatz (3.1). All this, however, has no bearing on the final value of $f_0^{K\pi}(0)$ since that comes directly from the SU(3) fit and so is automatically corrected. Fig. 3.6 shows $f_+(0)$ plotted as a function of $m_\pi^2$ for all ensembles. The data points in Fig. 3.6(top) are the ones for the simulated, i.e. unphysical strange-quark mass. After fitting the points using simul-fit (3.1) and then correcting towards the physical strange-quark mass, all data points line up on the fit-curve in the bottom plot of Fig. 3.6.

## 3.2 Decay constant - NLO Fit

As noted in [Boyle 10] one does not know the true value of SU(3) low energy decay constant $f_d$ entering $f_2$. Certain choices amount to different forms of higher-order terms in the expansion of the form factor. A straight forward method will be to add $f_d$ as a free parameter to the simul-fit along with $A0, A1, M0, M1$.

Table 3.5 lists $f_0^{K\pi}(0)$ and decay constant $f_d$ determined for different cutoff of $m_\pi$ using simul-fit ansatz (3.1) with $f_d$ also as a free parameter. With more parameters to fit, this method becomes noisy as denoted by the error of $f_d$ and variance of $f_0^{K\pi}(0)$ for different $m_\pi$ cutoffs. For $m_\pi$ cutoff $> 500$, the $\chi^2$ minimisation is dependent on the starting value of $f_d$ used in the simul-fit. This results in a underdetermined $f_0^{K\pi}(0)$ value. One of the reasons is due to the fact that as we are closer to the SU(3) symmetric limit($m_\pi$ cutoff $> 500$), the NNLO contribution becomes $\approx 0$. As we move closer to the physical limit, $f_d$ seems to prefer a value $\gg f_\pi$ as shown in table 3.5.

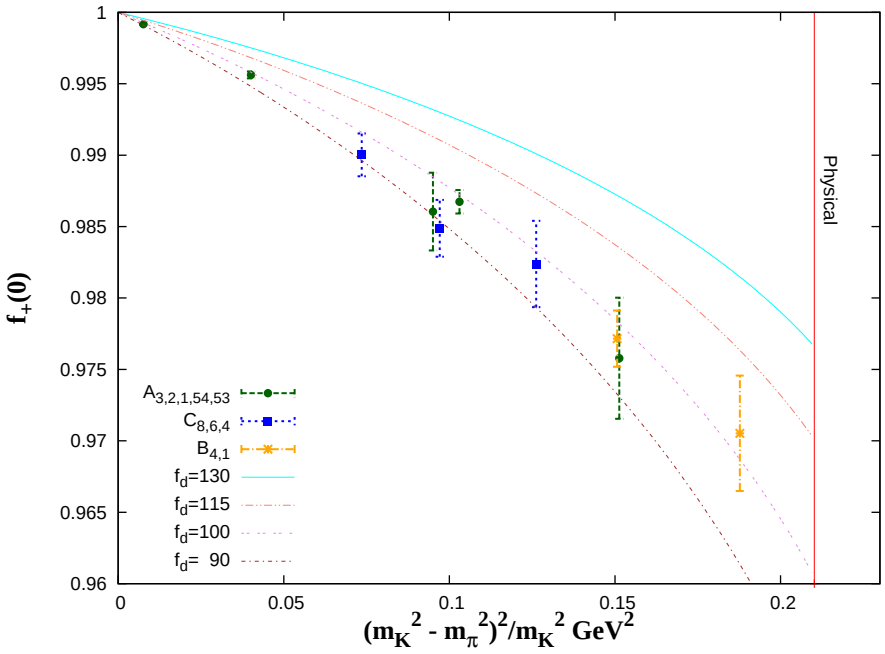


Figure 3.7: Plot showing $1 + f_2$ for different values of $f_d$, with $f_0(0)$ determined using twisted boundary conditions (table 2.10) .

If NNLO contribution is very small and we can approximate form-factor as

$$f_0(0) = 1 + f_2 \tag{3.15}$$

This leaves us with only one free parameter as compared to 5 in (3.1). Table 3.6 summarises $f_d$ and $f_0^{K\pi}(0)$ obtained for different $m_\pi$ cutoffs. Compared to fit shown in table 3.5, $\chi^2/dof < 1$ and $f_0^{K\pi}(0)$, $f_d$ show less variance. $f_d$ is found to lie within the range from 96 to 101 MeV. Fig. 3.7 shows how $1 + f_2$ for different values of $f_d$ fits $f_0(0)$ values of each ensemble. We can infer that $f_d$=100 MeV describes almost all the lattice data. This contradicts the results obtained by allowing $f_d$ to be a free parameter in simul-fit.

Even though $f_d$ is well constrained by $1 + f_2$, the NNLO contribution cannot be ignored. The simul-fit should be repeated with different choices of $f_d$ to check if the NNLO contribution can be ignored. Fig. 3.8 shows $f_0^{K\pi}(q^2)$ for different values of $f_d$. From the plots, lighter data points introduced in this thesis prefers $f_d \approx 130 - 150$ MeV. Simul-fit with $f_d \approx 95 - 100$ MeV seem to fit all data sets except $f_0(0)$ at lightest pion mass ($B1$). Since $B1$ is closer to the physical point,

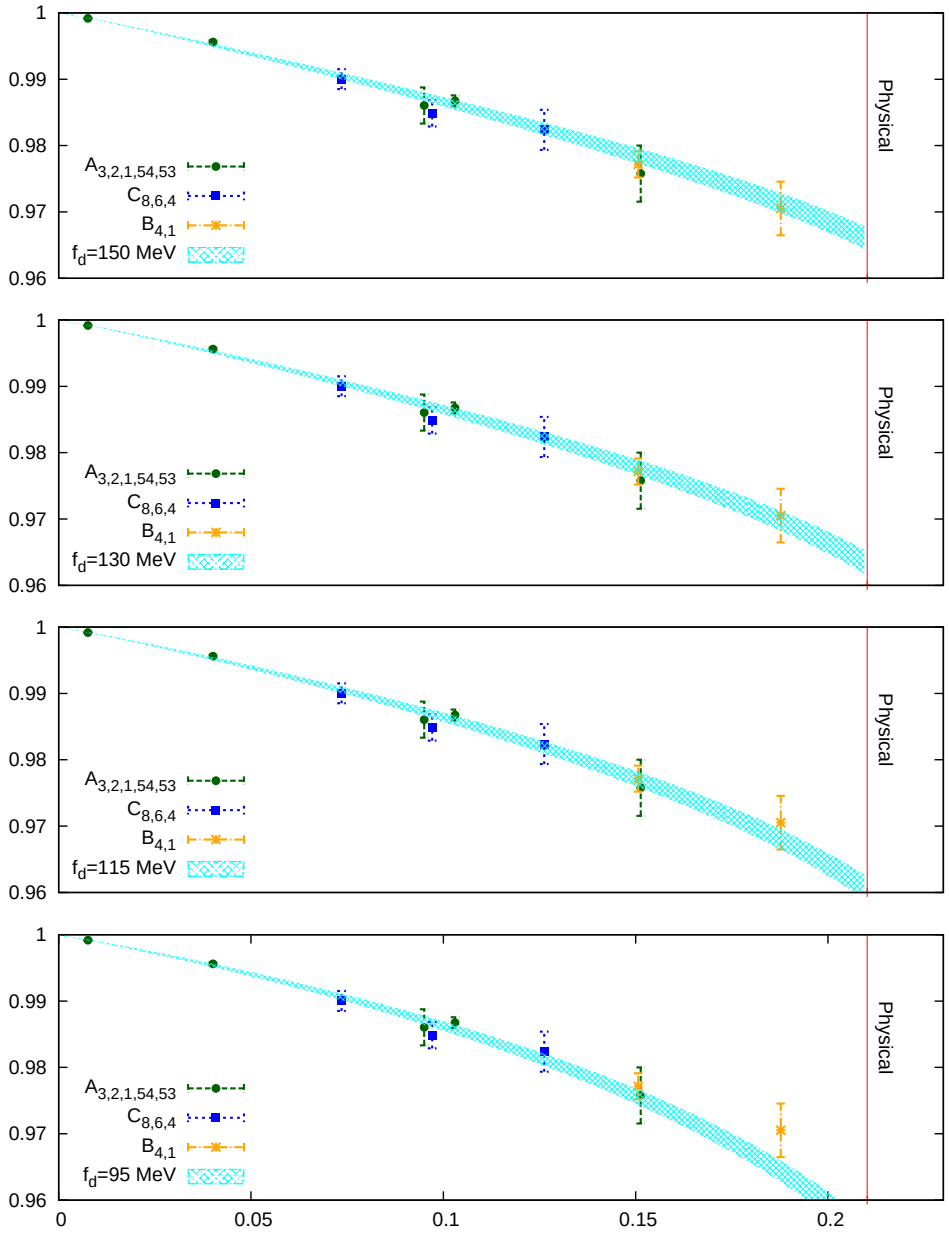


Figure 3.8: Plot showing $f_0^{K\pi}(q^2)$ determined using simul-fit as a function of $(m_K^2 - m_\pi^2)^2/m_K^2$ for different values of $f_d$. Only $f_0(0)$ determined using twisted boundary conditions (table 2.10) are used in the fit.

| $m_\pi$ cutoff | $f_0^{K\pi}(0)$ | $f_d\,GeV$ | $\chi^2/dof$ |
|---|---|---|---|
| 700 | 0.9582(18) | 0.0972(21) | 0.70 |
| 600 | 0.9574(19) | 0.0963(21) | 0.58 |
| 500 | 0.9575(20) | 0.0964(23) | 0.67 |
| 400 | 0.9581(25) | 0.0971(29) | 0.75 |
| 300 | 0.9609(27) | 0.1005(35) | 0.34 |

Table 3.6: $f_0^{K\pi}(0)$ and decay constant $f_d$ determined for different cutoff of $m_\pi$ using $1 + f_2$ (3.15) with $f_d$ as the only free parameter.

it cannot be ignored in the mass extrapolation.

Thus even though global fit with only NLO term (3.15) seem to prefer $f_d \approx 95$ MeV, we cannot conclude this as a final value as it doesn't seem to account for the NNLO contributions. We can conclude that simul-fit is dependent on our choice of the unknown parameter $f_d$. Also we are unable to determine $f_d$ reliably when fit as a free parameter and this is not a good recipe for model independent results.

## 3.3 Polynomial Fits

The simul-fit ansatz in (3.1) is motivated by Ademello-Gatto theorem, and as described in the previous section this fit seems to be dependent on the choice of $f_d$ in $f_2$. For $f_2$, a simpler polynomial ansatz can be obtained by Taylor expanding the $f_2$ around the SU(3) symmetric limit ($m_K = m_\pi$) and ignoring the higher order terms.

### 3.3.1 1-NLO

Expanding $f_2$ around the SU(3) symmetric limit, and ignoring the higher order terms, we can approximate $f_0(0)$ as follows.

$$f_0(0) = 1 + C\left(\frac{(m_K^2 - m_\pi^2)^2}{m_K^2}\right) \tag{3.16}$$

We will refer to it as 1-NLO fit, with 1 referring to the value of $f_0(0)$ at SU(3) symmetric limit. Table 3.7 lists the $f_0^{K\pi}(0)$ and $f_0^{K\pi}(0)$ at SU(3) symmetric limit determined using 1-NLO fit. The $\chi^2$/dof of 1-NLO fit for $m_\pi$cutoff $< 700$ is

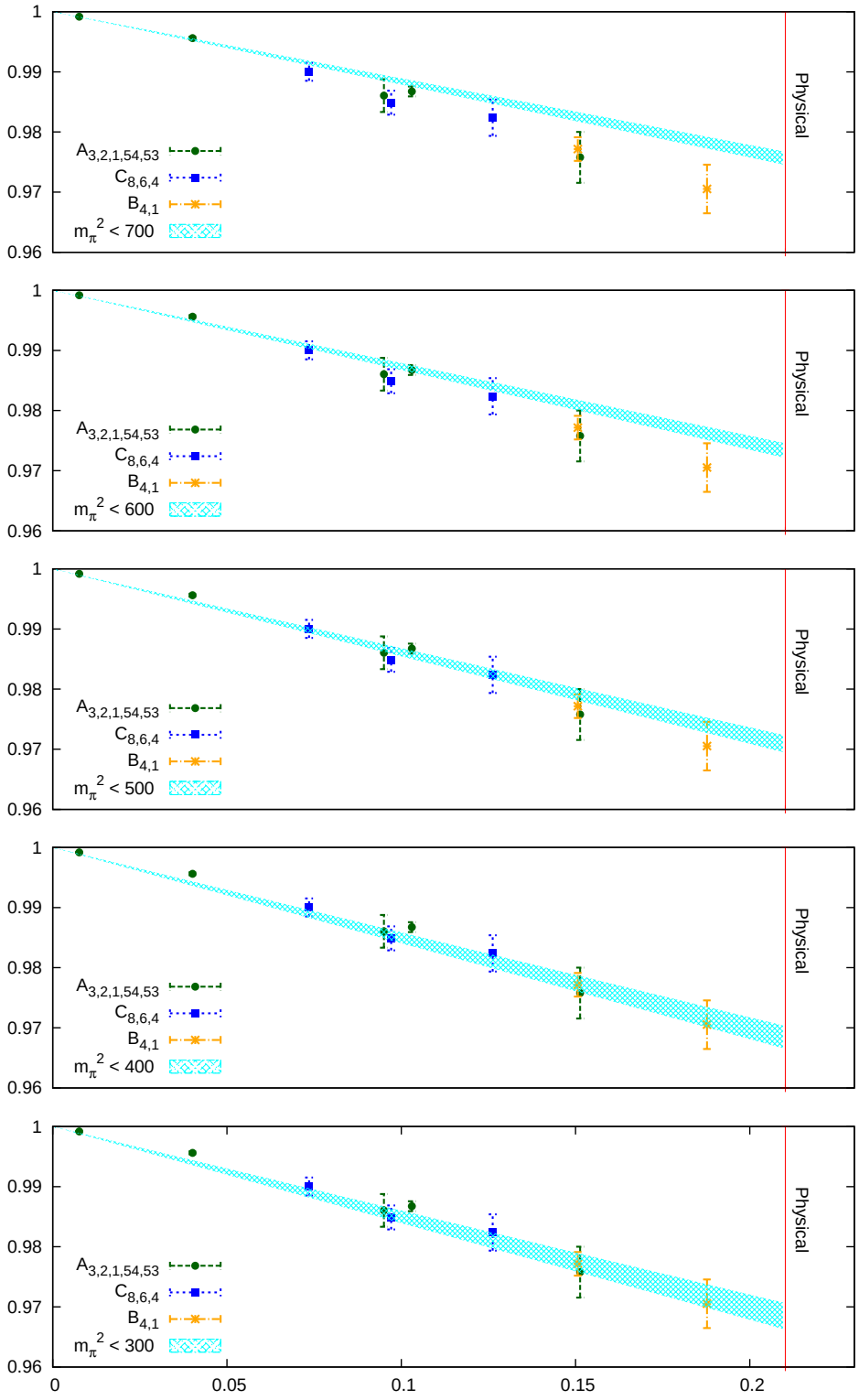


Figure 3.9: Plot showing $f_0^{K\pi}(q^2)$ determined using 1-NLO fit (3.16) as a function of $(m_K^2 - m_\pi^2)^2/m_K^2$ for different $m_\pi$ cutoffs.

| $m_\pi$ cutoff | $f_0(0)$ | $f_0^{SU(3)}(0)$ | $\chi^2$/dof |
|---|---|---|---|
| 700 | 0.9756(10) | 1 | 4.61 |
| 600 | 0.9733(12) | 1 | 2.18 |
| 500 | 0.9709(14) | 1 | 0.69 |
| 400 | 0.9684(19) | 1 | 0.13 |
| 300 | 0.9684(22) | 1 | 0.17 |

Table 3.7: $f_0^{K\pi}(0)$ and $f_0(0)$ at SU(3) symmetric limit determined for different cutoff of $m_\pi$ using 1-NLO fit (3.16).

4.61 and reduces to 0.17 as $m_\pi$ cutoff is reduced. The 1-NLO fit is a linear fit and $\chi^2/\text{dof} \gg 1$ simply points to existence of NNLO term and the presence of a dominant quadratic term in the Taylor expansion. This explains why $\chi^2$/dof decreases as the points closer to SU(3) symmetric limit ($m_\pi > 500$) are excluded from the fit. Fig. 3.9 shows how the linear 1-NLO fits individual data points and how the fit evolves as $m_\pi$ cutoff is applied. We can infer from the Fig. 3.9 that 1-NLO doesn't fit all the points for any $m_\pi$ cutoff and so cannot be used as a suitable ansatz for all data sets.

### 3.3.2 a-NLO

In 1-NLO fit ansatz, we can allow the value of $f_0^{K\pi}(0)$ at the SU(3) symmetric limit to be a free parameter instead of setting it to 1. Equation (3.17) corresponds to polynomial ansatz for the NLO term in simul-fit with $f_0^{K\pi}(0)$ at SU(3) symmetric limit as a free parameter. We will refer to it as a-NLO fit and $A$ in a-NLO fit should be consistent with 1 to ensure charge conservation.

$$f_0(0) = A + C\left(\frac{(m_K^2 - m_\pi^2)^2}{m_K^2}\right) \tag{3.17}$$

Table 3.8 lists the $f_0^{K\pi}(0)$ and $f_0^{K\pi}(0)$ at SU(3) symmetric limit determined using a-NLO fit. The $\chi^2/dof$ of a-NLO fit when all data set is included is 1.54 and reduces to 0.03 as $m_\pi$ cutoff is reduced. Interestingly, for $m_\pi$ cutoff $> 400$, the value of $f_0^{SU(3)}(0)$ produced by the fit is not consistent with 1, in violation of charge conservation. The deviation is small and likely a statistical effect or insufficient terms in our fit model at this level of precision. Fig. 3.9 shows how the linear a-NLO fits individual data points and how the fit evolves as $m_\pi$ cutoff

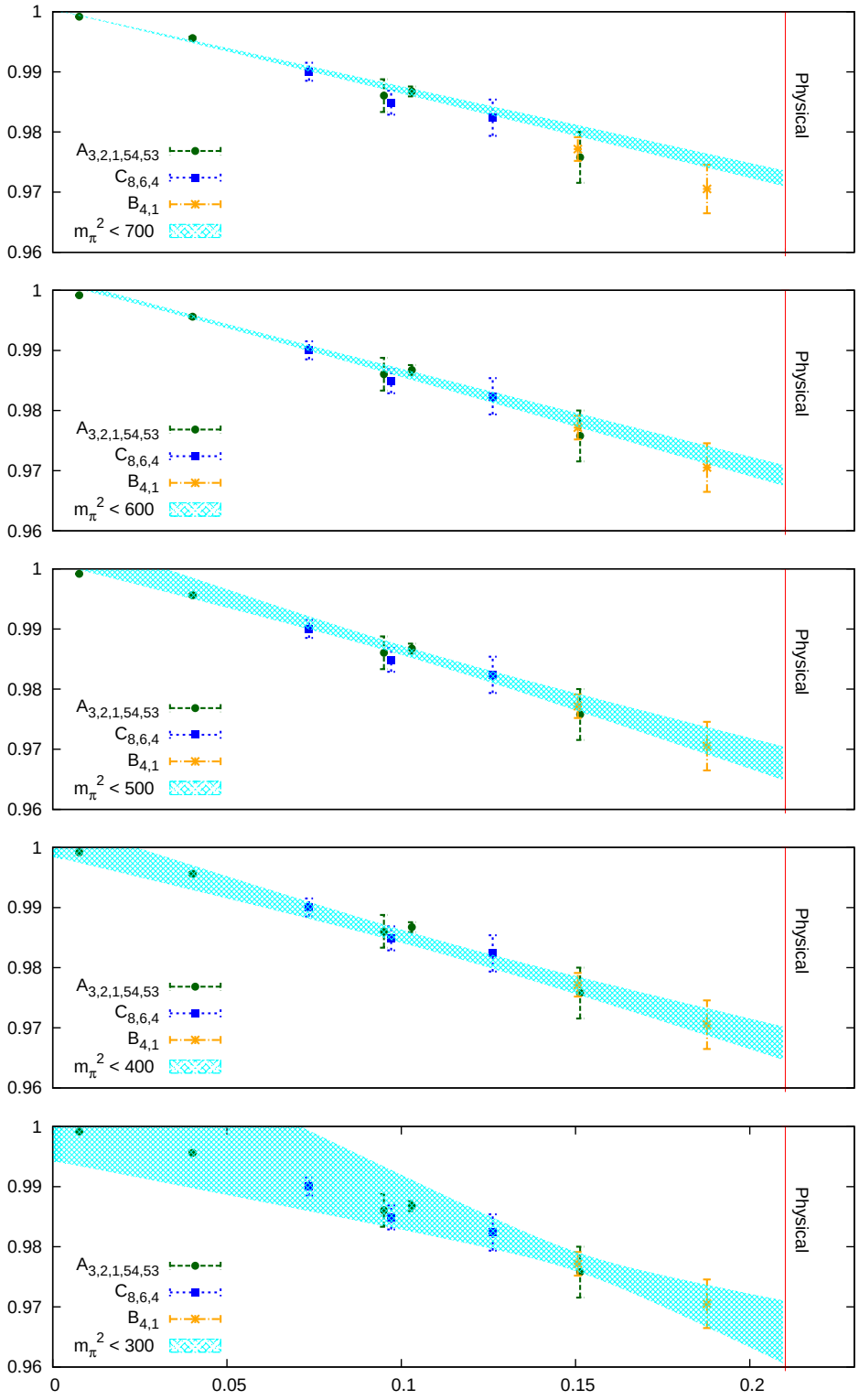


Figure 3.10: Plot showing $f_0^{K\pi}(q^2)$ determined using a-NLO fit (3.17) as a function of $(m_K^2 - m_\pi^2)^2/m_K^2$ for different $m_\pi$ cutoffs.

| $m_\pi\, cutoff$ | $f_0(0)$ | $f_0^{SU(3)}(0)$ | $\chi^2/dof$ |
|---|---|---|---|
| 700 | 0.9722(13) | 1.0004(1) | 1.54 |
| 600 | 0.9691(17) | 1.0018(5) | 0.51 |
| 500 | 0.9676(28) | 1.0037(27) | 0.52 |
| 400 | 0.9673(28) | 1.0015(30) | 0.11 |
| 300 | 0.9657(53) | 1.0070(127) | 0.03 |

Table 3.8: $f_0^{K\pi}(0)$ and $f_0(0)$ at SU(3) symmetric limit determined for different cutoff of $m_\pi$ using a-NLO fit (3.17).

is applied. Allowing $f_0^{SU(3)}(0)$ to be a free parameter inflates the error in the fit and fits almost all data points (especially with $m_\pi$ cutoff of 400 and 300).

Thus we can conclude that, for a $m_\pi$ cutoff of 400 MeV, a-NLO is a good approximation of $1 + f_2$ but also indicates the existence of NNLO terms. The important thing to note is that this fit ansatz is independent of $f_d$. If the inconsistent fits are discarded ($m_\pi$ cutoff $> 400$) we can expect $f_0^{K\pi}(0)$ value to lie within the range 0.9657 to 0.9673. This value is greater than that from simul-fit (130MeV) and so we can expect the polynomial fit ansatz (1-NLO and a-NLO) to prefer a value larger than 130 MeV for $f_d$.

| $m_\pi\, cutoff$ | $f_0(0)$ | $f_0^{SU(3)}(0)$ | $\chi^2/dof$ |
|---|---|---|---|
| 700 | 0.9668(21) | 0.99996(15) | 0.16 |
| 600 | 0.9668(22) | 0.99994(13) | 0.18 |
| 500 | 0.9668(28) | 0.99977(355) | 0.21 |
| 400 | 0.9676(30) | 1.00247(389) | 0.13 |
| 300 | na. | na. | na. |

Table 3.9: $f_0^{K\pi}(0)$ and $f_0(0)$ at SU(3) symmetric limit determined for different cutoff of $m_\pi$ using a-NNLO fit (3.18).

### 3.3.3 1-NNLO and a-NNLO

From a-NLO and 1-NLO fits, we found that the polynomial ansatz is a good approximation for the simul fit and need to add NNLO term to account for the curvature in the data. So we can readily add the NNLO term as that in (3.9) to fits (3.17) and (3.16) as shown below.

$$f_0(0) = A + \frac{\left(m_K^2 - m_\pi^2\right)^2}{m_K^2}\left(C + B\left(m_K^2 + m_\pi^2\right)\right) \tag{3.18}$$

$$f_0(0) = 1 + \frac{\left(m_K^2 - m_\pi^2\right)^2}{m_K^2}\left(C + B\left(m_K^2 + m_\pi^2\right)\right) \tag{3.19}$$

| $m_\pi\, cutoff$ | $f_0(0)$ | $f_0^{SU(3)}(0)$ | $\chi^2/dof$ |
|---|---|---|---|
| 700 | 0.9671(17) | 1 | 0.14 |
| 600 | 0.9668(20) | 1 | 0.15 |
| 500 | 0.9668(30) | 1 | 0.15 |
| 400 | 0.9676(30) | 1 | 0.13 |
| 300 | 0.9664(43) | 1 | 0.04 |

Table 3.10: $f_0^{K\pi}(0)$ determined for different cutoff of $m_\pi$ using 1-NNLO fit (3.19).

These fits will be referred to as a-NNLO and 1-NNLO fit respectively. The NNLO term is similar to the NNLO term of simul-fit. Tables 3.9 and 3.10 lists the $f_0^{K\pi}(0)$ and $f_0^{K\pi}(0)$ at SU(3) symmetric limit determined using fits a-NNLO and 1-NNLO respectively. For both a-NNLO and 1-NNLO, not only we get lower $\chi^2/dof$ when compared to simul-fit, but also the variance for different $m_\pi$ cutoff is negligible. For a-NNLO fit, when $f_0^{SU(3)}(0)$ is allowed to be a free parameter, its value is consistent with 1, as required by charge conservation.

Fig. 3.12 shows how the 1-NNLO fits individual data points and how the fit evolves as $m_\pi$ cutoff is applied. All the fits, fit all the data values and we can observe similar features for a-NNLO fit (Fig. 3.11). This also doesn't suffer from dependence on $f_d$. From 1-NNLO and a-NNLO, we can expect $f_0^{K\pi}(0)$ value to lie within the range 0.9664 to 0.9676.

Fig. 3.13 shows mass extrapolation of $f_0^{K\pi}(0)$ using different fit ansatz. We can conclude that 1-NNLO fits the form-factor data for all ensembles when compared to simul-fit, a-NLO and 1-NLO fits. The result from 1-NNLO fit is taken as the central value for above reasons. Now we need to estimate the systematic errors associated with the model dependence of our mass extrapolation, finite volume effects and Lattice artifacts.

## 3.4 Error budget

In this section we estimate the systematic uncertainties associated with Lattice artifacts , finite volume effects and model dependence of mass extrapolation in our error budget.

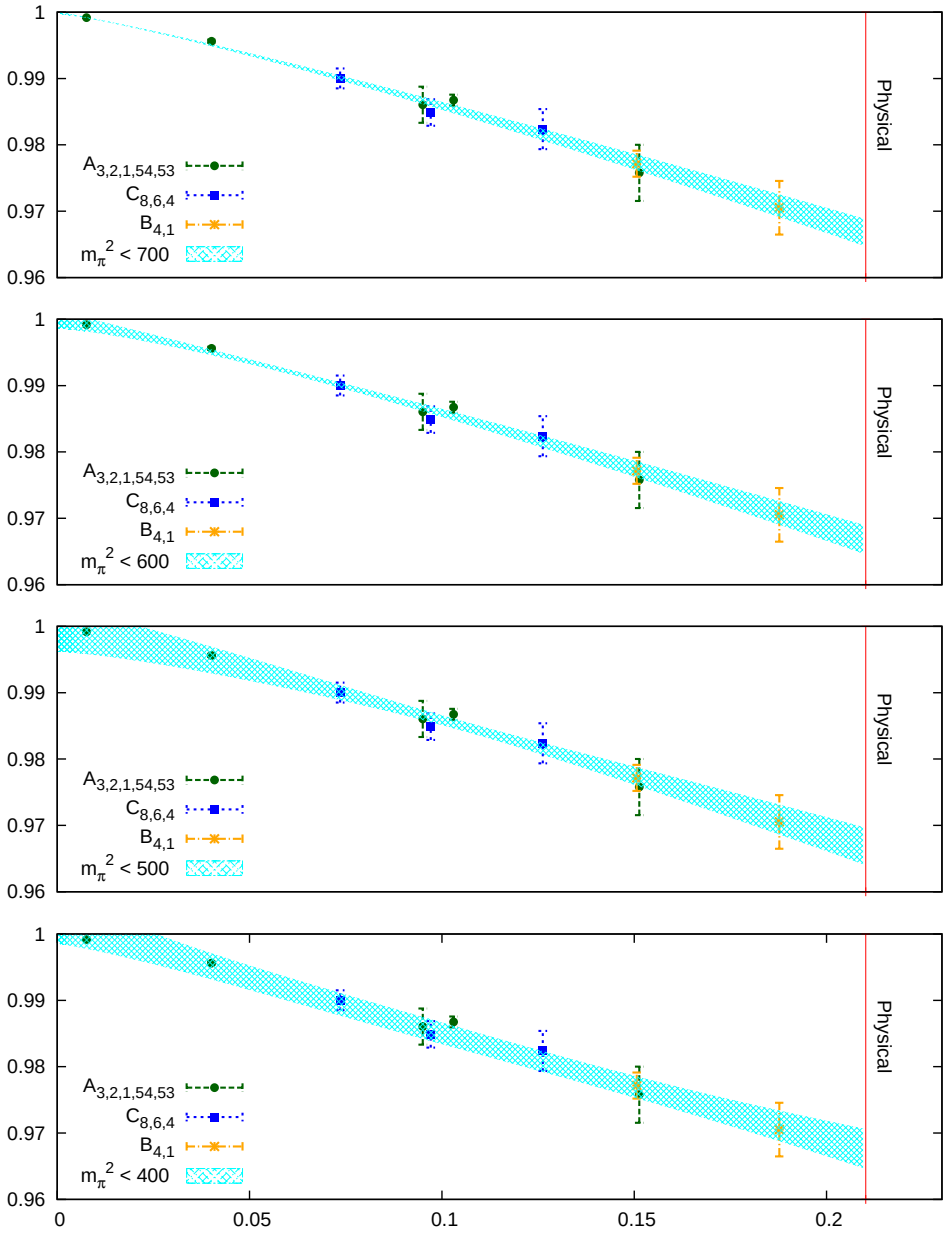


Figure 3.11: Plot showing $f_0^{K\pi}(q^2)$ determined using a-NNLO fit (3.18) as a function of $(m_K^2 - m_\pi^2)^2/m_K^2$ for different $m_\pi$ cutoffs.

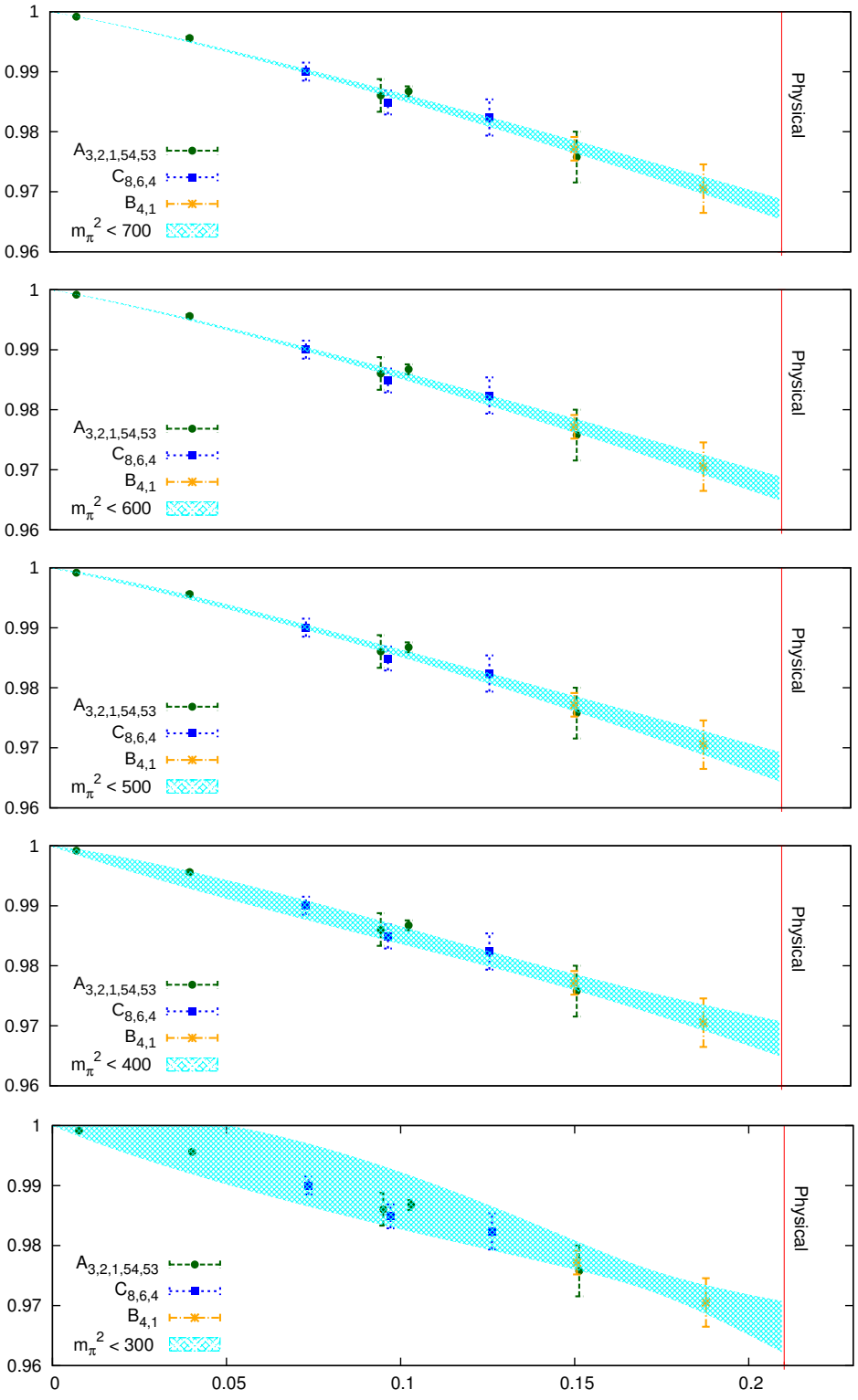


Figure 3.12: Plot showing $f_0^{K\pi}(q^2)$ determined using 1-NNLO fit (3.19) as a function of $(m_K^2 - m_\pi^2)^2/m_K^2$ for different $m_\pi$ cutoffs.

The ratios $R_1$ and $R_2$ in (2.5) are constructed such that $f_+^{K\pi}(0)|_{m_s=m_l} = 1$ and holds exactly even in a finite volume and for a finite lattice cut-off. So we expect finite-volume and cut-off effects to be symmetry-suppressed. Domain wall fermions are $O(a)$-improved and on the deviation of the form factor from one, we expect $O\left((a\Lambda_{\mathrm{QCD}})^2\right) \approx 5\%$ and $\approx 2\%$ cut-off effects on the Coarse (32Coarse) and finest ensemble (32Fine) respectively (assuming $\Lambda_{\mathrm{QCD}} \approx 300\,\mathrm{MeV}$). The Fig. 3.13 validates our findings as the data points for $m_\pi = 248\,\mathrm{MeV}$ ($\mathrm{B}_4$) and $m_\pi = 334\,\mathrm{MeV}$ ($\mathrm{A}_5^4$), with $a = 0.14\,\mathrm{fm}$ and $a = 0.11\,\mathrm{fm}$, respectively, lie on top of each other. Similarly, the $m_\pi = 334\,\mathrm{MeV}$ ($\mathrm{A}_5^3$) and $m_\pi = 349\,\mathrm{MeV}$ ($\mathrm{C}_6$) simulation points for $a = 0.11\,\mathrm{fm}$ and $a = 0.09\,\mathrm{fm}$, respectively, are in complete agreement. we can conclude that the cut-off effects are therefore absent at the current level of precision. The chiral effective theory [Ghorbani 11, Ghorbani 13] predicts finite

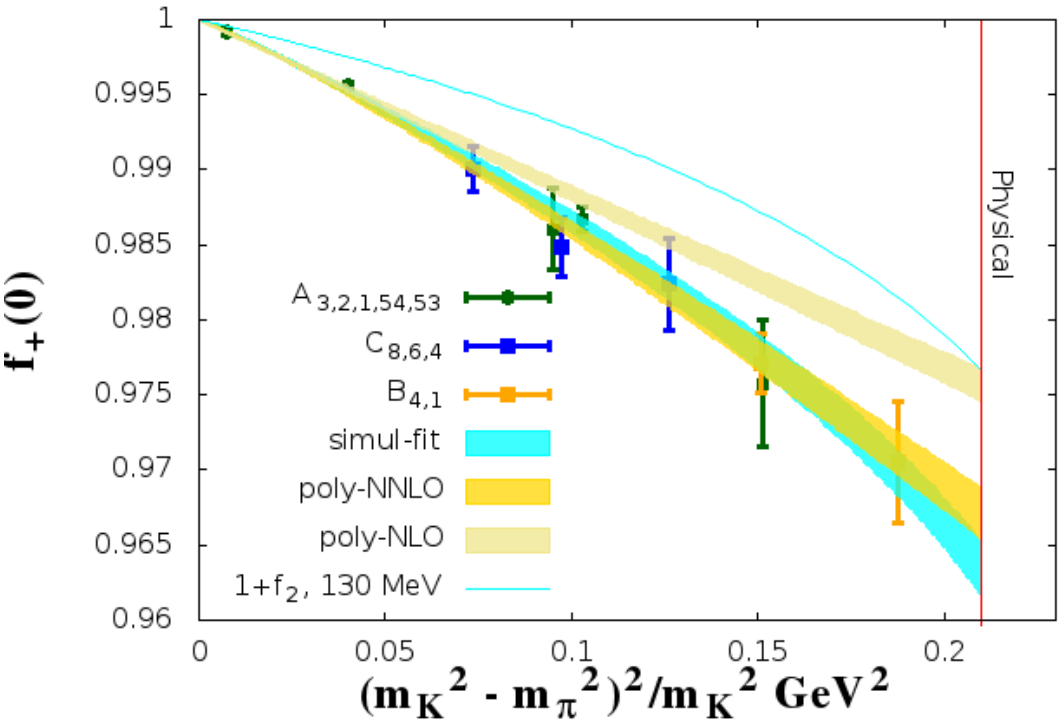


Figure 3.13: Plot showing mass extrapolation of $f_0^{K\pi}(0)$ using different fit ansatz and $f_0(0)$ from table 2.10. poly-NNLO and poly-NLO fit refers to 1-NNLO and 1-NLO fit with $m_\pi$ cutoff of 700 MeV.

volume effects are proportional to $e^{-m_\pi L}$ and suppressed exponentially. From table 2.3 we can observe that $m_\pi L$ has a minimum of value of 3.9. So we can conclude that the finite volume effects to be less than 2%.

Both the uncertainty due to finite volume effects and finite lattice cut-off affects only $1 - f_+^{K\pi}(0)$ which is negligible when compared to the statistical error for $f_+^{K\pi}(0)$ . In this section we therefore assume that both lattice artifacts and finite-volume effects are below the statistical accuracy of the results. Following the above discussion we estimate finite volume errors to be of order 2% and cutoff effects to be of order 5% on $1 - f_+^{K\pi}(0)$. Error in the lattice spacing shows the uncertainty in the scale of each ensemble and this is folded into the error analysis, so that the statistical error includes this uncertainty.

$$\begin{aligned} a^{-1}(\text{32Fine}) &= 2.310(37)(17)(9)\ \text{GeV} \\ a^{-1}(\text{24Coarse}) &= 1.747(31)(24)(4)\ \text{GeV} \\ a^{-1}(\text{32Coarse}) &= 1.3709(84)(56)(3)\ \text{GeV} \end{aligned} \tag{3.20}$$

The mass extrapolation for our final result is based on 1-NNLO fit but simul-fit appears to be an adequate alternative even though it is found to be dependent on $f_d$. When varying the input $f_d$ in simul-fit, the value of $\chi^2$/d.o.f. has a minimum around $f_d = 123\,\text{MeV}$. For this value of $f_d$ we find $f_+^{K\pi}(0) = 0.9632(16)$. We take the difference in central value between this simul-fit result and 1-NNLO as the residual model-dependence. After these considerations our final result is,

$$\begin{aligned} f_+^{K\pi}(0) &= 0.9671(17)_{\text{stat}}(^{+\ 0}_{-39})_{\text{model}}(7)_{\text{FSE}}(17)_{\text{cutoff}} \\ &\qquad\qquad 0.2\% \quad 0.4\% \quad 0.07\% \quad 0.2\% \\ &= 0.9671(17)(^{+18}_{-46})\,, \end{aligned} \tag{3.21}$$

where all systematic errors are added in quadrature. The previous result [Boyle 10] was based on 24Coarse ensemble with simul-fit where the main source of error was found to be $f_2$-term that determines the curvature as one moves away from the $SU(3)$-symmetric limit. Data sets with $m_\pi > 333$, mass extrapolation was performed by varying the value of the decay constant entering $f_2$. This value is then used to quantify the error due to mass extrapolation. Their result was $0.9599(34)(^{+31}_{-43})(14)$ and is fully compatible with the simul-fit applied to the

enlarged data set. With the new 1-NNLO ansatz, the mass extrapolation is independent of choice of decay constant.

The first applications of our result are predicting the CKM-matrix element $|V_{us}|$ and testing the unitarity of the CKM-matrix which is a crucial Standard Model test. In [Antonelli 10] the experimental data for $K \to \pi$ semi-leptonic decays was analysed. Their result $|V_{us} f_+^{K\pi}(0)| = 0.2163(5)$ combined with our result for $f_+^{K\pi}(0)$ gives

$$|V_{us}| = 0.2237(^{+13}_{-\ 8})\,. \tag{3.22}$$

Together with the result $|V_{ud}| = 0.97425(22)$ [Hardy 09] from super-allowed nuclear $\beta$-decay and $|V_{ub}| = 4.15(49) \cdot 10^{-3}$ [Beringer 12] we then confirm CKM-unitarity at the sub per mille level,

$$|V_{ud}|^2 + |V_{us}|^2 + |V_{ub}|^2 - 1 = -0.0008(^{+7}_{-6})\,. \tag{3.23}$$

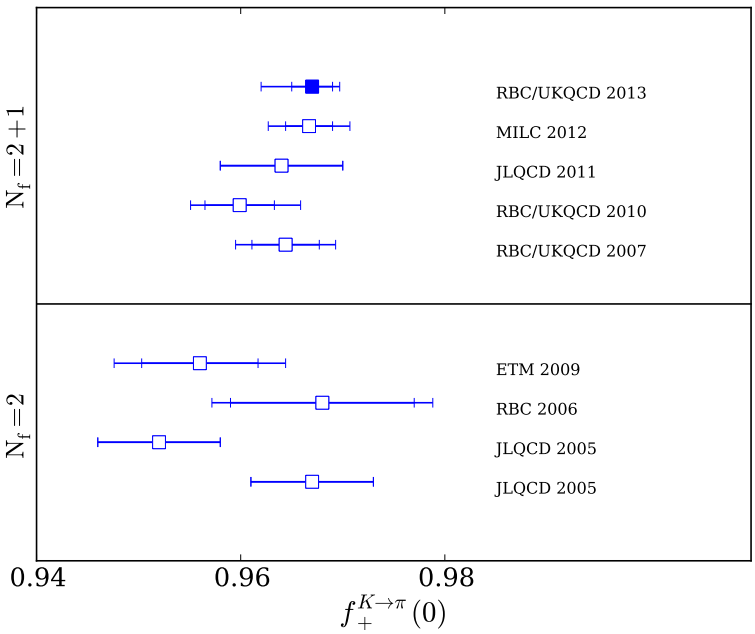


Figure 3.14: Comparison of recent Lattice results for $f_0^{K\pi}(0)$. Solid blue line (RBC-UKQCD 13) denotes the result calculated in this thesis.

## 3.5 Conclusion

We have studied the Kaon semi-leptonic decay form factor in three-flavor lattice QCD with simulations in large lattice volumes , three values of the lattice spacing and pion masses in the range from 678 to 171 MeV. All these allows us to do a the detailed study of systematic effects. We have studied the dependence of the ansatz on momentum transfer and quark masses. In performing the chiral extrapolation this study has identified a preferred functional form which was not used previously. After the extrapolation to the physical point we obtain the form factor with a statistical precision of 2 per mille and estimated $^{+2}_{-5}$ per mille systematic errors. The prediction for the form factor, $f_+^{K\pi}(0) = 0.9671(17)(^{+18}_{-46})$ has an overall uncertainty of $^{+0.3}_{-0.5}\%$, where statistical and systematic uncertainties have been added in quadrature.

Future work in the calculation should supplement the data set by simulations performed directly at the physical point. These additional data will allow us to reduce the dominant systematic uncertainty, that due to the extrapolation in the quark mass to the physical point.

In Fig. 3.14 we compare the result discussed in this thesis for $f_+(0)$ with other Lattice determinations. This result has bee published in JHEP [Boyle 13a] and presented at the recent Lattice conference at Mainz [Juettner 13]. Recent results of $f_+(0)$ determined at physical quark masses using $N_f = 2 + 1 + 1$ HISQ fermions [Gamiz 13] and the update to this thesis [Juettner 13] are in good agreement with the result in this thesis. An immediate phenomenological application of our result is the test of first-row CKM-matrix unitarity in the Standard Model which we are able to confirm at the sub per mille level.

# Chapter 4

# Clover Action for Blue Gene-Q and Iterative solvers for DWF

## 4.1 Introduction

In Lattice measurement of physical quantities, the simulated unphysical quark masses require mass extrapolation, as discussed in Chap. 3. With almost 50 million core-hours used for $K_{l3}$ calculation(ref. table 2.2) using unphysical quark masses, the major challenge in simulating physical quarks is the computational complexity of these simulations. This chapter describes the efforts made to reduce the computation cost by optimising clover fermion action for a new HPC architecture and testing different iterative solvers for DWF.

In Lattice QCD, the clover action is widely used, as it is cheaper than the chiral fermion action(DWF) discussed earlier. The clover term in (1.32) with the right coefficients gives $\mathcal{O}(a)$ improvement for on-shell quantities. Lattice QCD simulations with dynamical fermions usually involves hundreds of thousands of inversions in a serial dependent, importance sampling of QCD path integral. The inverter performance is critical for any good optimisation of Lattice QCD simulation. The inverter of this sparse matrix involves using an iterative solver that has repeated application of the clover operator. This chapter describes porting and optimisation of clover inverter to Blue Gene-Q architecture using the BAGEL compiler [Boyle 09].

## 4.2 Blue Gene-Q

Blue Gene-Q is based on the 64-bit Power-PC A2 processor core and with peak performance of 209 tera flops per rack of 1024 nodes (each node containing 16 compute and one OS core). It is the successor of Blue Gene-P architecture. Blue Gene-Q has quad floating point unit which can handle four floating point multiply-add operations, in parallel. Each node has 16GB of memory, the on-chip memory hierarchy consists of 16 KB L1 data and instruction cache and 4KB of L1 prefetch engine and 32 MB of L2 cache. DMA (Direct Memory Access) handles reading and writing messages across the network torus. Each core supports four threads and 64 threads across all cores share memory in a node. For complete details of the architecture, refer to [Haring 12] and [Gilge 13].

The Message Passing Interface (MPI) and OpenMP are supported and XL compilers provide some support for automatic vectorisation. As with most recent HPC architecture, the performance is limited by network and memory bandwidth. Symmetric multi-threading of four hardware threads per core (64 per node) helps in hiding the memory latency. The 5D interconnect torus and DMA provides a peak bandwidth of 40GB/s and overlapping communication with computations usually helps in hiding the network latency. The L1 prefetch engine, that was developed by scientists in University of Edinburgh and Columbia University, supports many prefetch patterns. The L2 cache supports atomic operations and the message-unit supports MPI Collective and All-to-All operations in hardware. For a detailed discussion of optimising Lattice actions for Blue Gene-Q architecture, refer to [Boyle 12a].

## 4.3 BAGEL and BFM

BAGEL is a QCD domain specific library developed by University of Edinburgh [Boyle 09]. It generates optimised assembly language instructions for target architectures including QCDOC, Blue Gene-P and Q machines. BAGEL achieves 20-50 % efficiency by better management of registers, SIMD operations, memory prefetching and instruction pipe-lining. For Blue Gene-Q, BAGEL uses one MPI process and 64 threads per node to efficiently use the shared memory and avoid unnecessary MPI packets for communication within the node. Also it uses IBM's System Programming Interface (SPI) library to communicate using

DMA and synchronise threads. Where possible, the compiler generates SIMD (QPX) instructions that efficiently use the quad floating unit.

BAGEL Fermion Matrix (BFM) library builds on top of BAGEL to provide QCD specific functionality. Currently the library supports solutions to QCD actions Wilson, Wilson twisted mass, Domain wall and Overlap. It supports iterative solvers like Conjugate Gradient (CG), Multi-shift CG in single, double and mixed precisions. As a part of this thesis, BFM was modified to support clover fermion action and new iterative solvers: MCR, GCR, OrthoMin and Multi-shift MCR.

## 4.4 Clover and Wilson actions

Clover action can be built from the Wilson action as follows

$$
\begin{aligned}
S &= \sum_{xy} \bar{\phi}(x) M_{xy} \phi(y) \qquad (4.1)\\
M_{xy}^{\text{Wilson}} &= I - k\,\mathcal{D}\\
M_{xy}^{\text{clover}} &= A - k\,\mathcal{D}\\
A &= I - k\,\frac{C_{sw}}{2} \sum_{\mu<\nu} [\gamma_\mu, \gamma_\nu] \mathcal{F}_{\mu\nu}
\end{aligned}
$$

where $\mathcal{D}$ is Wilson-Dirac operator. For clover action, Wilson-Dirac operator $\mathcal{D}$ and clover term $A$ can be applied independently. This clover term $A$ is local and can be computed once and applied to all the iterations of an iterative solver. In general, for any action that is based on Wilson fermion action and if it can be written like (4.1), then an optimised implementation of $\mathcal{D}$ can be reused.

$A$ is hermitian as $[\gamma_\mu, \gamma_\nu]$ and $\mathcal{F}_{\mu\nu}$ are hermitian. The $\gamma$ matrices are of the form

$$
\gamma_3 = \begin{pmatrix} 0 & I_2 \\ I_2 & 0 \end{pmatrix} \quad \gamma_{k=0,1,2} = \begin{pmatrix} 0 & i\sigma_k \\ -i\sigma_k & 0 \end{pmatrix} \qquad (4.2)
$$

where $\sigma_k$ are the Pauli matrices. The algebra of $\gamma$ matrices leaves A having the following format at each site.

$$
A_{xyzt} = \begin{pmatrix} A_1^{6\times6} & 0 \\ 0 & A_2^{6\times6} \end{pmatrix} \qquad (4.3)
$$

with two $6 \times 6$ hermitian matrices $A_1$ and $A_2$. This leaves us with implementation of $A \times \phi$ to complete the clover action. In performing this matrix multiplication, $A_1$ and $A_2$ are represented in a compressed format. To save memory space, the diagonal elements are stored as real numbers and only the lower triangular elements are stored as complex numbers.

## 4.5 Optimisation

This section describes the optimisation performed in porting the clover action to Blue Gene-Q architecture. BAGEL provides a highly optimised version of Wilson-Dirac operator($\mathcal{D}$) [Boyle 12a]. For an iterative solver, $A$ is constructed once and then applied hundreds of thousands of times. Construction of clover matrix($A$) takes less than 1% of the total inverter time and optimising this kernel will result in no real speedup. For this work, the clover matrix $A$ is constructed using an external library like CHROMA [Edwards 05] or CPS [Boyle 05] and then imported to BAGEL. This leaves us with optimising only the clover apply kernel($A \times \phi$).

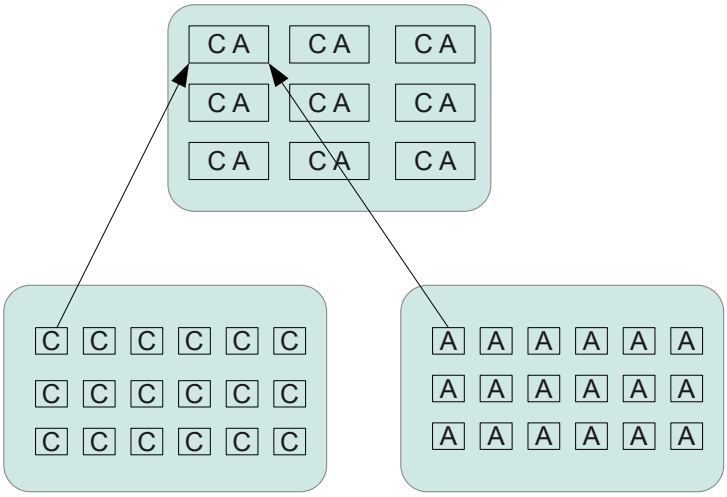


Figure 4.1: Plot showing data alignment for SIMDisation of data, where C and A are complex numbers from different logical volumes.

### 4.5.1 SIMD Optimisation

Blue Gene-Q has a vector length of four and this means for any SIMD optimisation, data required for four parallel instruction should be aligned consequently in memory. BAGEL compiler supports aligning data for different vector lengths. The compiler constructs logical SIMD volumes based on the vector length and stores the data from each of the logical volumes consequently in memory.

Clover matrix $A$ has the following format, with the right most index the fastest index.

```
A[L_x][L_y][L_z][L_t][M];
M :
   real diag[2][6];
   complex offdiag[2][15];
```

For complex number, the SIMD vector length of two is sufficient. Subdividing the volume to two logical volumes, $A$ is stored in the below format.

```
A[L_x][L_y][L_z][L_t/2][M][2]
M :
   real diag[2][6];
   complex offdiag[2][15];
```

Fig. 4.1 shows the SIMDisation of data for 2 logical nodes. With this new data layout, the QPX floating point unit can be efficiently used to increase floating point throughput. The key part is that by operating on two or more logical nodes in a data parallel fashion, one can always generate independent operations in different SIMD lines. This guarantees efficient SIMD operations and generalises to arbitrary width. A similar approach was used in the connection machine to operate on multiple memory banks and there the logical nodes were called virtual nodes.

### 4.5.2 Memory Optimisation

The application of clover matrix $A$ to a fermion vector requires efficient usage of cache and registers. This kernel requires reduction operations and using registers for all reduction variables will avoid writing to L1 cache which is write through.

With 32 registers available, it will be easier to load half-spinors into register and compute the results. It is important to note that all registers cannot be used as some are reserved for memory pointers. The data access pattern is sequential and the hardware cache is well optimised for sequential access. The logic can be summarised in Algo. 1.

**Data**: Lattice Fermion $\psi[V][N_s \times N_c]$, clover matrix $A[V][M]$
**Result**: Lattice Fermion $\chi[V][N_s \times N_c]$
Initialisation:
**for** *each site in V* **do**
  **for** *each half spinor* **do**
    Load $REG^6_\psi = \psi[site][N_s \times N_c]$
    Load $REG^6_\chi = \chi[site][N_s \times N_c]$
    Load $REG^6_A = A[site][M : diag]$
    compute $REG_\chi = REG_\psi \cdot REG_A$
    Load $REG^{15}_A = A[site][M : offdiag]$
    compute $REG_\chi \mathrel{+}= REG_\psi \cdot REG_A$
    store $\chi[site][N_s \times N_c] = REG_\chi$
  **end**
**end**

**Algorithm 1:** Function to apply clover matrix($A$). REG refers to registers and the super-script refers to number of registers used.

The above logic uses 27 registers, 6 each for $\chi$ and $\psi$ and 15 registers for storing the clover matrix($A$). Using fewer registers leads to serialisation of instructions due to dependencies. This is evident from the assembly instructions created by the BAGEL compiler.

For threading, 4 threads are used per core and 64 threads per node. With the spinors and clover matrix stored in shared memory, each thread is allocated list of sites using static scheduling. Complex scheduling strategies are not required as threads do the same amount of work. In case of multiple nodes, MPI is used for collective operations. This part of the kernel that implements application of clover matrix($A$) doesn't involve any massive communication like the Wilson-Dirac operator($\mathcal{D}$).

### 4.5.3 Instruction pipe-lining

Instruction pipe-lining plays a important role in increasing the throughput of instructions and hiding the memory latency. This is essential for achieving good efficiency with modern hardware architectures. BAGEL compiler constructs two pipelines using the greedy algorithm. Any dependencies for instructions are identified and are reordered accordingly. The planned schedule is referred to as execution map and acts as a abstract assembler. The instructions in execution map are then translated to hardware specific assembly instructions.

Listing 4.1: Execution map generated by BAGEL for Clover apply ($A$)

```
pipeline1     pipeline2
qvfxmul       qvlfsx
qvfxmul       qvlfsx
qvfxmul       qvlfsx
qvfxmul       addi
qvfxmul       la
qvfxmul         -
  -             -
  -             -
qvfxxnpmadd     -
qvfxxnpmadd     -
qvfxxnpmadd   qvlfsx
qvfxxnpmadd   qvlfsx
qvfxxnpmadd   qvlfsx
qvfxxnpmadd   qvlfsx
  -           qvlfsx
  -           qvlfsx
qvfxmadd      qvlfsx
qvfxmadd      qvlfsx
qvfxmadd      qvlfsx
qvfxmadd      qvlfsx
qvfxmadd      qvlfsx
  -           qvlfsx
  -           qvlfsx
qvfxmadd      qvlfsx
qvfxxcpnmadd  qvlfsx
```

```
qvfxxnpmadd      -
qvfxxnpmadd    addi
```

For clover apply($A$) as described in Algo. 1, BAGEL builds a execution map as shown in listing 4.1. We can see that from the prefix that the BAGEL uses QPX instructions to efficiently use the quad floating unit. Further the the load instruction (qvlfsx) are pipe-lined with the multiply instructions (qvfxmul). As the instruction unit is kept busy, this increases instruction throughput and the latency associated with loading data to memory is hidden.

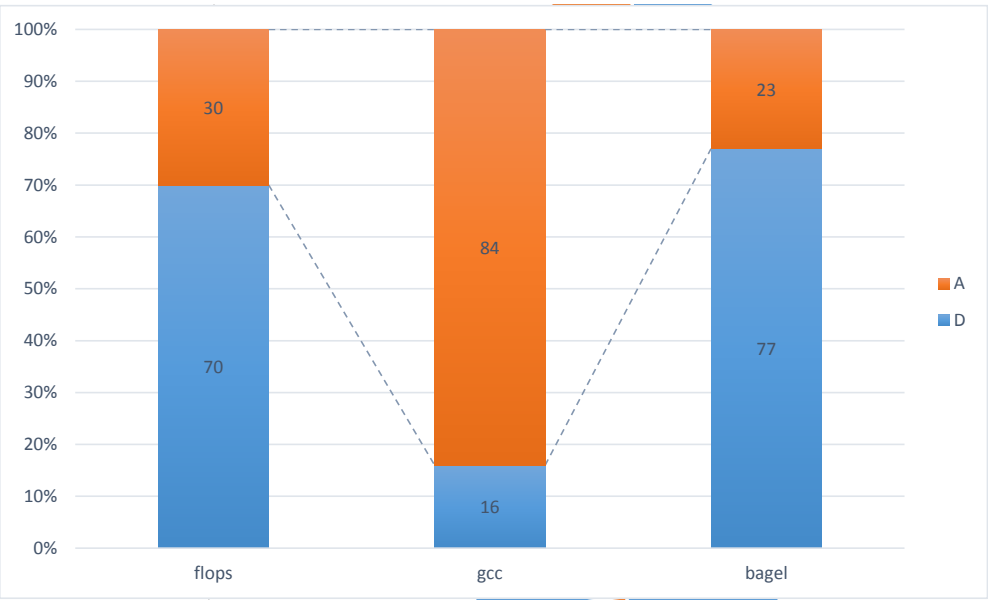


Figure 4.2: Plot comparing percentage of flops, percentage execution time using gcc and bagel compiler for clover apply($A$) and optimised Wilson-Dirac($\mathcal{D}$) kernels

## 4.6 Results

The optimisations discussed in previous section are applied to clover apply($A$) kernel. Fig. 4.2 compares the percentage of flops, percentage execution time using gcc and bagel compiler for clover apply($A$) and optimised Wilson-Dirac($\mathcal{D}$) kernels. Clover apply has 576 flops where as Wilson-Dirac has 1320 flops. With almost 30% of the total time spent on $A$, if both $\mathcal{D}$ and $A$ are 100% efficient, we can expect them to consume 70% and 30% of the execution time. Using a

gcc compiler for building $A$ and BAGEL optimised $\mathcal{D}$, result in an imbalance as cores spend 84% of time in $A$ as shown in Fig. 4.2. This shows the need for an optimised $A$ for the Blue Gene-Q architecture. Using BAGEL compiler and applying the optimisations, results in an optimised clover apply($A$) kernel, for which time spent is reduced $\approx 4$ times compared to the gcc version.

In order to achieve good efficiency, we need to experiment with the threads, MPI processes and memory. We have already established that to maximise the usage of shared memory and reduce unnecessary MPI packets, the application should run only with one MPI process per node. Each node supports 64 hardware threads and we can experiment with number of threads that gives optimal performance. Even though using more threads will result in better performance, it will also increase the synchronisation overhead. In this section, performance will be measured as the performance of the entire iterative Conjugate Gradient solver for clover fermion action that includes application of $\mathcal{D}$ and $A$ for each iteration. We will simply refer to it as Clover-CG.

Fig. 4.3 shows the performance of Clover-CG in GFlops per node, for increasing number of threads. The performance is measured on lattice volume of $32^4$, running on 128 nodes. From the plot we can infer that we have maximum efficiency of 18% for double precision and 23% for single precision when 64 threads are used. The speedup, when the threads are increased is not linear. If a linear speedup is achieved, we can expect a maximum performance of 100 and 124 GFlops per node for double and single precision respectively. We achieve only $\approx 37\%$ of the expected maximum performance due to the synchronisation overheads.

An important factor in performance for most high performance application is memory and network bandwidth. Optimally, the data should be available in cache so that memory latency is reduced. This means finding a optimal number of nodes to run the application so that the data can fit in the memory. Also care should be taken to ensure that there is enough data to keep the cores busy all the time.

Fig. 4.4 shows the performance in GFlops per node for Clover-CG in single precision for different volume and increasing number of nodes. One a single node, we couldn't run volumes larger than $32^4$ because of the limited memory available. On multiple nodes, we cannot run simulations for cases, where the

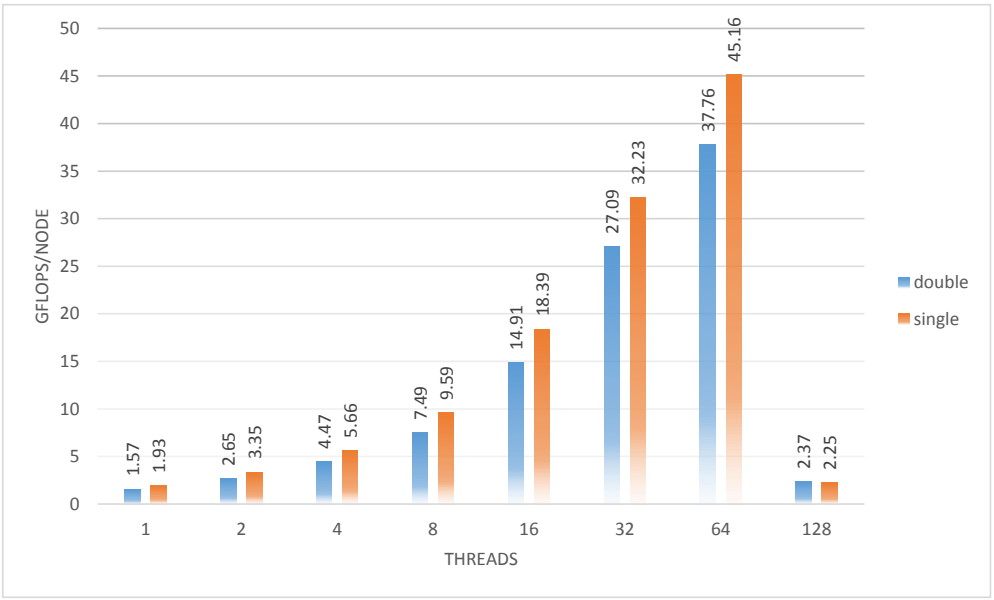


Figure 4.3: Plot showing performance in GFlops per node for Clover-CG when increasing number of threads are used per node. The performance is measured on lattice volume of $32^4$, running on 128 nodes.

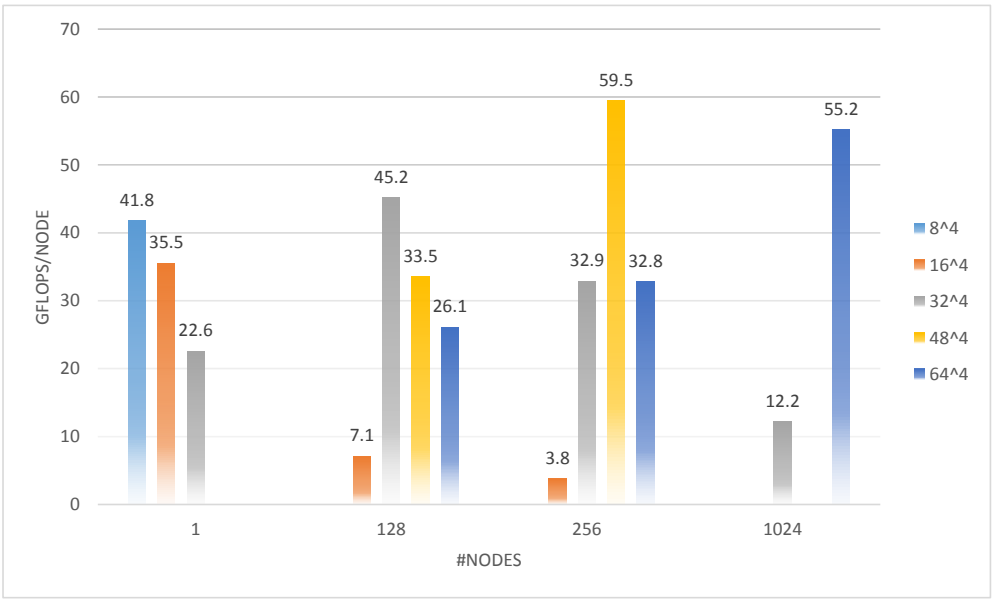


Figure 4.4: Plot showing performance in GFlops per node for a clover solver in single precision for different volume and increasing number of nodes.

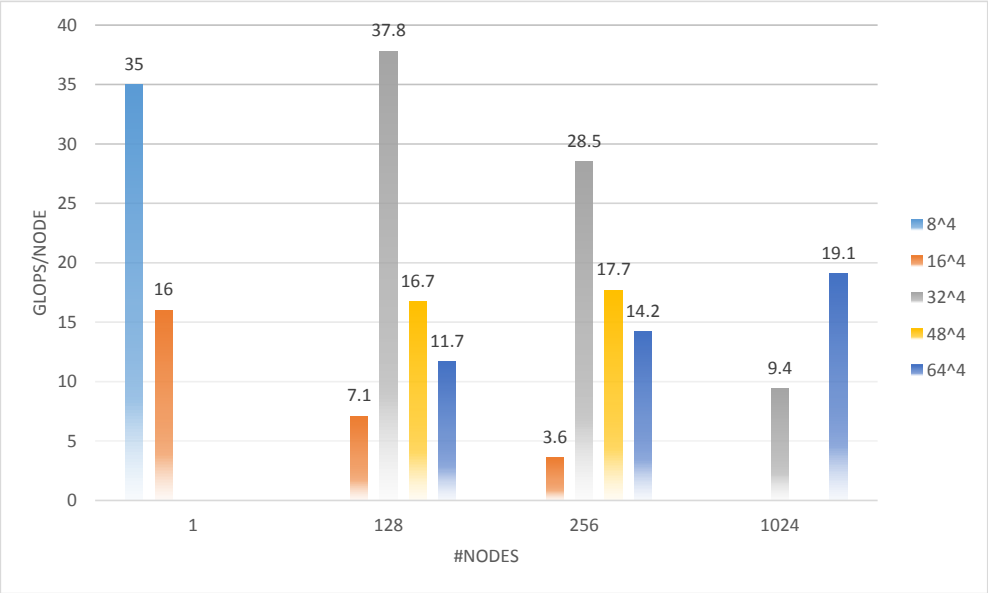


Figure 4.5: Plot showing performance in GFlops per node for a clover solver in double precision for different volume and increasing number of nodes.

local sub-volume is very small or has a odd dimension. We achieve a maximum performance of 59.5 GFlops per node when the lattice volume is $48^4$. This maximum performance corresponds to a efficiency of 29.1%. We can infer that for a single precision, using a local volume of $16 \times 8 \times 8 \times 16$ fits the memory well and there is enough data to keep all the cores busy. Similarly Fig. 4.5 shows the performance in GFlops per node for Clover-CG in double precision for different volume and increasing number of nodes. We achieve a maximum speedup of 37.8 GFlops per node when the lattice volume is $32^4$. In fact, for lattice volume $32^3 \times 48$, the performance slightly improves to 41 GFlops per node. This maximum performance corresponds to a efficiency of 20.2%. We can infer that for a double precision, using a local volume of $16 \times 8 \times 8 \times 12$, data fits the memory well and there is enough data to keep all the cores busy.

Both the single and double precision performance show strong local volume dependence. Fig. 4.6 shows the strong scaling of Clover-CG in double and single precision for increasing local lattice sub-volume, when run on a single and 128 nodes. The strong scaling shows strong dependence on local volume. For single precision, the performance improves as the local volume increase to $2^{14} = 16384$ and then reduces. Similar performance is seen for double precision,

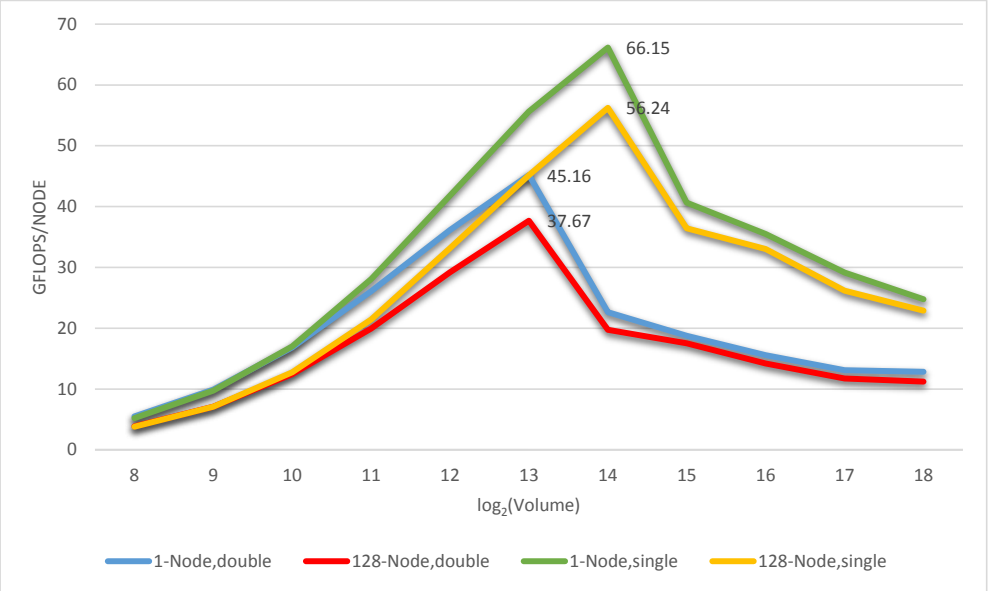


Figure 4.6: Plot showing strong scaling (GFlops per node) of the clover solver in double and single precision for increasing local sub-volume (for a single node) when run on a single and 128 nodes

with maximum performance achieved for a local volume of $2^{13} = 8192$ (as double precision takes twice as much memory as that for single precision). This is directly related to the size of the L2cache and maximum performance is achieved when the data fits the L2cache.

Also we can note that maximum performance of Clover-CG on 128 nodes using message passing slows down by 15% (single) or 16.5% (double) compared to single node. This is due to the additional overhead for passing message across nodes. This overhead doesn't increase as the number of nodes are increased to 1024 and shows very good scaling. Using more than 1024 nodes may increase overhead as they involve using more than one rack. This could not be tested due to non-availability of resources. Even though Clover-CG achieves maximum efficiency of 29.1% and shows good weak scaling, care should be taken to ensure the local sub-volume fits the cache for good throughput. This means running on less or more number of nodes according to the simulated lattice volume.

## 4.7 Iterative solvers for DWF

Computing the Quark propagators in a background gauge fields form the main part in any Lattice QCD simulation. This involves solving

$$(\mathcal{D} + m_q)\psi(x) = \eta(x) \tag{4.4}$$

where $\mathcal{D}$ is the Dirac matrix, $m_q$ is the quark mass, $\psi(x)$ and $\eta(x)$ are the solution and source field respectively. This large sparse linear system can be only solved using iterative methods (see eg. [Saad 03]). In a simulation, the above step of solving the linear system is repeated for different gauge configurations and different right hand sides. In case of Domain Wall fermion(DWF) action, the solution to the linear system becomes difficult as the Dirac matrix is large, indefinite and the eigen values are clustered around the origin. Also the matrix becomes ill-conditioned as the simulated quark masses($m_q$) gets closer to physical values and lattice spacing ($a$) gets smaller [Luscher 10]. The condition number $k(\mathcal{D})$ can be written as

$$k(\mathcal{D}) = (\frac{\alpha_{max}}{\alpha_{min}})^{\frac{1}{2}} \propto \frac{1}{ma} \tag{4.5}$$

Using a suitable solver and preconditioner is a topic of intense research. The following sections discuss iterative solvers namely Conjugate Gradient(CG), Generalised Conjugate residual(GCR) [Saad 86] and Modified Conjugate residual(MCR) [Chandra 77] for solving DWF.

**Data**: Matrix $A$, source vector $b$
**Result**: Solution vector $x$, $Ax = b$
Initialisation: $r_0 = b - Ax_0$; $p_0 = r_0$
**for** $j = 0, 1, 2, ...till\, convergence$ **do**
  $\alpha_j = \frac{(r_j, r_j)}{(Ap_j, p_j)}$
  $x_{j+1} = x_j + \alpha_j p_j$
  $r_{j+1} = r_j - \alpha_j A p_j$
  $\beta_j = \frac{(r_{j+1}, r_{j+1})}{(r_j, r_j)}$
  $p_{j+1} = r_{j+1} + \beta_j p_j$
**end**

**Algorithm 2:** Conjugate Gradient Algorithm

### 4.7.1 CG, MCR and GCR

The iterative methods described in this section are Krylov subspace methods based on projection methods(Petrov-Galerkin conditions). For solving a linear system $Ax = b$, the Krylov subspace is defined by

$$\mathcal{K}_m(A, r_0) \equiv span\{r_0, Ar_0, A^2 r_0, \ldots, A^{m-1} r_0\} \tag{4.6}$$

where $r_0 = b - Ax_0$. The approximate solution $x_m$ is obtained by searching in the subspace $x_0 + \mathcal{K}_m$ so that

$$b - Ax_m \perp \mathcal{L}_m \tag{4.7}$$

where $\mathcal{L}_m$ is also a subspace of dimension m.

**Data**: Matrix $A$, source vector $b$
**Result**: Solution vector $x$, $Ax = b$
Initialisation: $r_0 = b - Ax_0$; $p_0 = r_0$
**for** $j$=0, 1, 2, ...*till convergence* **do**
  $\alpha_j = \frac{(r_j, Ar_j)}{(Ap_j, p_j)}$
  $x_{j+1} = x_j + \alpha_j p_j$
  $r_{j+1} = r_j - \alpha_j A p_j$
  $\beta_j = \frac{(r_{j+1}, Ar_{j+1})}{(r_j, Ar_j)}$
  $p_{j+1} = r_{j+1} + \beta_j p_j$
**end**

**Algorithm 3:** Modified Conjugate Residual Algorithm

Conjugate Gradient (CG) is the most popular method for solving sparse symmetric, positive definite linear systems. CG uses orthogonal projection ($\mathcal{L}_m = \mathcal{K}_m$) on to Krylov subspace $\mathcal{K}_m(A, r^0)$. For symmetric, positive definite matrices, that are hermitian, MCR improves by constructing residual vectors that conjugate. For non-symmetric matrices, we can generalise by constructing $p_i$ as a linear combination of current and all previous $p_i$s. This general method is referred to as Generalised Conjugate Residual.

**Data**: Matrix $A$, source vector $b$
**Result**: Solution vector $x$, $Ax = b$
Initialisation: $r_0 = b - Ax_0$; $p_0 = r_0$
**for** $j = 0, 1, 2, ...till\, convergence$ **do**
  $\alpha_j = \frac{(r_j, Ap_j)}{(Ap_j, Ap_j)}$
  $x_{j+1} = x_j + \alpha_j p_j$
  $r_{j+1} = r_j - \alpha_j Ap_j$
  **for** $i = 0, 1, 2, ...j$ **do**
    $\beta_{ij} = \frac{(Ar_{j+1}, Ap_{i+1})}{(Ap_i, Ap_i)}$
  **end**
  $p_{j+1} = r_{j+1} + \sum_{i=0}^{j} \beta_{ij} p_i$
**end**

**Algorithm 4:** Generalised Conjugate Residual Algorithm

The exact steps of the CG, MCR and GCR algorithm are shown in Algo. 2, Algo. 3 and Algo. 4 respectively. For CG, $p_i$s are A-orthogonal, whereas for MCR, $Ap_i$s are orthogonal or simply $p_i$s are $A^\dagger A$-orthogonal.

CG and MCR are very similar, but MCR requires storage for one more vector and requires more operations than CG. GCR algorithm requires us to store all previous $p_i$s ($Ap_i$s) and this is practically not possible. The number of previous $p_i$s that are stored are restricted to a lesser number (m). We can either restart after m iterations or truncate the number of $p_i$s stored to the latest m entries. The former is referred to as GCR(m) and the latter as OrthoMin(m).

## 4.8 Results

In simulating Domain Wall Fermion, the fermion matrix is represented as $\mathcal{M}^\dagger\mathcal{M}$ as it is positive definite and hermitian. In case of GCR and OrthoMin, we can consider both $\mathcal{M}^\dagger\mathcal{M}$ and $\mathcal{M}$, to check if it works generally for non-symmetric matrices. Also for GCR and OrthoMin, careful study is required to balance the number of previous residuals to store and computation cost for better performance.

In this work, we use a variant of CG called CGNE [Freund 92], which solves $Ax = b$ by solving $AA^Ty = b$ ($x = A^Ty$). We will refer to it as CG for simplicity. GCR with fermion matrix $\mathcal{M}^\dagger\mathcal{M}$ and $\mathcal{M}$ will be referred to as GCR-MM and

GCR-M respectively. OrthoMin will also be referred to as O-MIN.

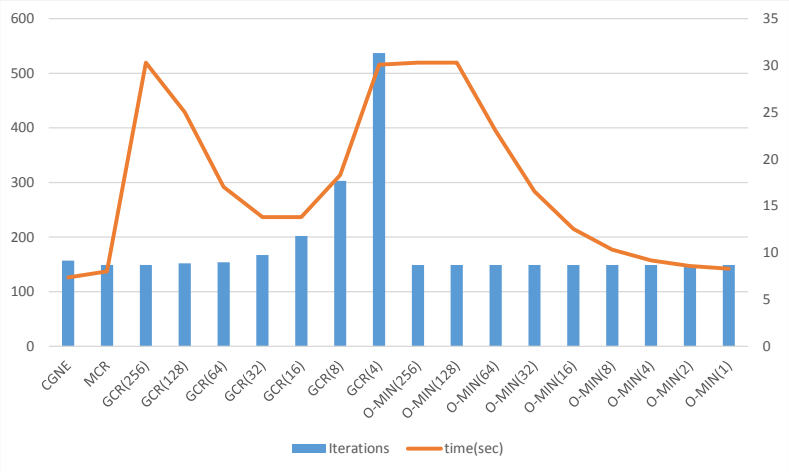


Figure 4.7: Plot showing number of iterations(left axis) and time taken (right axis) for DWF in a random gauge field with $L_s = 16$ using different solvers in solving $\mathcal{M}^\dagger\mathcal{M}\,\psi = \chi$.

The results described in this section uses gauge configuration with $N_f$= 2+1 dynamical flavors, generated from Iwasaki gauge action at $\beta$=2.13 ($a^{-1}$=1.73(4) GeV) and lattice volume of $16^3 \times 32$. All the iterative solvers discussed in this section uses $L_s$=16 and quark mass of 0.01, unless specified otherwise. The performance is measured on 128 nodes of Blue Gene-Q machine.

Fig. 4.7 shows the results for solving $\mathcal{M}^\dagger\mathcal{M}\,\psi = \chi$ using different solvers. CG and MCR and OrthoMin(1) are efficient when we compare both the number of iterations and the time to converge. For restarted GCR, the most efficient solver requires 16 $p_i$s to be stored before a restart and takes more than twice the time as that for CG. OrthoMin behaves exactly same as MCR and we can easily say MCR is equivalent to OrthoMin(1). Storing more residuals for OrthoMin doesn't make any difference as the number of iterations to converge and the residual at each iteration remain similar.

Fig. 4.8 shows the results for solving $\mathcal{M}\,\psi = \chi$ using GCR and OrthoMin solvers. CG and MCR results in this plot, still use $\mathcal{M}^\dagger\mathcal{M}$ and are added to the plot for easier comparison. As expected GCR and OrthoMin solves $\mathcal{M}$ efficiently as GCR(4) and OrthoMin(4) solves in almost half the time as that for CG and MCR. Using GCR and OrthoMin with $\mathcal{M}$, reduces the number of matrix operations by half, even though it increases the number of vectors stored and the number of

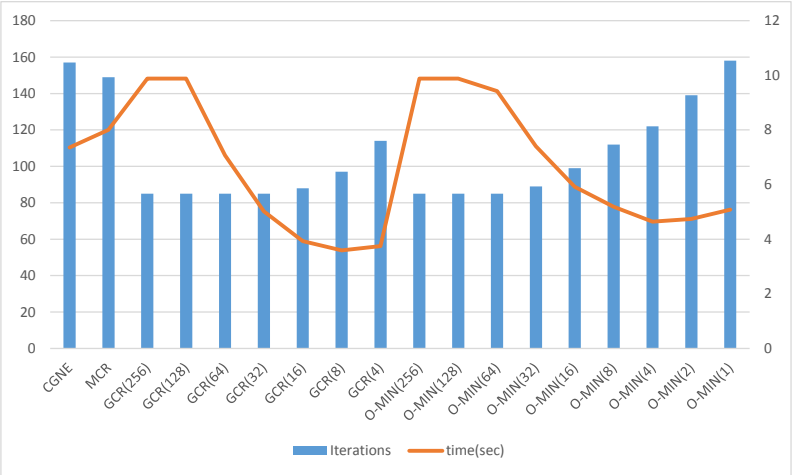


Figure 4.8: Plot showing number of iterations(left axis) and time taken (right axis) for DWF in a random gauge field with $L_s = 16$ using different solvers in solving $M\,\psi = \chi$. CG and MCR solving $\mathcal{M}^\dagger\mathcal{M}\,\psi = \chi$, are added for easier comparison.

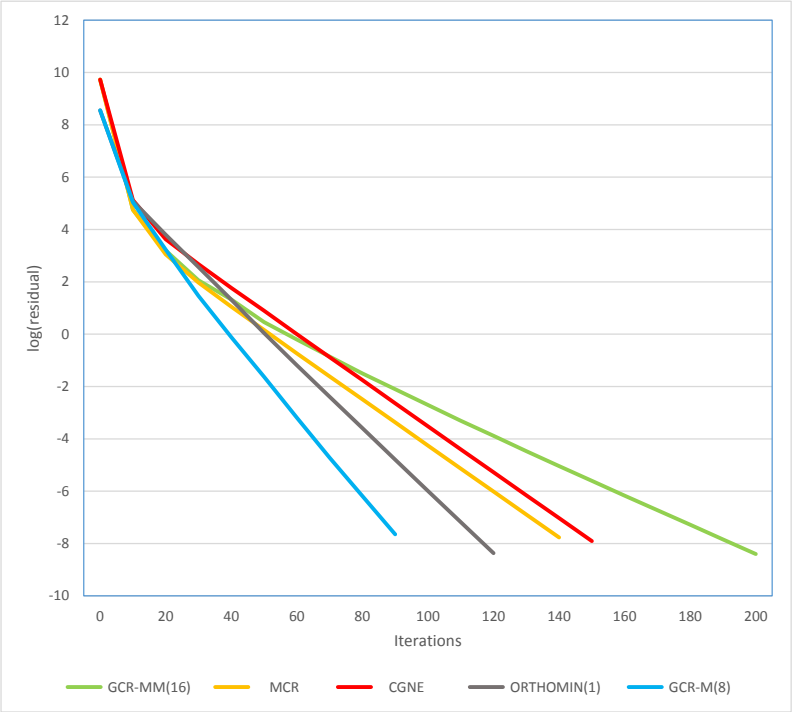


Figure 4.9: Plot showing how the residual reduces with iterations for DWF in a random gauge field, with $L_s = 16$ using different solvers. GCR-MM and GCR-M denotes GCR solving $\mathcal{M}^\dagger\mathcal{M}\,\psi = \chi$ and $\mathcal{M}\,\psi = \chi$ respectively.

vector operations.

Fig. 4.9 shows convergence of residual as a function of iteration count. The efficient solvers of GCR and OrthoMin are plotted for reference. The residual reduce steeply for GCR, OrthoMin and MCR compared to CG. It is important to note that where the former methods are based on conjugate residuals, the latter method CG is based on gradients.

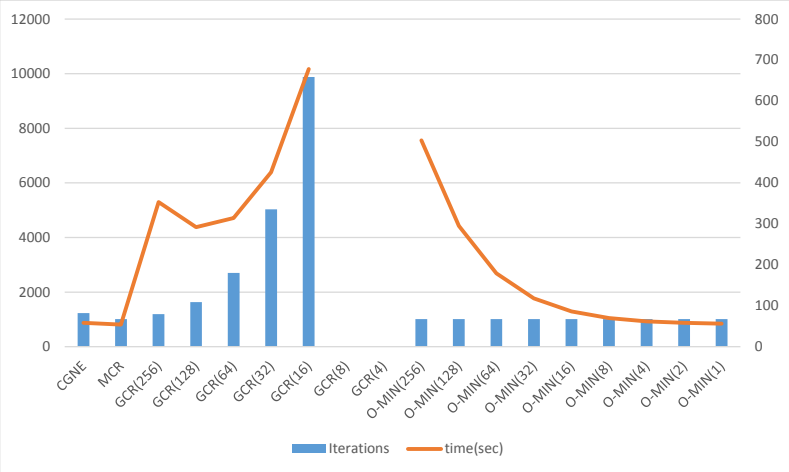


Figure 4.10: Plot showing number of iterations(left axis) and time taken (right axis) for DWF in a background QCD gauge field with $L_s = 16$ using different solvers in solving $M^\dagger M\,\psi = \chi$.

The results in Fig. 4.7 and Fig. 4.8 are of obtained for a random gauge. Using a QCD gauge configuration generated using Hybrid Monte-Carlo simulation is interesting as it changes the spectrum of the DWF Operator. Fig. 4.10 shows the results for solving hermition system $\mathcal{M}^\dagger\mathcal{M}\,\psi = \chi$ using different solvers. We see similar results as that for random gauge, but the fastest GCR solver is 40 times slower than CG. For solving non hermitian system $\mathcal{M}\,\psi = \chi$, GCR and OrthoMin do not converge. A closer study of the DWF operator and the impact of the fifth dimension is shown in Fig. 4.11. As $L_s$ increases linearly, the conditioning of the $\mathcal{M}$ worsens and convergence of GCR suffers exponentially when compared to CG.

From numerical analysis in [Nachtigal 92a, Nachtigal 92b], we can conclude that when the eigen values of the matrix lie in all four quadrants of the complex plane, the convergence of non-hermitian solvers(GCR with $\mathcal{M}$) is unreliable. In such cases, normal equations is the best we can do. Using $\mathcal{M}^\dagger\mathcal{M}$ is therefore the only option for good convergence. The GCR and OrthoMin solvers may perform

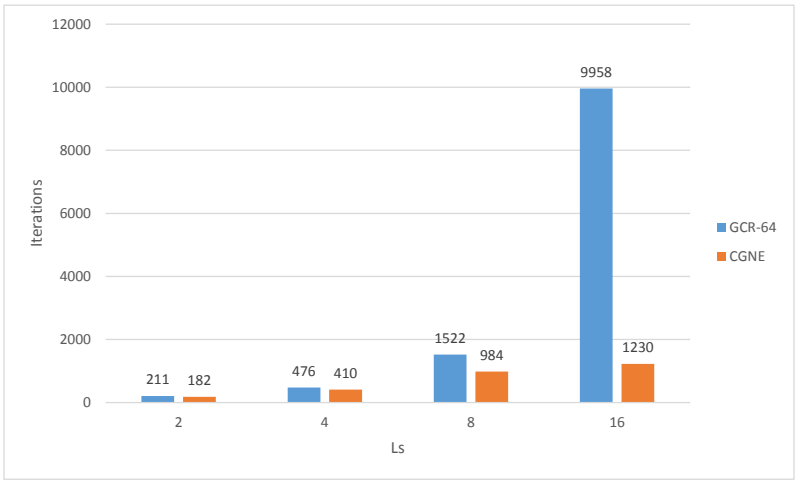


Figure 4.11: Plot showing number of iterations(left axis) and time taken (right axis) for DWF in a background QCD gauge field with increasing $L_s$ using different solvers in solving $M\,\psi = \chi$.

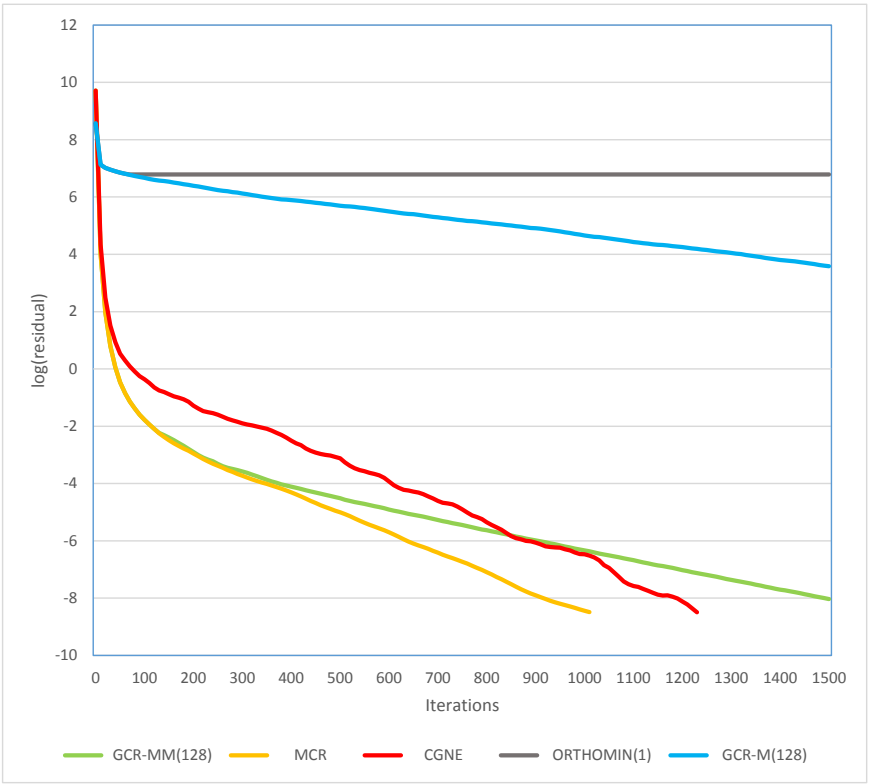


Figure 4.12: Plot showing how the residual reduces with iterations for DWF in a background QCD gauge field, with $L_s = 16$ using different solvers in solving $M^\dagger M\,\psi = \chi$.

better than the CG, if a good pre-conditioner is used as shown by the results from random gauge. Fig. 4.12 shows a closer look at the convergence of residual as a function of iterations. We can easily identify MCR as the most efficient algorithm as it takes 20% lesser time and number of iterations to solve the system.

### 4.8.1 Multi-shift MCR

In solving (4.4), the solution is usually repeated for different quark masses($m_q$). Instead of solving them separately, the solution for different quark masses with same source field can be computed simultaneously using multi-shift methods [Osborn 08, Bloch 09]. This is based on the fact that the Krylov subspaces are shift invariant

$$\mathcal{K}_m(\mathcal{D}, b) = \mathcal{K}_m(\mathcal{D} + m, b) \tag{4.8}$$

Multi-shift solvers are a key part in the Rational Hybrid Monte Carlo(RHMC) algorithm. This method can be used for any of the Kyrlov subspace methods. For DWF, we have found out that MCR is an efficient algorithm. In this thesis, we develop a multi-shift MCR algorithm that uses MCR as the solver for multiple shifts. The multiple shifts corresponds to poles in the rational approximation. For example the rational approximation of $\frac{1}{\sqrt[4]{x}}$ is given by

$$\begin{aligned}\frac{1}{\sqrt[4]{x}} = 8.12 + \frac{-6.46e^{-4}}{x+4.68e^{-3}} + \frac{-2.88e^{-3}}{x+2.5e^{-2}} + \frac{-9.44e^{-3}}{x+7.76e^{-2}} + \frac{-2.89e^{-4}}{x+2.05e^{-1}} \\ + \frac{-8.71e^{-2}}{x+5.10e^{-1}} + \frac{-2.62e^{-1}}{x+1.24} + \frac{-7.93e^{-1}}{x+3.01} + \frac{-2.47}{x+7.37} \\ + \frac{-8.19}{x+1.85e^{1}} + \frac{-3.21e^{1}}{x+5.02e^{1}} + \frac{-1.94e^{2}}{x+1.68e^{2}} + \frac{-5.33e^{3}}{x+1.26e^{3}}\end{aligned} \tag{4.9}$$

Fig. 4.13(top) shows how the rational function approximates $\frac{1}{\sqrt[4]{x}}$. The above approximation is accurate only in the interval $[0.3, 100]$ and is evident from the errors in rational approximation outside this interval as shown in Fig. 4.13(bottom). This approximation has 12 shifts and the solutions are computed in parallel.

The tests of this algorithm are performed on a $16^3 \times 32$ volume with stopping residual 1e-8 and $L_s = 16$. Table 4.1 compares the results from using Multi-shift MCR as a iterative solver in HMC runs for generating gauge configuration when compared to that for Multi-shift CG. In the table 4.1, efficiency refers to the acceptance per (CG/MCR) iteration and $\delta H$ refers to the extent of energy

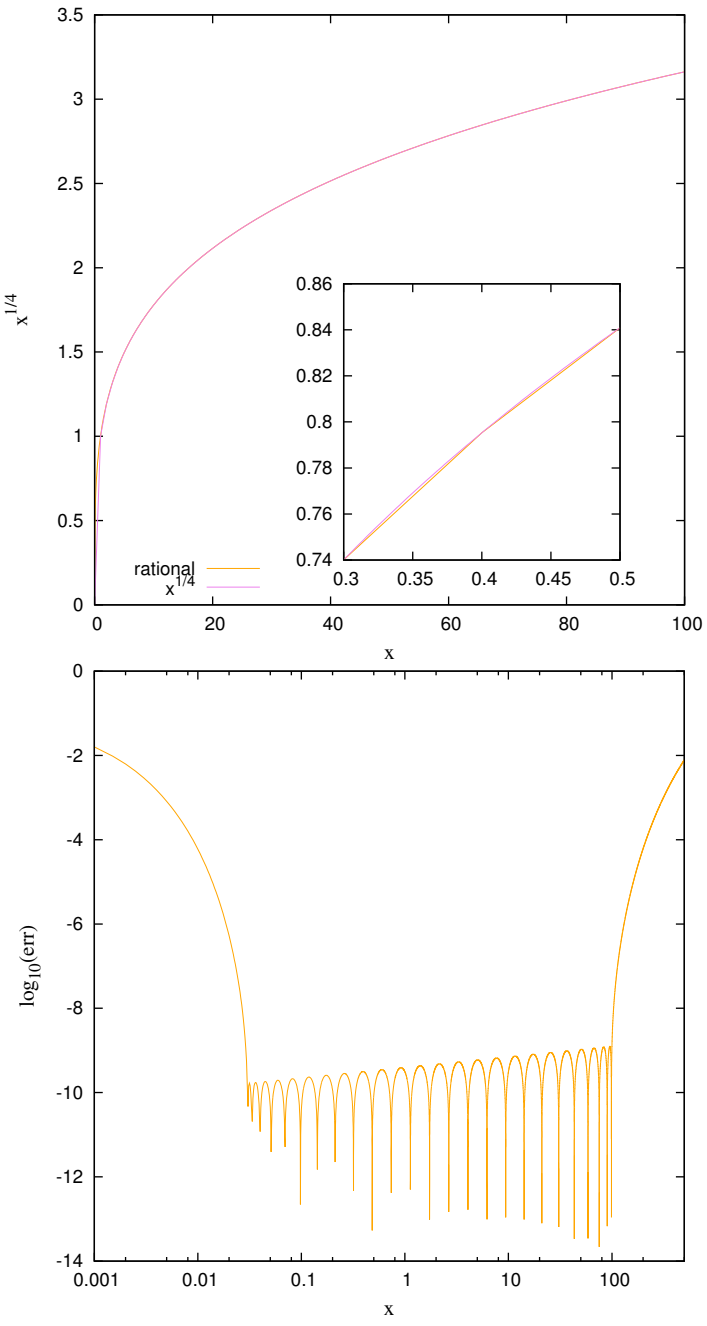


Figure 4.13: Plot showing - Top : $\frac{1}{\sqrt[4]{x}}$ and rational approximation as shown in (4.10). The inner plot zooms in for values $0.3 < x < 0.5$. Bottom : Error comupted as the absolute difference between the actual value ($\frac{1}{\sqrt[4]{x}}$) and its rational approximation.

| | CG | MCR |
|---|---|---|
| Metropolis Step | Accepted | Accepted |
| $\delta H$ | -9.717e-03 | 9.038e-03 |
| $\text{iteration}_{\text{avg}}$ | 905 | 658 |
| $\text{iteration}_{\text{min}}$ | 74 | 63 |
| $\text{iteration}_{\text{max}}$ | 8876 | 7951 |
| efficiency | 1.104e-03 | 1.506e-03 |
| Inversion time | 755s | 611s |
| Elapsed time | 904s | 760s |

Table 4.1: Comparison of results from using Multi-shift MCR and MCR as a iterative solver in HMC runs for generating gauge configuration when compared to that for Multi-shift CG and CG. $\delta H$ refers to the extent of energy conservation.

conversation. We can infer from the table that multi-shift MCR runs 18.5% faster compared to CG version. Hence, we have developed a new multi-shift algorithm that accelerates the evaluation of rational function by 18.5% in RHMC algorithm. In 2+1f Lattice simulations, the rational function evaluation takes 1/3 of the compute time and using this method will give a overall 6% gain in RHMC.

# Chapter 5

# Probing method for estimating the diagonal of the Dirac Matrix Inverse

## 5.1 Introduction

In lattice QCD, hadronic properties such as masses, matrix elements, decay constants and form factors can be computed in terms of correlation functions (as discussed in Chap. 2). After performing the Wick contractions, correlation functions are expressed as traces over products of quark propagators, Dirac matrices and color-structures. The construction of quark propagators by means of standard techniques of Lattice QCD usually involves statistical noise and particularly for disconnected graphs, prevents accurate computations of many physical observables. The reduction of this noise is always desirable.

On the lattice the quark propagator in coordinate space can be computed as the solution of the linear system

$$D\Phi = \eta, \tag{5.1}$$

where $D \in \mathbb{C}^{n\times n}$ is the lattice Dirac operator and $\eta$ a source vector. In its simplest form, $\eta$ is taken to be a point source, *i.e.*[1]

$$\eta(x') = \delta_{x'y}\,. \tag{5.2}$$

[1]For simplicity color and spinor indices are suppressed.

This implies that the solution of (5.1) yields the quark propagator from a single point $y$ to any other point $x$, which corresponds to just one column of the propagator matrix. In typical simulations of Lattice QCD, the sparse matrix $D$ has $O(10^9 \times 10^9)$ entries, and solving (5.1) to machine precision for all source positions, i.e. computing the whole propagator exactly, is therefore beyond the capabilities of even the most powerful supercomputers. Consequently the computation of propagator that start and end at the same space-time position poses a huge computational challenge and alternative methods are required.

Volume-filling random-noise sources have been proposed as a means to access the full propagator matrix [Bernardson 93, Dong 94, de Divitiis 96, Michael 98] by replacing it with a stochastic estimate. These stochastic "all-to-all" propagators have been successfully applied in a number of different contexts [Dong 94, de Divitiis 96, Michael 98, Foster 99, Struckmann 01, O'Cais 04, Boyle 08a] but usually a large computational effort is required in order to sufficiently reduce the intrinsic stochastic noise.

In this work, we apply a recently proposed "Probing" algorithm [Tang 11] for computing the diagonal entries of a matrix inverse in the context of Lattice QCD computations. These diagonal entries are those that enter into disconnected wick contractions of the local operators like $\langle \bar{u}(x)\gamma_5 u(x) \quad \bar{u}(0)\gamma_5 u(0)\rangle$, which is understood to be the flavour singlet state. For a selection of small lattice volumes, we compare the new probing method to the commonly used stochastic volume technique and the exact computation of the entire propagator matrix by means of point sources. While we use the new algorithm for the computation of mesonic flavor-singlet two point functions, we point out that it might be suitable for a wide range of applications.

### 5.1.1 Probing method

This section introduces the "Probing" method developed by Tang and Saad [Tang 11] for computing the diagonal of the inverse of a matrix denoted by $diag(D^{-1}) = diag(S)$. Probing is defined as a method of extracting entries of some unknown matrix by application of matrix product to probing vectors. For any unknown matrix, by constructing "s" vectors of length "n": $V_s := \{v_1, v_2, \ldots, v_s\}$, we can estimate the diagonal of a matrix $A \in [a_{ij}]$ using the

relation

$$diag(A) = \left[\sum_{k=1}^{s} v_k \odot Av_k\right] \oslash \left[\sum_{k=1}^{s} v_k \odot v_k\right] \tag{5.3}$$

where $\odot$ and $\oslash$ refers to the component wise multiplication and division. We can rewrite the above relation as

$$diag(A) = \left[A \odot V_s V_s^T\right] \oslash \left[V_s V_s^T\right] \tag{5.4}$$

To estimate the exact diagonal entries ($a_{ii}$), $V_s \in \mathbb{R}^{n\times s}$ matrix should be constructed such that the $i^{th}$ row of $V_s$ is orthogonal to all other rows of $j$ of $V_s$, for which $a_{ij} \neq 0$ [Bekas 07]. This is a sufficient condition which requires the knowledge of the non-zero pattern of the sparse matrix $A$. These methods have been successfully used for solving non-linear systems [Coleman 83].

The efficiency of this method is determined by the number of probing vectors and a value of $s \ll n$ is desirable. In fact if $s = n$, $V_n$ will be unitary matrix and we will get the exact diagonal of $A$. This method is suited for sparse matrices that are either banded or show decaying behaviour as we move away from the diagonal.

We are interested in diagonal of the inverse of Dirac matrix ($S = D^{-1}$). The above method proposed in [Bekas 07] is for estimating the diagonal of a unknown matrix. [Tang 11] extends the above method for estimating the diagonal of inverse of a sparse matrix. For $S$, we can approximate (5.4) as

$$diag(S) \approx diag(SV_sV_s^T)diag(V_sV_s^T)^{-1} \tag{5.5}$$

Now we are left with the problem of finding the probing vectors $V_s$ for $S = D^{-1}$. Even though the Dirac matrix is sparse, $S$ is dense. If we ignore entries in $S$ that are small, then $S$ can be approximated to a sparse and banded matrix. This is based on the approximate inverse preconditioners [Tang 11]. We can define a sparse matrix $S_\epsilon$ that ignore elements in $S$ less than some $\epsilon$. The sparsity pattern of $S_\epsilon$ can be approximated to $D^p$, for some integer $p$. The value of $p$ is dependent on the chosen $\epsilon$ value and increases as $\epsilon$ is reduced.

The probing method amounts to finding a suitable choice of probing vectors $\{v_j\}$ which recovers the non-zero entries of the matrix $S_\epsilon$. Since the structure of $S_\epsilon$ is unknown, this makes it even more difficult to find suitable choice of

probing vectors. In an earlier work an unbiased stochastic estimator of the inverse was constructed by using a sequence of random vectors [Bekas 07], but the convergence is found to be slow.

[Tang 11] proposes a new method of finding probing vectors by coloring the adjacency graph of the sparse matrix $D^p$, where the path length of at most $p$ are considered in the adjacency graph of $D$. We use Greedy Multicolouring Algorithm to color the adjacency graph associated with $D^p$ that has the same sparsity pattern as that of $S_\epsilon$. The algorithm is summarised in Algo. 5.

**Data**: Adjacency graph corresponding to an $n \times n$ matrix
**Result**: Colours of the vertices of the graph
Initialisation:
**for** *j=1 to n* **do**
| Set Color(j) = 0
**end**
**for** *j=1 to n* **do**
| Set Color(j) = min{ $k > 0 \mid k \neq$ Color($l$) $\forall l \in$ Adjacent(j) }
**end**

**Algorithm 5:** Greedy Multicolouring Algorithm

Having performed the colouring of the adjacency graph associated with $S_\epsilon$, the probing matrix $V_s = \{v_1, v_2, \ldots, v_s\}$ is derived from the coloured graph according to (5.6).

$$(V_s)^{jk} = \begin{cases} 1, \text{ if } Color(j) = k \\ 0, \text{ else} \end{cases} \tag{5.6}$$

The number of probing vectors $s$ is given by the number of required colours during the colouring process, i.e. $s = max\{k\}$. Following the procedure of (5.6), each row of $V_s$ will contain a single nonzero entry and $diag(V_s V_s^T) = diag(V_s V_s^T)^{-1} = I$.

In order to illustrate the above steps, Fig. 5.1 shows example of colouring the vertices of the adjacency graph associated with 3-dimensional matrix for $p$=1 (left) and $p$=2 (right). No boundary conditions are assumed for the above colouring example. The probing vectors corresponding to Colouring graphs in Fig. 5.1 is shown in (5.7). As shown in Fig. 5.1, we need 2 colours and 11 colours

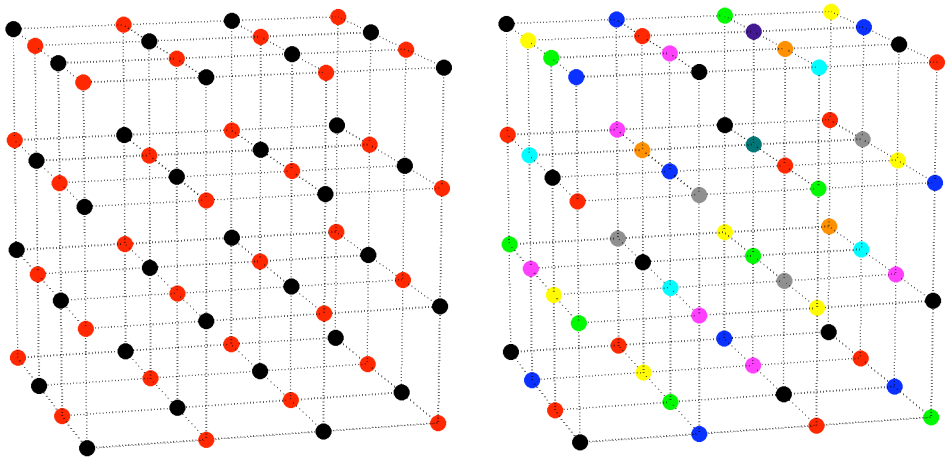

Figure 5.1: Colouring a adjacency graph of 3D matrix (dimension $4 \times 4 \times 4$) for path lengths: $p$=1 (left) and $p$=2 (right) with no boundary conditions. The Colouring is done starting in the left, front corner of the bottom plane. Then moving from front to back, left to right and finally bottom to top. We require 2 and 11 different colours to color the adjacency graph corresponding to $p$=1 and $p$=2 respectively

to color the adjacency graph for path lengths: $p$=1 and $p$=2 respectively. As a result of this the probing vector in (5.7) has only 2 and 11 columns.

$$V_2 = \begin{bmatrix} 1 & 0 \\ 0 & 1 \\ 1 & 0 \\ \vdots & \vdots \\ 1 & 0 \\ 0 & 1 \end{bmatrix}, \qquad V_{11} = \begin{bmatrix} 1 & 0 & 0 & \dots & 0 \\ 0 & 1 & 0 & \cdots & 0 \\ 0 & 0 & 1 & \cdots & 0 \\ 1 & 0 & 0 & \dots & 0 \\ \vdots & \vdots & \vdots & \dots & \vdots \\ 0 & 0 & 0 & \dots & 1 \end{bmatrix} \tag{5.7}$$

Having constructed $V_s$ its columns are used as source vectors for solving the linear system

$$Dx_i = v_i, \tag{5.8}$$

yielding a set of solution vectors $X_s := \{x_1, x_2, \dots, x_s\} := S_\epsilon V_s$. Assuming $diag(V_s V_s^T)^{-1} = I$, an estimate of the inverse of the sparsified matrix can be estimated as

$$diag(S_\epsilon) \approx diag(X_s V_s^T). \tag{5.9}$$

The probing method significantly reduces the computational effort by solving only $s \ll n$ linear equations which can be done by using any iterative solvers. Applying this method for the Lattice Dirac operator the colouring is performed in space and time only, i.e. the internal spin and color structure is not coloured and periodic boundary conditions are used. In other words the ones in the matrix $V_s$ are a unit matrix in spin-color space, i.e. $1 \triangleq \mathbb{I}_{12\times 12}$. Consequently a point source is used for each of the spin-color indices and $x_i$ is evaluated separately for each of the 12 spin-color indices. Algo. 6 summarises the probing algorithm used for estimating the diagonal of the inverse lattice Dirac operator.

**Data**: Lattice Dirac operator $D$, matrix of dimension $V \times 12$
**Result**: Estimate of the diagonal of the inverse $\mathcal{D}(D_\epsilon^{-1}) = \mathcal{D}(S_\epsilon)$
Initialisation:
**for** *any p* **do**
  Color the vertices of the adjacency graph in space and time coordinates; no Colouring in spin and color indices. Apply the corresponding boundary conditions.
  Construct probing matrix $V_s = \{v_1, v_2, \ldots, v_s\}$ according to (5.6), i.e. $(V_s)^{ik} = 1_{12\times 12}$ if Color$(i) = j$, or $0_{12\times 12}$ otherwise
  **for** *i=1 to s* **do**
    **for** *j=1 to 12* **do**
      Solve (5.8) for each spin-color index $j$ using a Krylov subspace method.
    **end**
    Construct $x_i$
  **end**
  Construct $X_s := \{x_1, x_2, \ldots, x_s\}$
  Compute $\mathcal{D}(D_\epsilon^{-1}) = \mathcal{D}(X_s V_s^T)$
  Set $\mathcal{D}(S) := \mathcal{D}(S_\epsilon) = \mathcal{D}(D_\epsilon^{-1})$
**end**

**Algorithm 6:** Algorithm to probe the diagonal of the Dirac operator

In the above algorithm, the computation expense is proportional to $p$ since $s$ increases with $p$. As the value of cutoff $\epsilon$ is reduced, the value of $p$ increases and the precision of diag$(D)$ increases. Thus the value of $p$ has to be chosen carefully so that a balance of precision and cost is achieved. Also if a certain $p$ does

not achieve a required accuracy, a new distance $p$ can not make use of previous computations since its probing vectors are not related to the previous ones. A recent advance referred to as hierarchical probing [Stathopoulos 13] allows to reuse results from prior choices of $p$.

## 5.2 Results

For this work, we used gauge configurations with $N_f = 2$ flavors of dynamical Wilson fermions. The configurations are generated using the deflation-accelerated DD-HMC algorithm [Luscher 05] which combines domain-decomposition (DD) methods [Saad 03] with the Hybrid Monte Carlo (HMC) algorithm [Duane 87] and the Sexton-Weingarten multiple-time integration scheme [Sexton 92]. The Wilson-Dirac operator of (5.1) is inverted using a iterative method called GCR and Schwarz-preconditioner (SAP+GCR) algorithm [Luscher 04].

As part of the study two lattice volumes, $8^4$ ($\beta = 5.30, \kappa = 0.13625$, 300 configurations) and $16^4$ ($\beta = 5.30, \kappa = 0.13620$, 99 configurations) are considered. This method is compared to the exact method and the volume-filling stochastic method that uses sources with dilution in space, time and spin-color.

In addition to probing the diagonal of the inverse Dirac matrix and computing the trace, we also compare physical observables by comparing the 2pt correlation functions and its disconnected part

$$C_2^{FULL}(t) = \sum_{\vec{x},\vec{y}} \gamma_5 S^\dagger(y,x)\gamma_5 \Gamma S(y,x)\Gamma'^\dagger - \sum_{\vec{y}} \gamma_5 S^\dagger(y,y)\gamma_5\Gamma \sum_{\vec{x}} S(x,x)\Gamma'^\dagger \quad (5.10)$$

$$C_2^{DIS}(t) = \sum_{\vec{y}} \gamma_5 S^\dagger(y,y)\gamma_5\Gamma \sum_{\vec{x}} S(x,x)\Gamma'^\dagger \quad (5.11)$$

In (5.10) and (5.11) we measure and compare scalar ($\Gamma = 1$), pseudo-scalar ($\Gamma = \gamma_5$) and axial ($\Gamma = \gamma_5\gamma_{0123}$) channels.

For the $8^4$ volume, we estimate the diagonal of a single loop propagator ($S(x,x)\Gamma$) from stochastic, probing and exact method . The "Exact" solution is obtained by using point sources for all space-time locations. This method estimates numerically the most accurate solution but is usually not used for real lattice calculations. From these measurement we estimate the "Goodness" of the

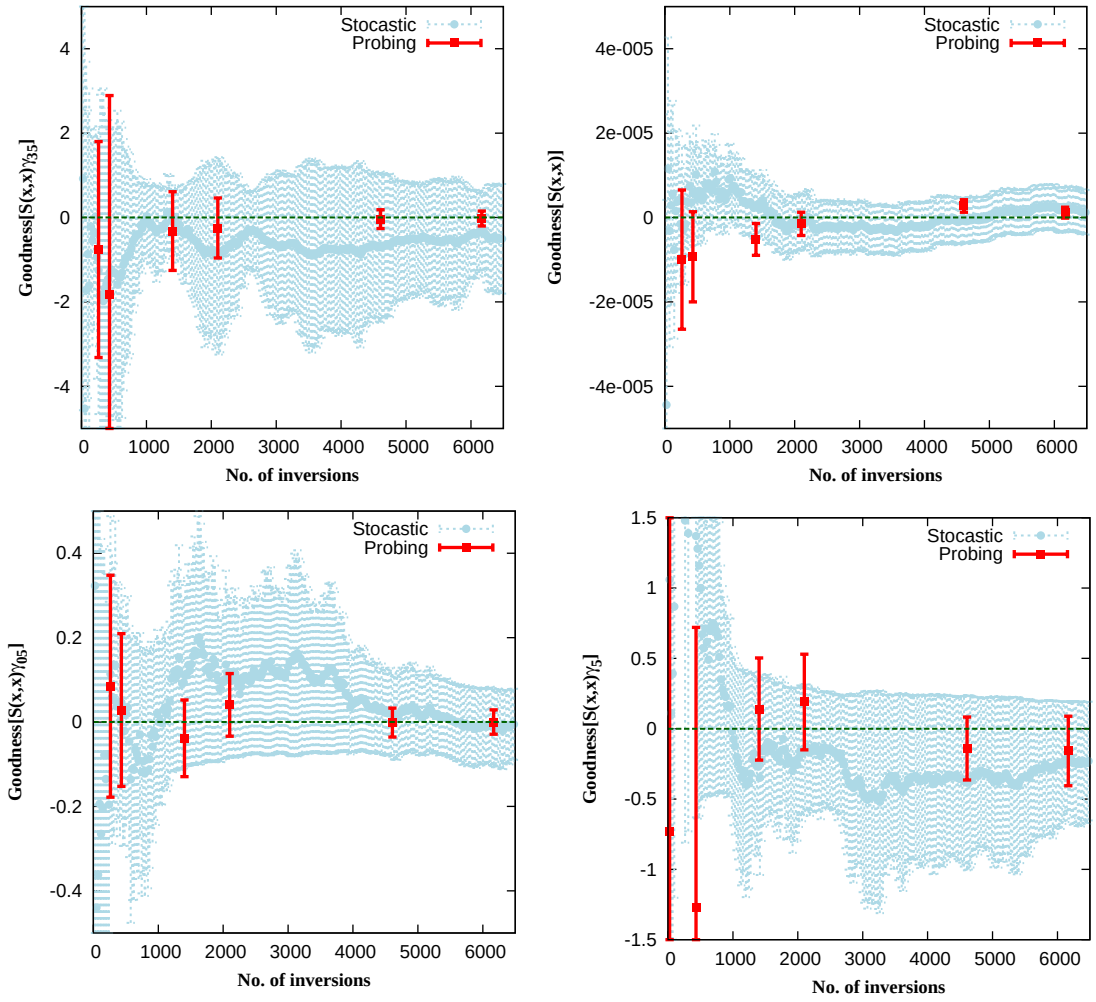


Figure 5.2: Goodness (5.12) of probing and stochastic method compared to exact for the measurement of single loop scalar (1-top right), pseudo-scalar ($\gamma_5$-bottom right) and axial ($\gamma_0\gamma_5$-bottom left, $\gamma_3\gamma_5$-top left) channel in a $8^4$ lattice with 300 configurations

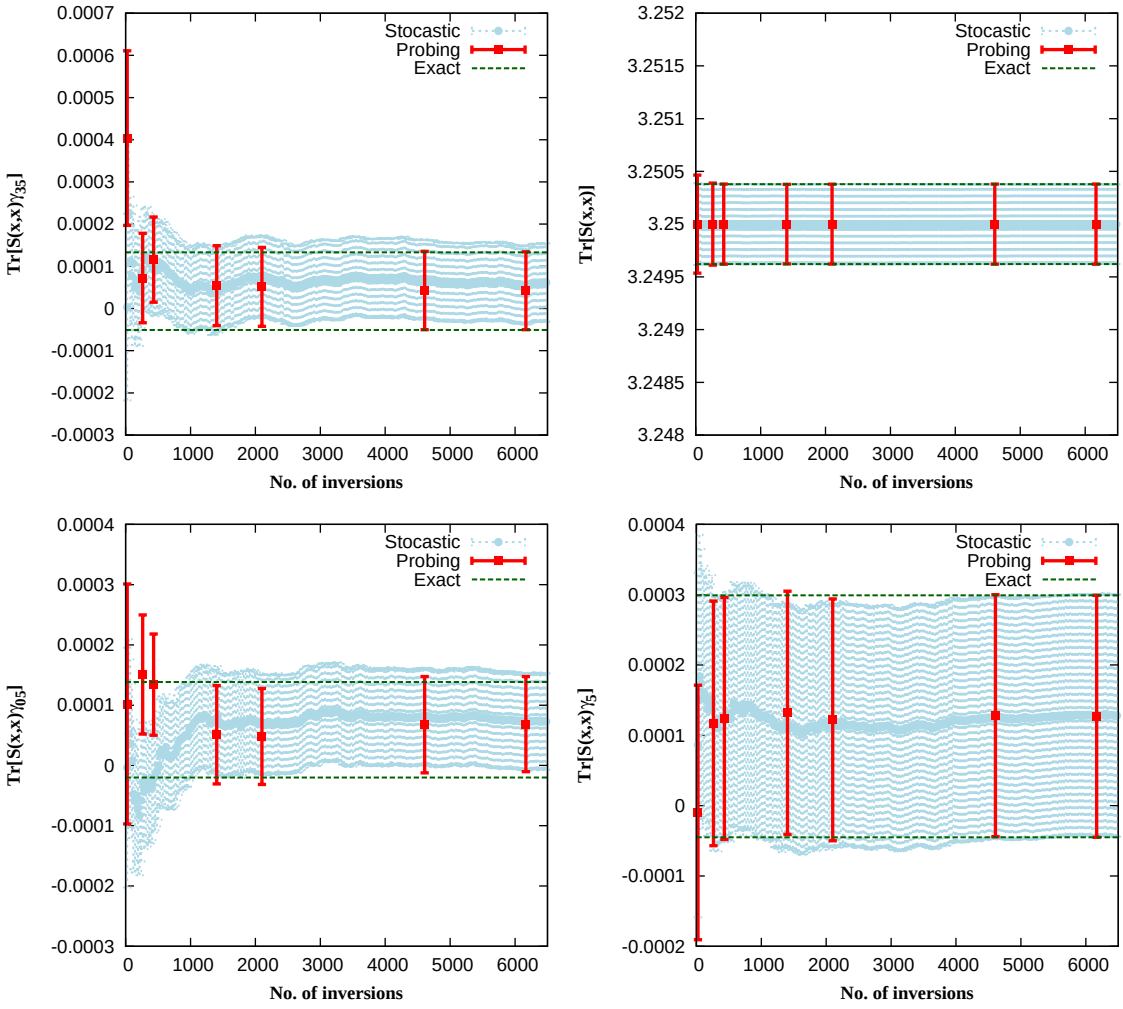


Figure 5.3: Comparison of measured value of single loop scalar (1-top right), pseudo-scalar ($\gamma_5$-bottom right) and axial ($\gamma_0\gamma_5$-bottom left, $\gamma_3\gamma_5$-top left) channel for probing and stochastic method in a $8^4$ lattice with 300 configurations

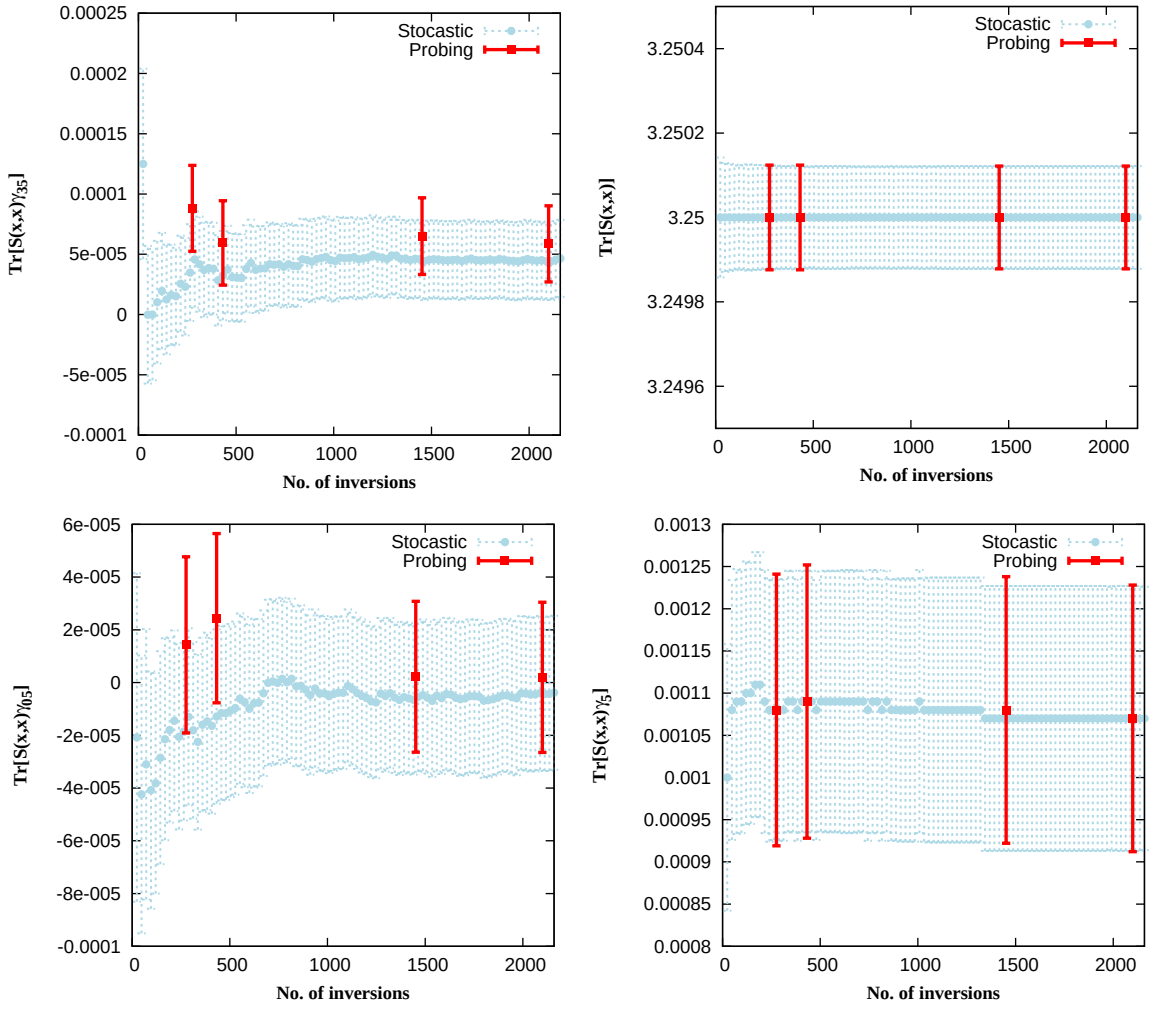


Figure 5.4: Comparison of measured value of single loop scalar (1-top right), pseudo-scalar ($\gamma_5$-bottom right) and axial ($\gamma_0\gamma_5$-bottom left, $\gamma_3\gamma_5$-top left) channel for probing and stochastic method in a $16^4$ lattice with 99 configurations

method compared to exact method as shown in (5.12).

$$\text{Goodness} = 1 - \frac{\text{Tr}[S(x,x)\Gamma]_{method}}{\text{Tr}[S(x,x)\Gamma]_{exact}}, \tag{5.12}$$

where *method* refers to either the stochastic or probing approach and the trace is over space and time. The exact method is very expensive as it requires $Volume \times 12$ inversion for lattice and for this reason the Goodness is not measured in the $16^4$ volume. The method with Goodness closer to zero is considered as the method closer to the exact solution. This Goodness is measured as a function of number of inversions required and as number of inversions reach $Volume \times 12$, we can expect the Goodness to be exactly zero.
Fig.5.2 shows the Goodness (5.12) of probing and stochastic methods compared to exact for the measurement of single loop propagator in $8^4$ volume. Probing solution is closer to the exact solution than that of stochastic for all channels. We can see better improvement in Goodness as the number of inversion ($p$) for probing are increased when compared to (nhits) stochastic. Fig.5.3 compares the measured value of single loop propagator for probing and stochastic method in the $8^4$ volume. Even though the probing method is closer to the exact solution (as shown by the Goodness plots) the measured propagator shows no statistical difference between stochastic and probing method. Similar results are seen for $16^4$ volume as shown in Fig.5.4 and we can conclude that Gauge noise is dominant when compared to stochastic noise.

Fig. 5.6 and Fig. 5.5 compares the 2-pt correlation function and its disconnected part measured using both the probing and stochastic method. For comparison, we consider $p$=4 for probing and nhits=50 for stochastic as they have same number of inversions. Again we see similar results as the probing shows almost little or no improvement over the stochastic method. We can see that even though the probing method is closer to the exact solution the statistical error obtained by using probing and stochastic method is almost same. This is due to the dominating gauge noise which kills any improvement from using the probing method.

From studying two different lattice volumes, we can clearly see that $p$=4 as a good candidate for lattice measurement, as the results are stable and the statistical noise is minimal. An advantage of the probing method is that for a

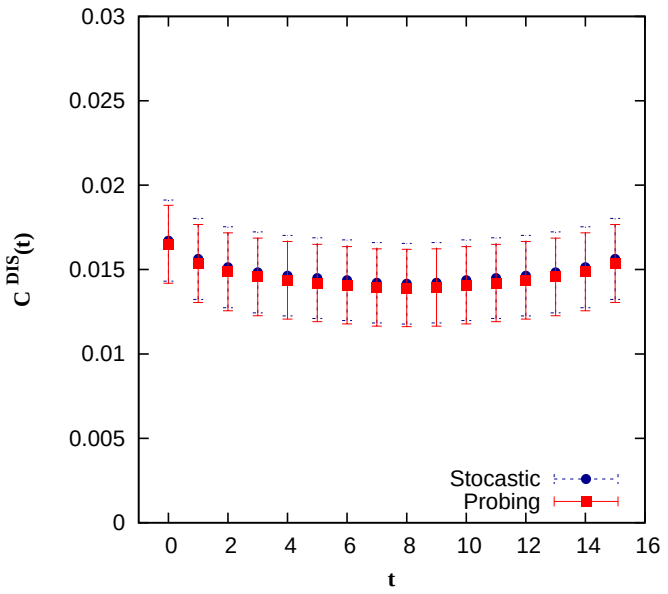


Figure 5.5: Comparison of measured value of 2pt correlation function, disconnected part (5.11) with $\Gamma = \Gamma' = \gamma_5$ for probing and stochastic method in a $16^4$ lattice with 99 configurations

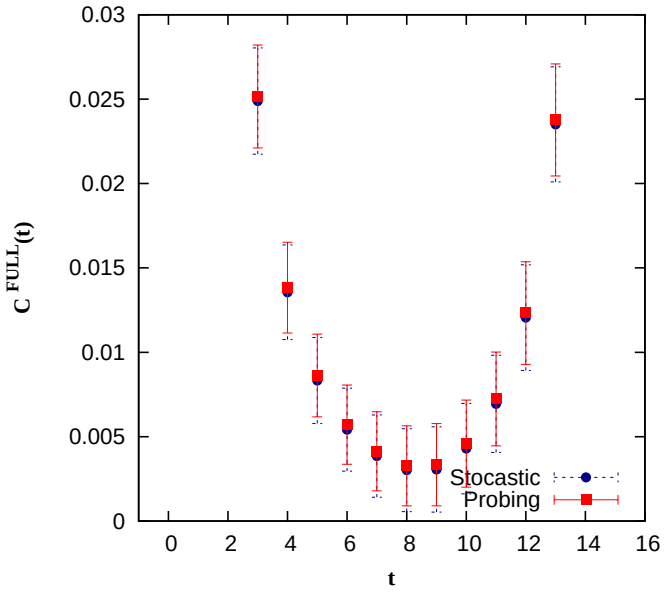


Figure 5.6: Comparison of measured value of 2pt correlation function, disconnected part (5.10) $\Gamma = \Gamma' = \gamma_5$ for probing and stochastic method in a $16^4$ lattice with 99 configurations

fixed $p$, the number of inversion is almost constant for increasing lattice volume. When compared to stochastic method that uses dilution in time, the cost of probing is considerable less as the cost for stochastic methods increase linearly with increase in lattice volume. The main source of statistical noise comes from gauge configurations and using probing methods for gauge generation should be considered in future.

# Conclusions

In this thesis, we have successfully calculated the $K_{l3}$ form factor in $N_f = 2 + 1$ Lattice QCD using domain wall fermions. With three different lattice spacings and near physical quark masses, these lattice simulations have helped us reduce the systematic errors in the determination of the $K_{l3}$ form factor.

A significant improvement in the calculation was achieved through the use of a new kinematic arrangement of the twisted boundary conditions as applied to the pion and kaon and by motivating a new ansatz for the mass extrapolation to the physical point. The final value of $K_{l3}$ form factor is

$$f_+^{K\pi}(0) = 0.9671(17)(^{+18}_{-46})$$

where the first error is statistical and the second error systematic. From the above result for $K_{l3}$ form factor, we estimated the value of the CKM matrix element $|V_{us}|$:

$$|V_{us}| = 0.2237(^{+13}_{-\ 8})$$

which confirmed unitarity of the first row CKM matrix in the Standard Model.

In this thesis, we have successfully ported the Clover Lattice fermion action to Blue Gene/Q architecture. The optimised Clover term achieved a maximum efficiency of 29.1% and 20.2% for single and double precision respectively for iterative Conjugate Gradient solver for the Clover fermion action. This optimised version showed good Weak scaling. Strong scaling showed local volume dependency due to the effects of cache capacity and network bandwidth.

We have studied the different iterative solvers for Domain Wall Fermion action (DWF) and found that Modified Conjugate Residual(MCR) as the most efficient solver compared to CG and GCR. We have developed a new multi-shift MCR algorithm that is 18.5% faster compared to multi-shift CG for the evaluation of

rational functions in RHMC.

We have introduced a new probing technique for estimating the diagonal of the inverse Dirac operator. This probing method is found to be closer to the exact solution when compared to stochastic methods for the same cost. This is important in the evaluation of disconnected correlation functions.

# Appendix A

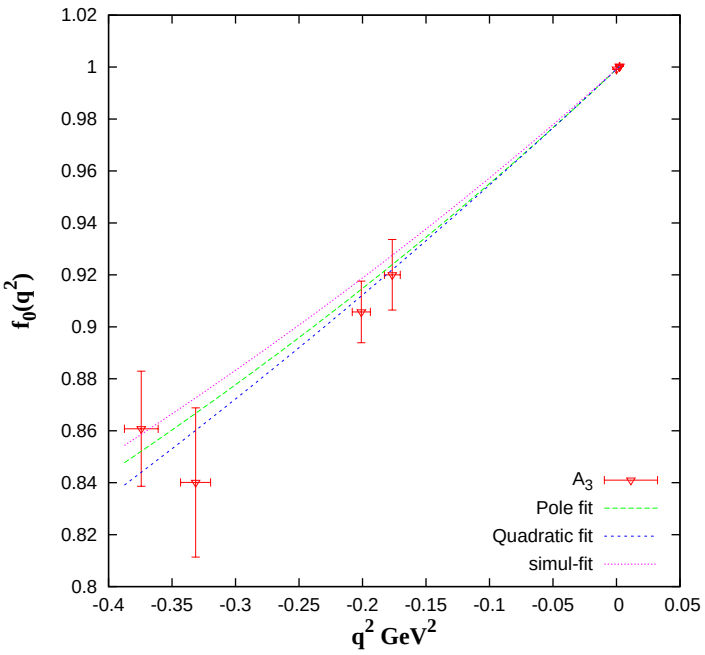


Figure A.1: Plot showing $f_0(q^2)$ dependence on $q^2$, pole fit, Quadratic fit and simul fit for ensemble $A_3$

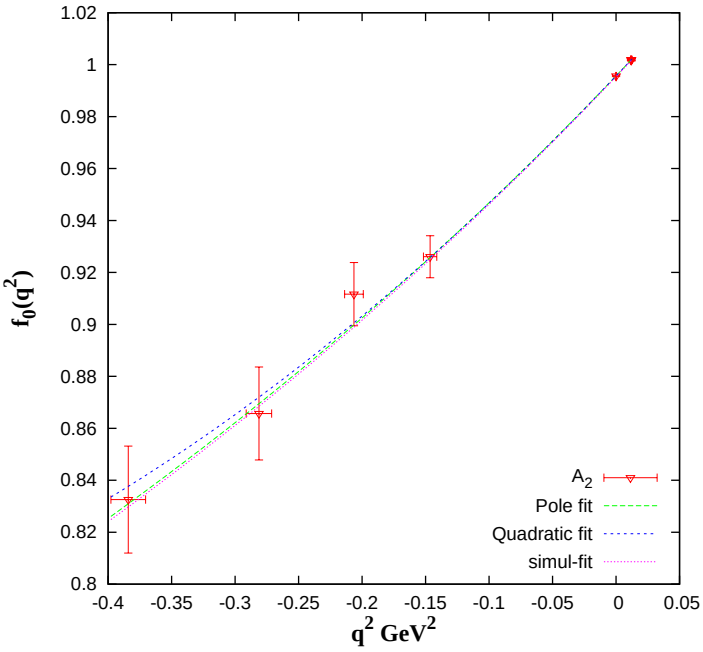


Figure A.2: Plot showing $f_0(q^2)$ dependence on $q^2$, pole fit, Quadratic fit and simul fit for ensemble $A_2$

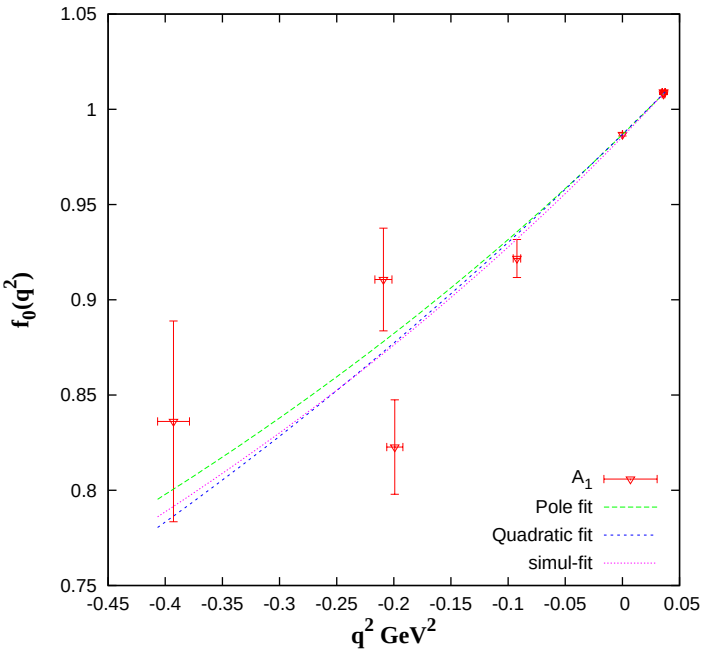


Figure A.3: Plot showing $f_0(q^2)$ dependence on $q^2$, pole fit, Quadratic fit and simul fit for ensemble $A_1$

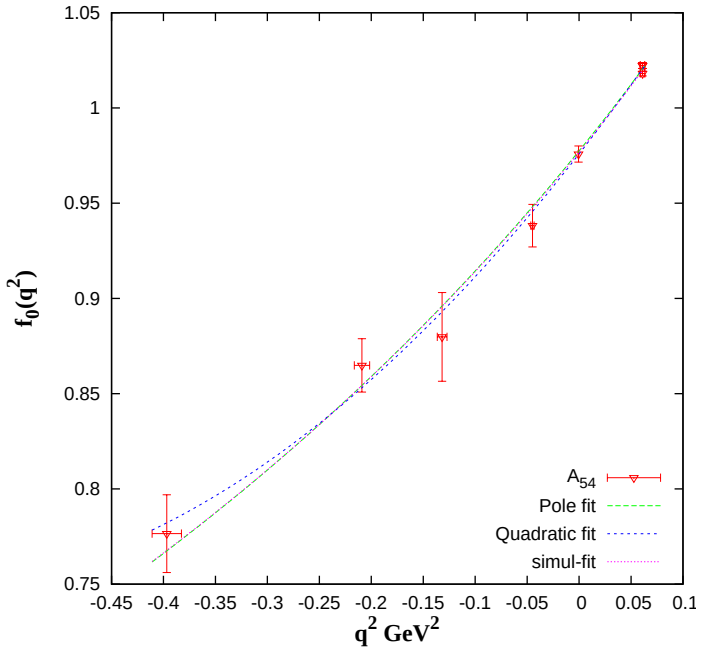


Figure A.4: Plot showing $f_0(q^2)$ dependence on $q^2$, pole fit, Quadratic fit and simul fit for ensemble $A_4^5$

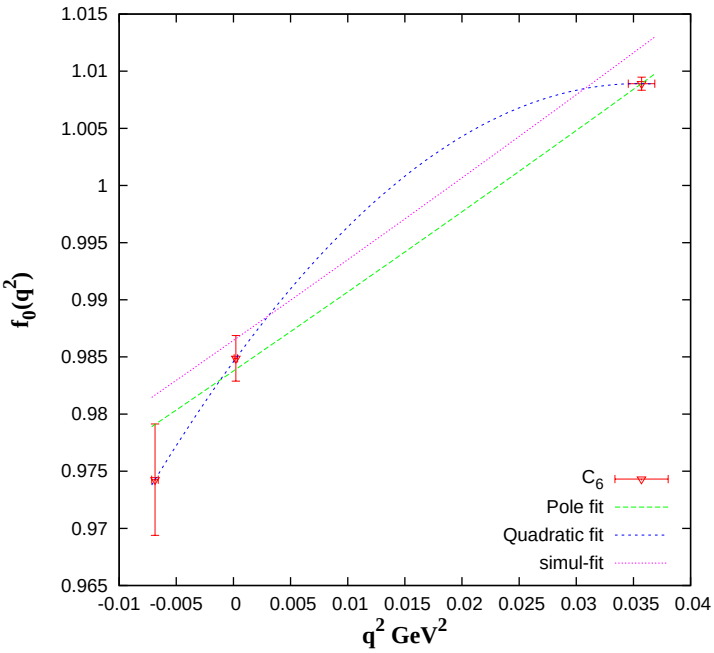


Figure A.5: Plot showing $f_0(q^2)$ dependence on $q^2$, pole fit, Quadratic fit and simul fit for ensemble $C_6$

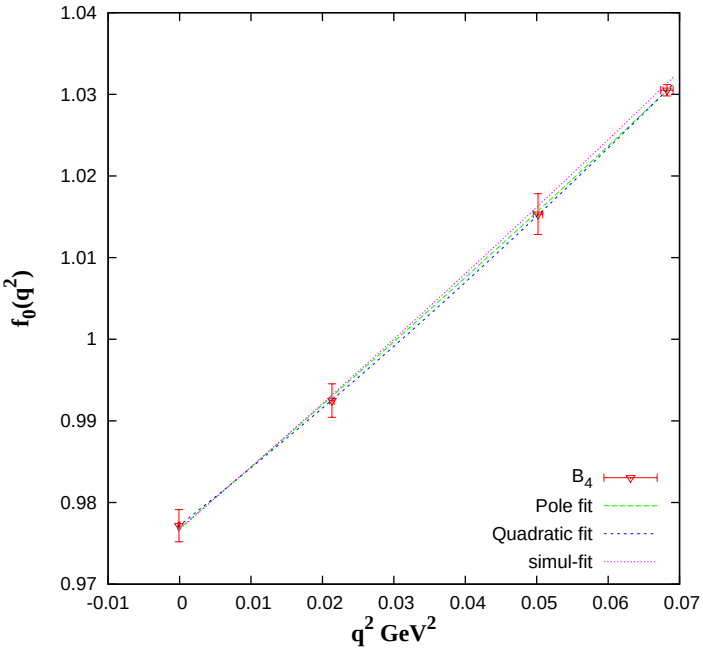


Figure A.6: Plot showing $f_0(q^2)$ dependence on $q^2$, pole fit, Quadratic fit and simul fit for ensemble $B_4$

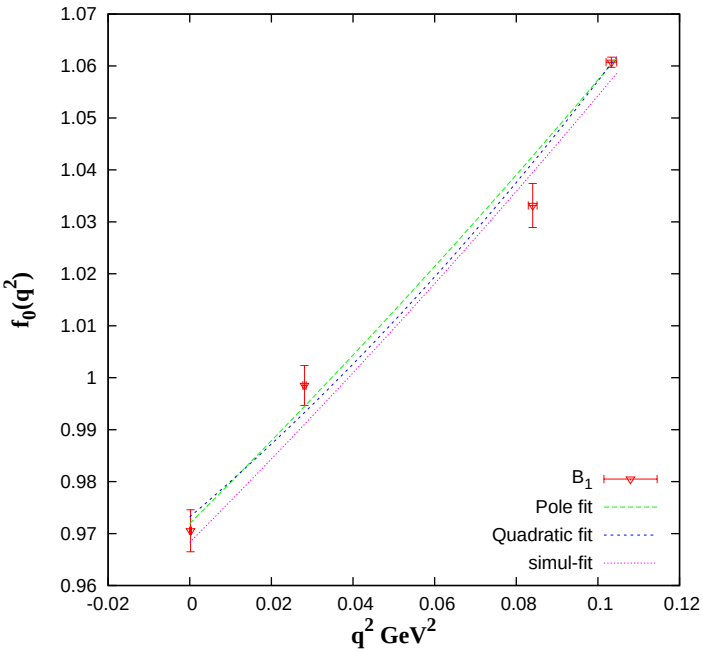


Figure A.7: Plot showing $f_0^{K\pi}(q^2)$ dependence on $q^2$, pole fit, Quadratic fit and simul fit for ensemble $B_1$

# Bibliography


[Ademollo 64] M. Ademollo & Raoul Gatto. *Nonrenormalization Theorem for the Strangeness Violating Vector Currents.* Phys.Rev.Lett., vol. 13, pages 264–265, 1964.

[Alexopoulos 04] T. Alexopoulos*et al.* *A Determination of the CKM parameter —V(us)—.* Phys.Rev.Lett., vol. 93, page 181802, 2004.

[Allton 08] C. Allton*et al.* *Physical Results from 2+1 Flavor Domain Wall QCD and SU(2) Chiral Perturbation Theory.* Phys.Rev., vol. D78, page 114509, 2008.

[Antonelli 10] M. Antonelli, V. Cirigliano, G. Isidori, F. Mescia, M. Moulson*et al.* *An Evaluation of $|V_us|$ and precise tests of the Standard Model from world data on leptonic and semileptonic kaon decays.* Eur.Phys.J., vol. C69, pages 399–424, 2010.

[Aoki 11] Y. Aoki*et al.* *Continuum Limit Physics from 2+1 Flavor Domain Wall QCD.* Phys.Rev., vol. D83, page 074508, 2011.

[Arthur 13] R. Arthur*et al.* *Domain Wall QCD with Near-Physical Pions.* Phys.Rev., vol. D87, page 094514, 2013.

[Bazavov 12] A. Bazavov, C. Bernard, C.M. Bouchard, C. DeTar, Daping Du*et al.* *Kaon semileptonic vector form factor and determination of $|V_{us}|$ using staggered fermions.* 2012.

[Becirevic 05a] D. Becirevic, D. Guadagnoli, G. Isidori, V. Lubicz, G. Martinelli*et al.* *SU(3)-breaking effects in kaon and hyperon semileptonic decays from lattice QCD.* Eur.Phys.J., vol. A24S1, pages 69–73, 2005.

[Becirevic 05b] D. Becirevic, G. Isidori, V. Lubicz, G. Martinelli, F. Mescia*et al.* *The K to pi vector form-factor at zero momentum transfer on the lattice.* Nucl.Phys., vol. B705, pages 339–362, 2005.

[Becirevic 06] Damir Becirevic, Guido Martinelli & Giovanni Villadoro. *The Ademollo-Gatto theorem for lattice semileptonic decays.* Phys.Lett., vol. B633, pages 84–88, 2006.

[Bedaque 05] Paulo F. Bedaque & Jiunn-Wei Chen. *Twisted valence quarks and hadron interactions on the lattice.* Phys.Lett., vol. B616, pages 208–214, 2005.

[Bekas 07] C. Bekas, E. Kokiopoulou & Y. Saad. *An estimator for the diagonal of a matrix.* Applied Numerical Mathematics, vol. 57, no. 1112, pages 1214 – 1229, 2007. ¡ce:title¿Numerical Algorithms, Parallelism and Applications (2)¡/ce:title¿.

[Beringer 12] J. Beringer*et al.* *Review of Particle Physics (RPP).* Phys.Rev., vol. D86, page 010001, 2012.

[Bernardson 93] S. Bernardson, P. McCarty & C. Thron. *Monte Carlo methods for estimating linear combinations of inverse matrix entries in lattice QCD.* Comput.Phys.Commun., vol. 78, pages 256–264, 1993.

[Bijnens 03] Johan Bijnens & Pere Talavera. *K(l3) decays in chiral perturbation theory.* Nucl. Phys., vol. B669, pages 341–362, 2003.

[Bloch 09] Jacques C.R. Bloch, Tobias Breu, Andreas Frommer, Simon Heybrock, Katrin Schafer*et al.* *Krylov subspace methods and the sign function: multishifts and deflation in the non-Hermitian case.* PoS, vol. LAT2009, page 043, 2009.

[Boyle 04] P.A. Boyle. *Four momentum boosted fermion fields.* Nucl.Phys.Proc.Suppl., vol. 129, pages 358–360, 2004.

[Boyle 05] P.A. Boyle, D. Chen, N.H. Christ, M. Clark, Saul D. Cohen*et al.* *The status of user software on QCDOC.* Nucl.Phys.Proc.Suppl., vol. 140, pages 829–831, 2005.

[Boyle 07] P.A. Boyle, J.M. Flynn, A. Juttner, C.T. Sachrajda & J.M. Zanotti. *Hadronic form factors in Lattice QCD at small and vanishing momentum transfer.* JHEP, vol. 0705, page 016, 2007.

[Boyle 08a] P.A. Boyle, A. Juttner, C. Kelly & R.D. Kenway. *Use of stochastic sources for the lattice determination of light quark physics.* JHEP, vol. 0808, page 086, 2008.

[Boyle 08b] P.A. Boyle, A. Juttner, R.D. Kenway, C.T. Sachrajda, S. Sasaki*et al.* *K(l3) semileptonic form-factor from 2+1 flavour lattice QCD.* Phys.Rev.Lett., vol. 100, page 141601, 2008.

[Boyle 09] Peter A. Boyle. *The BAGEL assembler generation library.* Comput.Phys.Commun., vol. 180, pages 2739–2748, 2009.

[Boyle 10] P.A. Boyle*et al.* *K $\pi$ form factors with reduced model dependence.* Eur.Phys.J., vol. C69, pages 159–167, 2010.

[Boyle 12a] PA Boyle. *The BlueGene/Q Supercomputer*. In The 30 International Symposium on Lattice Field Theory-Lattice, volume 2012, 2012.

[Boyle 12b] Peter A. Boyle, Jonathan M. Flynn, Andreas Juttner, Christopher Sachrajda, Karthee Sivalingam*et al.* *Kaon semileptonic decays near the physical point*. PoS, vol. LATTICE2012, page 112, 2012.

[Boyle 13a] Peter A. Boyle, Jonathan M. Flynn, Nicolas Garron, Andreas Jttner, Chris T. Sachrajda*et al.* *The kaon semileptonic form factor with near physical domain wall quarks*. JHEP, vol. 1308, page 132, 2013.

[Boyle 13b] Peter A. Boyle & Karthee Sivalingam. *Clover fermion action for Blue gene-Q and Iterative solvers for DWF*, August 2013. `http://www.lattice2013.uni-mainz.de/static/AM.html#contrib4078`.

[Cabibbo 63] Nicola Cabibbo. *Unitary Symmetry and Leptonic Decays*. Phys.Rev.Lett., vol. 10, pages 531–533, 1963.

[Cabibbo 04] Nicola Cabibbo, Earl C. Swallow & Roland Winston. *Semileptonic hyperon decays and CKM unitarity*. Phys.Rev.Lett., vol. 92, page 251803, 2004.

[Chandra 77] R. Chandra, S.C. Eisenstat & M.H. Schultz. The modified conjugate residual method for partial differential equations. Department of Computer Science: Research report. Defense Technical Information Center, 1977.

[Clark 04] M.A. Clark & A.D. Kennedy. *The RHMC algorithm for two flavors of dynamical staggered fermions*. Nucl.Phys.Proc.Suppl., vol. 129, pages 850–852, 2004.

[Clark 05] M.A. Clark, A.D. Kennedy & Z. Sroczynski. *Exact 2+1 flavour RHMC simulations*. Nucl.Phys.Proc.Suppl., vol. 140, pages 835–837, 2005.

[Colangelo 11] Gilberto Colangelo, Stephan Durr, Andreas Juttner, Laurent Lellouch, Heinrich Leutwyler*et al.* *Review of lattice results concerning low energy particle physics*. Eur.Phys.J., vol. C71, page 1695, 2011.

[Coleman 83] Thomas F. Coleman & Jorge J. Moré. *Estimation of sparse Jacobian matrices and graph coloring problems*. vol. 20, no. 1, pages 187–209, February 1983.

[Dawson 06] C. Dawson, T. Izubuchi, T. Kaneko, S. Sasaki & A. Soni. *Vector form factor in K(l3) semileptonic decay with two flavors of*

*dynamical domain-wall quarks.* Phys.Rev., vol. D74, page 114502, 2006.

[de Divitiis 96] G.M. de Divitiis, R. Frezzotti, M. Masetti & R. Petronzio. *Pseudofermion observables for static heavy meson decay constants on the lattice.* Phys.Lett., vol. B382, pages 393–397, 1996.

[de Divitiis 04] G. M. de Divitiis, R. Petronzio & N. Tantalo. *On the discretization of physical momenta in lattice QCD.* Phys. Lett., vol. B595, pages 408–413, 2004.

[Dong 94] Shao-Jing Dong & Keh-Fei Liu. *Stochastic estimation with Z(2) noise.* Phys.Lett., vol. B328, pages 130–136, 1994.

[Duane 87] S. Duane, A.D. Kennedy, B.J. Pendleton & D. Roweth. *Hybrid Monte Carlo.* Phys.Lett., vol. B195, pages 216–222, 1987.

[Edwards 05] Robert G. Edwards & Balint Joo. *The Chroma software system for lattice QCD.* Nucl.Phys.Proc.Suppl., vol. 140, page 832, 2005.

[Efron 79] B. Efron. *Bootstrap methods: another look at the jacknife.* Ann. Statist., vol. 7, pages 1–26, 1979.

[etal 06] WM Yao etal. *Review of Particle Physics.* Journal of Physics G: Nuclear and Particle Physics, vol. 33, no. 1, page 1, 2006.

[Flynn 06] J. M. Flynn, A. Jüttner & C. T. Sachrajda. *A numerical study of partially twisted boundary conditions.* Phys. Lett., vol. B632, pages 313–318, 2006.

[Foster 99] M. Foster & Christopher Michael. *Quark mass dependence of hadron masses from lattice QCD.* Phys.Rev., vol. D59, page 074503, 1999.

[Freund 92] Roland Freund, Gene H. Golub & Noel M. Nachtigal. *Iterative Solution of Linear Systems.* Acta Numerica, vol. 1, pages 57–100, 1992.

[Gamiz 12] E. Gamiz, Jon A. Bailey, A. Bazavov, C. Bernard, C. Bouchard*et al.* *Kaon semileptonic decay form factors with HISQ valence quarks.* PoS, vol. LATTICE2012, page 113, 2012.

[Gamiz 13] Elvira Gamiz. *Kaon semileptonic form factors with $N_f = 2+1+1$ HISQ fermions and physical light quark masses*, August 2013. `http://www.lattice2013.uni-mainz.de/presentations/7C/Gamiz.pdf`.

[Gasser 85] J. Gasser & H. Leutwyler. *Low-Energy Expansion of Meson Form-Factors.* Nucl.Phys., vol. B250, pages 517–538, 1985.

[Ghorbani 11] Karim Ghorbani. *Chiral and Volume Extrapolation of Pion and Kaon Electromagnetic form Factor within SU(3) ChPT.* 2011.

[Ghorbani 13] Karim Ghorbani & Hossein Ghorbani. *Kaon semi-leptonic form factor at zero momentum transfer in finite volume.* 2013.

[Gilge 13] Megan Gilge. Ibm system blue gene solution blue gene/q application development. IBM, 1 edition, 2013.

[Hardy 09] J.C. Hardy & I.S. Towner. *Superallowed nuclear beta decays: A New survey with precision tests of the conserved vector current hypothesis and the standard model.* Phys.Rev., vol. C79, page 055502, 2009.

[Haring 12] R.A. Haring, M. Ohmacht, T.W. Fox, M.K. Gschwind, D.L. Satterfield, K. Sugavanam, P.W. Coteus, P. Heidelberger, M.A. Blumrich, R.W. Wisniewski, A. Gara, G.L.-T. Chiu, P.A. Boyle, N.H. Chist & Changhoan Kim. *The IBM Blue Gene/Q Compute Chip.* Micro, IEEE, vol. 32, no. 2, pages 48–60, 2012.

[Hashimoto 99] Shoji Hashimoto, Aida X. El-Khadra, Andreas S. Kronfeld, Paul B. Mackenzie, Sinead M. Ryan*et al. Lattice QCD calculation of anti-$B \to D$ lepton anti-neutrino decay form-factors at zero recoil.* Phys.Rev., vol. D61, page 014502, 1999.

[Iwasaki 84] Y. Iwasaki & T. Yoshie. *RENORMALIZATION GROUP IMPROVED ACTION FOR SU(3) LATTICE GAUGE THEORY AND THE STRING TENSION.* Phys.Lett., vol. B143, page 449, 1984.

[Iwasaki 85] Y. Iwasaki. *Renormalization Group Analysis of Lattice Theories and Improved Lattice Action: Two-Dimensional Nonlinear O(N) Sigma Model.* Nucl.Phys., vol. B258, pages 141–156, 1985.

[Juettner 13] Andreas Juettner. *Kaon semileptonic decay from the SU(3)-symmetric point down to physical quark masses*, August 2013. `http://www.lattice2013.uni-mainz.de/presentations/7C/Juettner.pdf`.

[Kaneko 11] T. Kaneko*et al. Kaon semileptonic form factors in QCD with exact chiral symmetry.* PoS, vol. LATTICE2011, page 284, 2011.

[Kaplan 92] D. B. Kaplan. *A Method for Simulating Chiral Fermions on the Lattice.* PHYS.LETT.B, vol. 288, page 342, 1992.

[Kelly 11] Christopher Kelly. *Continuum Results for Light Hadronic Quantities using Domain Wall Fermions with the Iwasaki and DSDR Gauge Actions.* PoS, vol. LATTICE2011, page 285, 2011.

[Kobayashi 73] Makoto Kobayashi & Toshihide Maskawa. *CP Violation in the Renormalizable Theory of Weak Interaction.* Prog.Theor.Phys., vol. 49, pages 652–657, 1973.

[Leutwyler 84] H. Leutwyler & M. Roos. *Determination of the Elements V(us) and V(ud) of the Kobayashi-Maskawa Matrix.* Z.Phys., vol. C25, page 91, 1984.

[Lubicz 09] V. Lubicz, F. Mescia, S. Simula & C. Tarantino, for the ETM Collaboration. *$K \to \pi l \nu$ Semileptonic Form Factors from Two-Flavor Lattice QCD.* Phys.Rev., vol. D80, page 111502, 2009.

[Lubicz 10] V. Lubicz, F. Mescia, L. Orifici, S. Simula & C. Tarantino. *Improved analysis of the scalar and vector form factors of kaon semileptonic decays with $N_f = 2$ twisted-mass fermions.* PoS, vol. LATTICE2010, page 316, 2010.

[Luscher 04] Martin Luscher. *Solution of the Dirac equation in lattice QCD using a domain decomposition method.* Comput.Phys.Commun., vol. 156, pages 209–220, 2004.

[Luscher 05] Martin Luscher. *Schwarz-preconditioned HMC algorithm for two-flavour lattice QCD.* Comput.Phys.Commun., vol. 165, pages 199–220, 2005.

[Luscher 10] Martin Luscher. *Computational Strategies in Lattice QCD.* pages 331–399, 2010.

[Maltman 09] K. Maltman, C.E. Wolfe, S. Banerjee, I.M. Nugent & J.M. Roney. *Status of the Hadronic tau Decay Determination of —V(us)—.* Nucl.Phys.Proc.Suppl., vol. 189, pages 175–180, 2009.

[McNeile 06] C. McNeile & Christopher Michael. *Decay width of light quark hybrid meson from the lattice.* Phys.Rev., vol. D73, page 074506, 2006.

[Michael 98] Christopher Michael & J. Peisa. *Maximal variance reduction for stochastic propagators with applications to the static quark spectrum.* Phys.Rev., vol. D58, page 034506, 1998.

[Nachtigal 92a] Noël M. Nachtigal, Satish C. Reddy & Lloyd N. Trefethen. *How fast are nonsymmetric matrix iterations.* SIAM J. Matrix Anal. Appl., vol. 13, no. 3, pages 778–795, July 1992.

[Nachtigal 92b] Noël M. Nachtigal, Lothar Reichel & Lloyd N. Trefethen. *A Hybrid GMRES algorithm for nonsymmetric linear systems.* SIAM J. Matrix Anal. Appl., vol. 13, no. 3, pages 796–825, July 1992.

[O'Cais 04] Alan O'Cais, K. Jimmy Juge, Mike J. Peardon, Sinead M. Ryan & Jon-Ivar Skullerud. *Improving algorithms to compute all elements of the lattice quark propagator.* pages 844–849, 2004.

[Osborn 08] James C. Osborn. *Initial guesses for multi-shift solvers.* PoS, vol. LATTICE2008, page 029, 2008.

[R.Arthur 12] R.Arthur*et al. Domain Wall QCD with Near-Physical Pions.* 2012.

[Saad 86] Youcef Saad & Martin H Schultz. *GMRES: a generalized minimal residual algorithm for solving nonsymmetric linear systems.* SIAM J. Sci. Stat. Comput., vol. 7, no. 3, pages 856–869, July 1986.

[Saad 03] Y. Saad. Iterative methods for sparse linear systems. Society for Industrial and Applied Mathematics, 2003.

[Sachrajda 05] C.T. Sachrajda & G. Villadoro. *Twisted boundary conditions in lattice simulations.* Phys.Lett., vol. B609, pages 73–85, 2005.

[Sexton 92] J.C. Sexton & D.H. Weingarten. *Hamiltonian evolution for the hybrid Monte Carlo algorithm.* Nucl.Phys., vol. B380, pages 665–678, 1992.

[Shamir 93] Yigal Shamir. *Chiral Fermions from Lattice Boundaries.* Nuclear Physics B, vol. 406, page 90, 1993.

[Sheikholeslami 85] B. Sheikholeslami & R. Wohlert. *Improved Continuum Limit Lattice Action for QCD with Wilson Fermions.* Nucl.Phys., vol. B259, page 572, 1985.

[Sirlin 82] A. Sirlin. *Large m(W), m(Z) Behavior of the O(alpha) Corrections to Semileptonic Processes Mediated by W.* Nucl.Phys., vol. B196, page 83, 1982.

[Stathopoulos 13] Andreas Stathopoulos, Jesse Laeuchli & Kostas Orginos. *Hierarchical probing for estimating the trace of the matrix inverse on toroidal lattices.* 2013.

[Struckmann 01] T. Struckmann*et al. Flavor singlet pseudoscalar masses in N(f) = 2 QCD.* Phys.Rev., vol. D63, page 074503, 2001.

[Tang 11] Jok M. Tang & Yousef Saad. *A probing method for computing the diagonal of a matrix inverse.* Numerical Linear Algebra with Applications, vol. 19, no. 3, pages 485–501, 2011.

[Tsutsui 06] N. Tsutsui*et al. Kaon semileptonic decay form-factors in two-flavor QCD.* PoS, vol. LAT2005, page 357, 2006.